EXPLORING CORTICAL INFORMATION PROCESSING USING OPTOGENETICS

Thesis submitted by Stephen Alexander Rudinski

December 2014

A thesis submitted for the degree of Doctor of Philosophy of The Australian National University.

STATEMENT OF SOURCES

DECLARATION

I declare that this thesis is my own original work and has not been submitted in any other form for another degree or diploma at any university or other institution of tertiary education. Information derived from the published or unpublished work of others has been acknowledged in the text and a list of references is given. The research presented and reported in this thesis has been presented at a number of conferences. Abstracts published in conjunction with these presentations are listed below.

Rudinski, S.A. and Stuart, G.J. (2012) Functional characterisation of a channelrhodopsin-2 transgenic mouse. *Australasian Neuroscience Society Annual Meeting, Gold Coast*

Rudinski, S.A. and Stuart, G.J. (2012) Optogenetic tools in the study of cortical circuitry. *Eccles Institute of Neuroscience Seminar Series, Canberra*

Rudinski, S.A. and Stuart, G.J. (2012) Optogenetics: switching brain cells on and off with light. *University of the Third Age Annual Health Forum, Canberra*

Rudinski, S.A. and Stuart, G.J. (2011) Optogenetics: Probing the function of distal dendrites. *Australian Neuroscience Society Annual Meeting, Auckland*

S. A. Rudinski

December 2014

STATEMENT ON THE CONTRIBUTION OF OTHERS

I acknowledge the assistance and support of Professor Greg Stuart for project supervision and funding as well as research, analysis, and editorial assistance. I also acknowledge the contribution of Dr Vincent Daria for assistance with the development of optical equipment described in this thesis. Finally, I acknowledge the assistance of Professor George Augustine for provision of the animal model used in this project.

S. A. Rudinski

December 2014

STATEMENT OF ACCESS

I, the undersigned, author of this work, understand that the Australian National University will make this thesis available for use within the university library, research repository, and via the Australian Digital Thesis network, for use elsewhere. I understand that, as an unpublished work, a thesis has significant protection under the Copyright Act. Beyond this, I do not wish to place any restriction on access to this thesis.

S. A. Rudinski

December 2014

ELECTRONIC COPY

I, the undersigned, author of this work, declare that the electronic copy of this thesis provided to the Australian National University research repository is an accurate copy of the print thesis submitted, within the limits of the technology available.

S. A. Rudinski

December 2014

DECLARATION OF ETHICS

The research presented and reported in this thesis was conducted within the guidelines for research ethics outlined in the Australian National University Animal Experimentation Ethics Committee, and by extension, the Australian Code of Practice for the Care and Use of Animals for Scientific Purposes. The research methodology received clearance from the Australian National University and was performed under the Animal Ethics Protocol Numbers: JNS 42.08 and A2011/62.

S. A. Rudinski

December 2014

ACKNOWLEDGEMENTS

First and foremost I would like to express my indebtedness to my supervisor, Greg Stuart. Without his assiduous and indefatigable support not only would this project not have been possible but I would not have been afforded the many opportunities accompanying it. Above all else I would like to thank Greg for his invaluable advice, guidance, admonition, and commitment.

I would like to thank Vincent Daria for his valuable technical assistance and provision of optical apparatus which has complemented the results and aided the findings of this project. I would also like to thank George Augustine for provision of the animal model used in this project.

Many thanks also to all the technical staff that have facilitated the many facets of this project as well as my friends and fellow students.

Last but not least I would like to thank my family for their ongoing support and encouragement.

ABSTRACT

Optogenetics provides a powerful new tool for studying the way neurons integrate the inputs they receive, and how this shapes information processing in the brain. In this thesis we apply this new tool to investigate the mechanisms governing information processing in the somatosensory cortex of the mouse.

The first aspect of this study characterised the expression and activation of channelrhodopsin-2 (ChR2) in somatosensory barrel cortex of a widely used transgenic mouse line where ChR2 expression is driven by the Thy-1 promoter. Within somatosensory barrel cortex ChR2 expression was found in 96% of layer V and 72% of layer II/III pyramidal neurons. Expression of ChR2 was also found in the majority of fast-spiking interneurons in both layer II/III and V (78% and 86% respectively). This study shows that ChR2 expression is not limited to layer V pyramidal neurons in this mouse model as is commonly assumed.

The second aspect of this study developed a spatiotemporally precise method for optogenetic stimulation based on a projector-based optical interface. As proof-of-principle, three studies were conducted to assess the application of this method. Firstly, subcellular dendritic photo-stimulation was used to investigate the somatic impact of distal dendritic inputs in cortical pyramidal neurons. Secondly, this method was applied to mapping the spatial distribution of synaptic inputs to neurons in layer II/III and IV within somatosensory barrel cortex. We demonstrate that layer II/III pyramidal cells receive the majority of their excitatory synaptic input from layer IV and II/III, with fewer and weaker inputs arising from layer V within the same barrel. Interneurons in layer II/III also

received extensive excitatory synaptic input from layer IV in addition to surrounding layer II/III cells. The vertical profile of excitatory input to layer IV neurons indicated stronger input from layer IV and layer V than from layer II/III within the same barrel. Similar intra-columnar input profiles were also seen in interneurons residing in layer IV, where inputs were more numerous and stronger from layer IV than from layer II/III or layer V. Thirdly, using a thalamocortical slice we show that thalamocortical inputs arising from the thalamus have significantly higher connection probability and input strength in layer IV compared layer II/III and V.

The final aspect of this study investigated how inhibition targeted to somatic versus dendritic compartments shapes the firing output of layer V pyramidal neurons, and how the location of excitatory input influences this process. The findings presented illustrate that when excitatory drive is close to the soma both somatic and dendritic $GABA_A$-mediated inhibition has a purely subtractive effect on input-output relationships, whereas subtractive and divisive effects are observed during dendritic excitatory input. Somatic inhibition produces significantly more subtractive effects when excitation is driven somatically, whereas more divisive effects are observed during dendritic excitatory input. Together these findings suggest that both somatic and dendritic inhibition can generate divisive gain control provided excitatory drive is concentrated in dendritic compartments.

TABLE OF CONTENTS

LIST OF ABBREVIATIONS

ACSF	Artificial cerebrospinal fluid
AHP	After-hyperpolarisation
AP	Action potential
AP5	D-(-)-2-Amino-5-phosphonopentanoic acid
BSA	Bovine serum albumin
CGC	Cerebellar granule cell
ChR2	Channelrhodopsin-2
DNQX	6, 7-Dinitroquinoxaline-2, 3-dione
EPSP	Excitatory postsynaptic potential
GABA	γ-aminobutyric acid
NMDA	N-methyl-D-aspartate
PBS	Phosphate buffered saline
PV	Parvalbumin
SLM	Spatial light modulator
SOM	Somatostatin
TC	Thalamocortical
TTX	Tetrodotoxin
YFP	Yellow fluorescent protein

CHAPTER ONE

INTRODUCTION

1.1 Background

From an evolutionary perspective, the primary function of the brain is to increase our capacity to survive and reproduce. Evolution of the central nervous system (CNS) has produced a sophisticated organ capable of centralised control over other organ systems. This has been achieved by increasingly complex functional organisation and underlying neural networks, leading to a remarkable capacity to process and store information. One way in which neural function can be understood is as an information processing system. Drawing on a vast array of sensory input the brain creates representations of the outside world and through complex operations acts on this information to make us what we are. This is achieved by the concerted effort of billions of neurons connected to each other in complex networks.

Although the cell was recognised as the fundamental unit of living organisms during the early nineteenth century, it was not until the early twentieth century that single neurons were acknowledged as the basic building blocks of the nervous system. Until then the structure of the nervous system was explained by two opposing theories. The reticular theory – established by Joseph von Gerlach and championed by Camillo Golgi – described the nervous system as a continuous fused network. While the neuron theory (doctrine) – proposed by

Wilhelm His and later consolidated by Ramón y Cajal – argued that the nervous system is formed of structurally independent units (Bock, 2013). These early studies paved the way for our understanding of the structure and function of neurons and neuronal circuitry. Our appreciation of individual neurons as the fundamental signalling units of the nervous system has enabled us to understand the basis of neuronal information processing. Today we have a broad understanding of the physiology of individual neurons, the connections (or synapses) they form, and the organisational principles that produce the complex behaviour unique to the nervous system.

Individual neurons receive thousands of excitatory and inhibitory inputs distributed primarily onto their dendrites. The principle function of neurons is to integrate these synaptic inputs to produce an output in the form of an action potential. The manner in which neurons process these inputs is governed by both passive and active dendritic properties, which work together to shape synaptic integration and information processing (Yuste and Tank, 1996; Magee, 2000; Branco and Hausser, 2010). This ability to distil and modulate incoming information illustrates the remarkable computational capacity of single neurons and is fundamental to neuronal physiology and circuit function.

Our understanding of nervous system function has been largely predicated on the available tools capable of probing neuronal function. The development of new electrophysiological, pharmacological, and optical techniques has enabled sophisticated means to monitor and manipulate the activity of neurons, leading to substantial new information on how the brain works.

1.2 Optogenetics

Electrical stimulation and recording from neurons has been the go-to method in neuroscience research for over a century. The stimulation electrode – capable of generating local electric fields which trigger action potentials in nearby neurons – was developed in the late nineteenth century by Eduard Hitzig and Gustav Fritsch (Brazier, 1988). The temporal precision and reproducibility of responses evoked by electrical stimulation stands as the main strength of this method and is largely why electrode stimulation is still used as the primary way of controlling the electrical activity in neurons. Similarly, direct recording of electrical activity has long been the gold standard for monitoring neuronal function. The path-clamp technique, first developed in the mid-1970s and then refined in the early 1980s, enables measurement of electrical activity triggered by ion fluxes across neuronal membranes (Hamill *et al.*, 1981). Together these electrophysiological tools have contributed immensely to our understanding of neuronal function.

There are, however, limitations associated with these electrophysiological methods. Extracellular stimulating electrodes are incapable of reliably targeting specific neurons populations, presenting a fundamental challenge to determining the function of distinct neuronal subtypes. For example, the indiscriminate nature of electrical stimulation can result in the inadvertent activation of non-target excitatory or inhibitory cells within the area under investigation. Obstacles also arise from electrophysiological recording methods. The invasive nature of patch-clamp recording requires direct contact with the

tissue under investigation. These constraints put limitations on their usefulness for investigating neuronal function.

Recent developments in optical technologies have revolutionised neuroscience research. Advancements in fluorescence microscopy (Ji *et al.*, 2008) together with optical recording techniques such as voltage-sensitive dye imaging (Grinvald and Hildesheim, 2004; Palmer and Stuart, 2009), calcium imaging (Wallace *et al.*, 2008), fluorescent proteins (Akemann *et al.*, 2009) and calcium sensors (Chen *et al.*, 2012) enable relatively non-invasive methods to measure neuronal activity. Similarly, optical manipulation methods such as glutamate uncaging (Losonczy and Magee, 2006) and, more recently, optogenetics (Nagel *et al.*, 2003; Boyden *et al.*, 2005) have proven tremendously valuable for controlling neuronal activity in a more selective manner than is possible using extracellular stimulation.

Critically, the advent of optogenetic methods has provided a powerful tool for studying neural circuits. This technology employs the introduction of light sensitive proteins such as channelrhodopsin-2 (ChR2; Figure 1.1) into specific neuronal populations. Optogenetic methods address many of the technical constraints associated with electrode-based techniques and other existing optical methods. The ability to non-invasively and selectively target neuronal subtypes with high temporal and spatial precision represents a tremendous advance in the methods available for manipulating neuronal function (Nagel *et al.*, 2003; Boyden *et al.*, 2005; Arenkiel *et al.*, 2007; Wang *et al.*, 2007).

Figure 1.1: Channelrhodopsin-2

Schematic of the channelrhodopsin-2 (ChR2) protein. Following exposure to blue light (~470 nm) the protein undergoes a conformational change allowing sodium ions (Na^+) and very low levels of calcium ions (not shown) to enter the cell and potassium ions (K^+) to leave, leading to depolarisation.

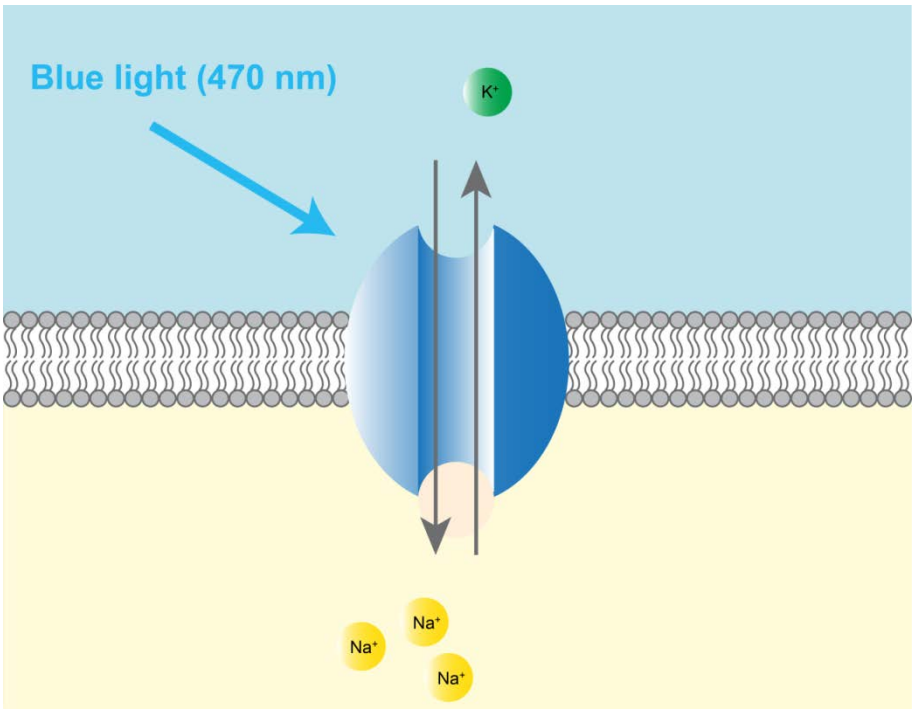
Blue light (470 nm)
K+
Na+
Na+
Na+

Multiple transgenic mouse lines have been developed expressing light-activated channels such as ChR2. The first transgenic mice expressing ChR2 drove expression using the Thy-1 gene. This gene is a member of the immunoglobulin super-family of genes and is expressed at high levels in the adult brain of rodents (Gordon *et al.*, 1987; Vidal *et al.*, 1990). This expression profile of the Thy-1 gene makes it an excellent system to drive neuron-specific expression of exogenous proteins. Moreover, fusing Thy-1-driven ChR2 with fluorescent proteins - such as yellow fluorescent protein (YFP) - permits the expression of both activator (ChR2) and reporter (YFP) genes enabling a useful means to map functional neuronal circuitry (Wang *et al.*, 2007). Of the many Thy-1-ChR2 founder lines developed, four (9, 15, 18, and 19) have been identified as having high levels of ChR2 expression in multiple brain regions (Arenkiel *et al.*, 2007; Wang *et al.*, 2007). Out of these founder lines, line 18 has been shown to exhibit high levels of ChR2-YFP in the cortex, including layer V pyramidal neurons (Arenkiel *et al.*, 2007; Wang *et al.*, 2007).

These animal models have proven immensely valuable in both *in vitro* and *in vivo* studies (Arenkiel *et al.*, 2007; Wang *et al.*, 2007), however, a detailed characterisation of these models is vital to determining their limitations and usefulness. To address this issue Chapter Three of this thesis describes the characterisation of ChR2 expression in somatosensory cortical neurons in the line 18 Thy-1-ChR2-YFP mouse. Analysis of the functional properties of ChR2 expression in this mouse line illustrates the benefits and constraints of the applicability of this model for investigating cortical circuitry.

The widespread application of optogenetic technologies has led to an evolving toolbox of photo-sensitive proteins (Zhang *et al.*, 2011; Asrican *et al.*, 2013). Despite these advances, optical techniques available for optogenetic activation remain relatively limited. Typically, excitation of light-sensitive optogenetic proteins is achieved by illumination with fluorescent lamps, light-emitting diodes (LEDs; often coupled with fibre optics), or scanning lasers coupled to confocal or two-photon microscopes (Aravanis *et al.*, 2007; Wang *et al.*, 2007). These techniques typically rely on wide-field or targeted illumination with little flexibility for dynamically probing multiple neurons across different regions simultaneously. To exploit the full potential of optogenetic methods for circuit mapping, an optical tool with high spatiotemporal and chromatic precision allowing the ability to simultaneously stimulate multiple areas in real-time is required. Chapter Four of this thesis describes the design and application of an optical interface capable of spatiotemporally precise photo-stimulation for optogenetics.

1.3 Mapping functional network connectivity in the cortex

The neocortex displays pronounced laminar and columnar organisation, which is highly conserved across different cortical areas. The laminar arrangement is characterised by morphologically distinct populations of neurons with characteristic inputs and outputs (Gilbert and Wiesel, 1983; Douglas and Martin, 2004), while vertical organisation consists of modular columns comprising characteristic projection patterns (Mountcastle, 1997; Panzeri *et al.*, 2003). This organisation gives rise to information flow largely within a columnar structure. Afferent signals arising from thalamic nuclei project primarily to cortical layer IV

neurons, which in turn relay this input to the supra-granular layers II and III and subsequently to infra-granular layers V and VI. The infra-granular layers form the primary output pathways projecting to subcortical regions (Douglas and Martin, 2004). While this canonical model of cortical organisation forms a widely accepted framework for studying cortical function it is nevertheless over simplified.

The layer IV to layer II/III pathway in the rodent somatosensory barrel cortex has been the subject of extensive investigation owing to its role in the earliest stages of intra-cortical processing (Shepherd *et al.*, 2003). Mapping functional synaptic connections within the barrel cortex has allowed the spatial organisation of inputs on layer II/III and IV neurons of the barrel cortex to be mapped. Thalamocortical signalling pathways have also been investigated extensively both *in vitro* and *in vivo*. The use of voltage-sensitive dye imaging (Grinvald and Hildesheim, 2004) and anatomical tracers (Aronoff *et al.*, 2010) *in vivo*, as well as multiple simultaneous patch-clamp recordings (Lefort *et al.*, 2009) and laser-scanning photo-stimulation of caged glutamate (Shepherd *et al.*, 2003) *in vitro*, has garnered a wealth of information about these pathways. Recently, optogenetic methods have been utilized to investigate synaptic connectivity in somatosensory barrel cortex (Wang *et al.*, 2007; Avermann *et al.*, 2012). These studies have proven valuable in obtaining a deeper understanding of neocortical microcircuitry.

Chapter Four of this thesis details the application of methods for spatiotemporally precise optogenetic photo-stimulation for examining functional microcircuits in the mouse somatosensory barrel cortex by activating distinct

fields of ChR2-expressing neurons in different cortical layers in an effort to map synaptic connectivity. In addition, this method of optogenetic photo-stimulation can be used to investigate long-range thalamocortical projections to pyramidal neurons in somatosensory barrel cortex.

1.4 Role of inhibition in shaping neuronal output

Pyramidal neurons comprise the principle excitatory neurons in the cortex. These cells are evolutionary conserved across species, particularly in brain structures associated with advanced cognitive functions (Spruston, 2008). Pyramidal neurons receive synaptic input across their dendrites, soma, and axon with the majority of synaptic input distributed across their dendrites. Critical to understanding how neurons integrate synaptic information is an appreciation of how synaptic events generated at different locations shape action potential output. This has been studied in depth in the context of excitatory synaptic input (Williams and Stuart, 2003; Larkum *et al.*, 2009; Murayama *et al.*, 2009), but much less is known about the impact of the location of inhibition on neuronal output.

How excitatory and inhibitory inputs are integrated within neurons determines their impact on neuron output. As the majority of this input is made onto the dendritic tree of neurons, the passive and active properties of dendrites will play a critical role in this process. An appreciation for the active involvement of dendrites in information processing in neurons can largely be attributed to the development of novel recording techniques allowing recording directly from these structures electrically (Stuart and Sakmann, 1994; Davie *et al.*, 2006)

together with powerful imaging methods (Ross and Werman, 1987; Lasser-Ross *et al.*, 1991; Kogan *et al.*, 1995). The last two decades have also seen rapid advances in optical imaging (Helmchen *et al.*, 1999), glutamate uncaging (Matsuzaki *et al.*, 2004), and *in vivo* patch-clamp recordings (Lee *et al.*, 2006). This has led to outstanding advances in our knowledge and understanding of the role of dendrites in synaptic integration. Despite this the interplay between excitatory glutamate-mediated input and inhibitory γ-aminobutyric acid (GABA)-mediated input remains poorly understood.

A wealth of theoretical and experimental studies demonstrates that individual neurons integrate their inputs in a multitude of non-linear ways greatly enhancing their computational power (Blomfield, 1974; Silver, 2010). Pyramidal neurons receive vast numbers of excitatory and inhibitory inputs and their ability to modulate output in terms of this synaptic input is vitally important for information processing. Interestingly, the distribution of excitatory and inhibitory inputs is not uniform across dendritic and somatic domains. In cortical pyramidal neurons, excitatory synaptic inputs are concentrated primarily on dendrites, whereas inhibitory inputs are distributed throughout the dendrites, soma, and axon initial segment (Megias *et al.*, 2001; Spruston, 2008). The functional implications of these different input distributions have been the subject of much research (Atallah *et al.*, 2012; Lee *et al.*, 2012; Wilson *et al.*, 2012; Pouille *et al.*, 2013).

The modulation of neuronal output is typically described in terms of the impact this has on the slope or offset (or both) of the input-output relationship between driving input and output firing rate. This relationship enables a distinction to be

made between modulatory inputs which generate additive (or subtractive) changes from those which produce multiplicative (or divisive) changes – indicative of gain control (Silver, 2010). In the case of inhibitory input, GABA-mediated inhibition acts by increasing membrane potential hyperpolarisation and/or increasing membrane conductance. Membrane hyperpolarisation produces a subtractive effect on excitatory input – observed as a uniform right-shift in the input-output curve. This acts to sharpen neuronal responses by filtering inputs based on relative strength. In contrast, increased membrane conductance (shunting inhibition) creates a divisive effect – observed as a change in the slope of the input-output relationship. This serves to scale excitatory synaptic input (Blomfield, 1974; Prescott and De Koninck, 2003; Ulrich, 2003; Silver, 2010). Although gain control is thought to play a critical role in brain function the underlying mechanisms remain poorly understood. Moreover, this field remains remarkably inchoate, influenced by the use of contrasting research paradigms. One of the major challenges presented by current research is the contrasting findings between theoretical modelling studies (Holt and Koch, 1997; Prescott and De Koninck, 2003) and experimental electrophysiological data (Chance *et al.*, 2002; Mitchell and Silver, 2003; Rothman *et al.*, 2009) particularly in relation to the influence of background synaptic noise and membrane conductance location, as well as opposing effects of sub-threshold events and firing output. This is also highlighted by recent studies exploring the impact of inhibition targeting dendritic and somatic domains of pyramidal neurons in visual cortex, *in vivo*, which reached opposing conclusions (Lee *et al.*, 2012; Wilson *et al.*, 2012).

Inhibitory interneurons in the cortex can be broadly classified into three groups based on the molecular markers they express, these include the calcium-binding protein parvalbumin, the neuropeptide somatostatin, and the ionotropic serotonin receptor 5HT3a (including neurons expressing the neuropeptide VIP) (Rudy *et al.*, 2011). The two most abundant of these groups – the parvalbumin-expressing (PV) interneurons and somatostatin-expressing (SOM) interneurons – exhibit distinct synaptic connectivity patterns. PV interneurons characteristically target inhibition to the somatic region of pyramidal neurons, whereas SOM interneurons target inhibition to the dendrites of pyramidal neurons (Markram *et al.*, 2004; Freund and Katona, 2007; Silberberg and Markram, 2007). These distinct properties of PV and SOM interneurons suggest that they may underlie distinct computational functions within cortical circuits.

Chapter Five of this thesis uses a combination of optogenetics and local pharmacology to investigate how dendritic and somatic inhibition influences neuronal output in pyramidal neurons in somatosensory barrel cortex. Spatiotemporally precise optogenetic photo-stimulation is used to excite pyramidal neurons at different locations and also to drive synaptic network inhibition in an effort to determine how somatic and dendritic inhibition transforms the relationship between input and neuronal output.

CHAPTER TWO

GENERAL MATERIALS AND METHODS

2.1 Materials

The channelrhodopsin-2 transgenic mouse line (Thy1-ChR2-YFP) was donated by Professor George Augustine, Lee Kong Chian School of Medicine, Nanyang Technological University, Singapore. This founder line was developed using a transgenic construct containing channelrhodopsin-2 (ChR2) and the yellow fluorescent protein (YFP) fusion gene under the control of the mouse thymus cell antigen 1 (Thy1) promoter (Figure 2.1). This construct was injected into C57BL/6 x SJL-F1 hybrid donor eggs and subsequently backcrossed to C57BL/6 mice. Mice were bred as homozygous crosses and litters genotyped for ChR2 expression.

All chemical reagents were purchased from Sigma-Aldrich, USA or Tocris Biosciences, UK. Drugs including 6, 7-Dinitroquinoxaline-2, 3-dione (DNQX), D-(-)-2-Amino-5-phosphonopentanoic acid (AP5), gabazine, and tetrodotoxin were purchased from Tocris Biosciences, UK. All drugs were prepared in aliquots at stock concentrations (generally 100x working solutions) and stored at -18ºC before being unfrozen and diluted before use.

Artificial cerebrospinal fluid (ACSF) was prepared daily with a composition of 125 mM NaCl, 3 mM KCl, 1.25 mM NaH_2PO_4, 25 mM $NaHCO_3$, 25 mM glucose, 2 mM $CaCl_2$, and 1 mM $MgCl_2$. Intracellular solution had a composition of 135

Figure 2.1: Transgenic expression of ChR2-YFP in mouse brain

ChR2-YFP expression is controlled by the regulatory elements of the mouse Thy1 gene. Left: Thy1-ChR2-YFP construct (reproduced from (Wang *et al.*, 2007b)). Right: YFP fluorescence in a coronal tissue slice.

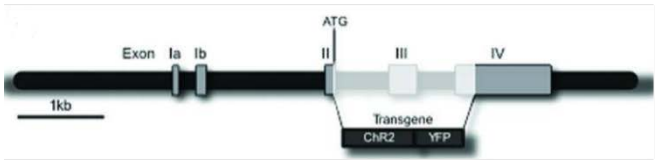
ATG
Exon
Ia
Ib
II
III
IV
1kb
Transgene
ChR2
YFP

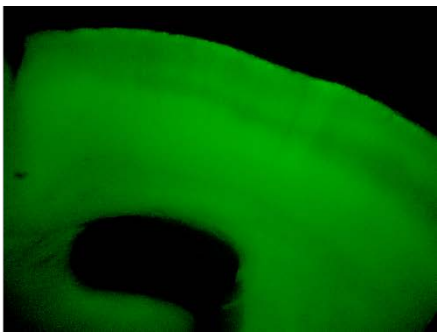

mM K-gluconate, 7 mM NaCl, 10 mM HEPES, 2 mM $MgCl_2$, and 2 mM Na_2ATP titrated with KOH to a pH of 7.2. On some occasions this solution also contained biocytin (for details see section 2.5, below). Intracellular solution was prepared in advance and stored at -18ºC before use. Reagents for biocytin staining were purchased from Vector Laboratories, USA.

2.2 Tissue Preparation

Experiments were performed on brain tissue slices from ChR2 mice aged 4-8 weeks. Both female and male mice were used without distinction. All animals were anaesthetised by isoflourane (3% in oxygen) and decapitated in accordance with procedures approved by the Australian National University Animal Experimentation Ethics Committee, and by extension the Australian Code of Practice for the Care and Use of Animals for Scientific Purposes.

A craniotomy was performed to expose the entire dorsal surface of the brain allowing removal of both hemispheres. Surgery was performed with tissue submerged in ice-cold (<4ºC) ACSF with 6 mM $MgCl_2$ at a pH of 7.4 perfused with 95% O_2/5% CO_2. The higher magnesium concentration was used to block NMDA receptor mediated Ca^{2+} influx and subsequent excitotoxicity (Rothman and Olney, 1986). Saturating the solution with 95% O_2/5% CO_2 provides necessary oxygenation and pH buffering. Once removed, brain tissue was mounted and fixed onto a stainless steel block with cyanoacrylate adhesive. Depending on the specific experiment tissue was fixed at an orientation and angle permitting preparation of coronal, sagittal, or thalamocortical slices. During slicing, brain tissue was submerged in ice-cold ACSF with 6 mM $MgCl_2$

perfused with 95% O_2/5% CO_2 and slices were sectioned at 300 µm (unless otherwise stated) using a tissue slicer (Campden Instruments; MA752, UK or Leica Microsystems; VT1000S, Germany). Where possible, tissue slices were sectioned in a plane conducive for preserving the dendritic structure of the cells within.

Once sectioned, tissue slices were transferred to a holding chamber containing ACSF perfused with 95% O_2/5% CO_2 and maintained at 35ºC using a water bath (Thermoline Scientific; UNI 110, Australia) for 30 minutes before being stored at room temperature (~22ºC) until required.

2.3 Electrophysiology

2.3.1 Recording

Tissue slices were individually transferred to the recording chamber and temporarily fixed in place using a nylon-strung harp mesh. The recording chamber was continuously perfused with 95% O_2/5% CO_2 saturated ACSF using a gravitation drip-feed system or a peristaltic pump (WPI; L22070, USA) and maintained at 35ºC via an automatic temperature controller and inline heater (Warner Instrument Corporation; TC-324B and SH-27B, United States). The recording chamber was positioned under an upright microscope (Zeiss; Axioskop, Germany) mounted on a vibration-isolation workstation (Kinetic Systems; 1201-01-12, USA).

Tissue slices and cells were visualised using infrared differential interference contrast (IR-DIC) optics enabling high image contrast and reduced light scatter, and an infrared-sensitive camera (Hamamatsu Photonics; C2400-07ER, Japan and PixeLINK; PLB957U, Canada). Cameras were coupled to LCD monitors for viewing. Patch-pipettes were prepared from filamented borosilicate glass (Harvard Apparatus, UK) and manufactured using a computer-controlled electrode puller (Sutter Instrument Co.; P-87, USA). Pipettes were pulled to produce tip diameters of approximately 1 µm with open-tip resistances of 5-7 MΩ. Prior to recording, pipettes were filled with filtered intracellular solution. Pipettes were then fixed to a pre-amplifier head stage mounted on a motorised micromanipulator (Luigs & Neuman; D-40880, Germany). Intracellular solution in the pipette was electrically coupled to the head stage via a chloride-coated silver wire and the head stage grounded to the recording chamber. The head stage was coupled to a bridge and voltage clamp amplifier (Dagan; BVC-700A, USA), which was connected to a computer (Apple Macintosh; Power Mac G4, USA) via a computer interface (Instrutech Corporation; ITC-16, USA).

Prior to recording and before immersing the recording pipette into the recording chamber, positive pressure was applied to the recording pipette and monitored using a digital manometer (TPI; 608, USA). This was performed to prevent debris from contaminating the pipette tip. Once immersed in the recording chamber the open-tip resistance of the pipette was determined under voltage clamp by applying a square voltage command and monitoring the current output. The recording electrode was then positioned directly under the microscope objective and lowered gradually to the tissue surface. At this point

any current offset between the recording electrode and the bath was corrected for in voltage-clamp mode.

The tip of the recording electrode was advanced to the cell body of the target neuron to a point where a slight deformation in the membrane was observed. The positive pressure was then released and subsequent negative pressure applied; this was timed with adjustment of the holding potential to -60mV. Negative pressure was released once the injected current required to maintain the applied holding potential fell below 20 pA; this was indicative of a seal resistance exceeding 3 GΩ between the electrode tip and cell membrane. Brief negative suction pulses were applied to rupture the membrane patch under the pipette tip and achieve the whole-cell recording configuration. At this point the amplifier was switched to current-clamp mode and the bridge balance and capacitance compensation adjusted. These measures were performed to correct for the voltage change across the series resistance of the pipette during current injection, and compensate for filtering by the pipette capacitance. Once this was achieved software protocols were executed according to individual experiments – as outlined in the methods sections accompanying each Results chapter.

2.3.2 Stimulation

Intracellular stimulation was achieved by injecting current into the recorded neuron through the recording pipette. All recorded cells were initially injected with sequential current steps across a negative to positive range to determine the cells' electrophysiological properties.

Extracellular stimulation was performed using patch-pipettes with open-tip resistances of 5-7 MΩ filled with ACSF at a pH of 7.4. Pipettes were mounted on a motorised micromanipulator (Luigs & Neuman; D40880, Germany) with the solution inside the pipette electrically coupled to a bipolar stimulus isolator (World Precision Instruments; A360, USA) via a chloride-coated silver wire. In some cases the other pole of the stimulus isolator was in turn grounded to the bath. The bipolar stimulus isolator was connected to the computer (Apple Macintosh; Power Mac G4, USA) via a computer interface (Instrutech Corporation; ITC-16, USA).

The stimulating electrode was positioned directly under the microscope objective and lowered gradually to the tissue surface. The tip of the stimulating electrode was then advanced to a given distance lateral to the soma of the recorded neuron. Extracellular stimulation protocols to evoke synaptic responses were executed according to the requirements of individual experiments – as detailed in the methods sections in the accompanying Results chapters.

2.4 Optogenetics

Optogenetic stimulation was achieved by photo-stimulating ChR2-expressing neurons with 470 nm (blue) light. Wide-field illumination was achieved using a high-intensity arc lamp (Cairn, USA) with a shutter system (Vincent Associates; Uniblitz VCM-D1, USA), or an Illumination unit and controller (Photonics; Polychrome II, USA), coupled to the microscope via a fibre optic cable. Following development of a projector-based illumination system – detailed in

Chapter Four – this system was used for subsequent experiments. Light was delivered to the tissue through the microscope objective, and total light power was recorded using a power meter (Thorlabs; PM100A, USA). Optogenetic methods are discussed in detail in the methods sections accompanying each Chapter.

2.5 Histology

Recorded neurons were morphologically reconstructed and analysed using a biocytin staining protocol and neuron tracing software. For loading cells with biocytin the intracellular solution contained 0.2% (3 mg/ml) biocytin. Whole-cell recordings were maintained for at least 10-15 minutes to allow adequate filling of the neuron. At the conclusion of the experiment, individual tissue slices were fixed in 4% paraformaldehyde for 1 hour before being washed 3 times with phosphate buffered saline (PBS) and then stored in PBS at 4ºC. For staining, tissue slices were initially added to a PBS solution containing 1% H_2O_2 for 15 minutes to block endogenous peroxidases. Tissue slices were then added to a PBS solution containing 1% bovine serum albumin (BSA) and 0.3% triton X-100 for 1 hour at room temperature to permeabilise the cell membrane and block non-specific binding. This solution was then removed and tissue slices incubated in a solution containing the avidin-biotin peroxidase reaction solution (Vector laboratories; Vectastain Elite ABC kit, USA) for 24 hours at 4ºC.

Tissue slices were then washed 3 times with PBS and incubated in DAB for 5-10 minutes for stain visualisation. Individual tissue slices were then mounted on glass slides with movial (polyvinyl alcohol) mounting solution. Mounted tissue

slices were stored at 4ºC and cells visualised under a microscope (Zeiss; Axioskop II, USA) and reconstructed using neuron tracing software (MBF Bioscience; Neurolucida, USA).

2.6 Data Acquisition and Analysis

Voltage and current signals were filtered at 10 kHz and digitised at a sample rate of 50 kHz by a computer interface (Instrutech Corporation; ITC-16, USA) under the control of acquisition software (Axon Instruments; Axograph, USA) on a computer (Apple Macintosh; Power Mac G4, USA). Acquisition software was used for both data acquisition and primary analysis. Exported data were further analysed using statistical software (IBM Corporation; SPSS, USA; Microsoft; Excel, USA; and GraphPad Software; Prism, USA). Figures were generated using graphics editor software (Adobe; Illustrator, USA). Unless otherwise stated, data were presented as the mean ± standard error of the mean (SEM). Statistical analysis between two independent datasets was performed using the unpaired, two-tailed Student's t-test for data comparisons. Where more than two datasets were analysed a one-way ANOVA was used. Values of $p<0.05$ were accepted as statistically significant.

CHAPTER THREE

CHANNELRHODOPSIN-2 MODEL CHARACTERISATION

3.1 Introduction

Optogenetic methods provide a powerful tool for studying cortical circuitry. As a result, multiple transgenic mouse lines have been developed expressing light-activated channels such as channelrhodopsin-2 (ChR2). A detailed characterisation of these models is vital for determining their limitations and usefulness.

The first transgenic mice expressing ChR2 were generated with expression driven by the Thy-1 promoter. This gene is a member of the immunoglobulin super-family of genes and is expressed at high levels in the adult brain of rodents (Gordon *et al.*, 1987; Vidal *et al.*, 1990). This expression profile makes it an excellent system for driving neuron-specific expression of exogenous proteins such as ChR2. Moreover, fusion of ChR2 with a fluorescent reporter - such as yellow fluorescent protein (YFP) – permitted the expression of both activator (ChR2) and reporter (YFP) in the same cells providing a useful model to map functional neuronal circuitry (Wang *et al.*, 2007).

Transgenic mice expressing ChR2 under the control of the Thy-1 promoter exhibit broad transgene expression throughout the nervous system. This expression, however, is random in subsets of neurons in different mouse lines (Feng *et al.*, 2000) presenting the exigency for founder lines with regionally

restricted ChR2 expression. Of the many founder lines first developed, four (9, 15, 18, and 19) were identified as having high levels of ChR2 expression in multiple brain regions (Arenkiel *et al.*, 2007). ChR2-YFP expression was detected in hippocampal CA1/CA3 pyramidal neurons, thalamic nuclei, midbrain, and brainstem in all four of these lines while expression was also seen in cerebellar mossy fibres (lines 18 and 19) and cortical pyramidal neurons (lines 9, 15, and 18) (Arenkiel *et al.*, 2007; Wang *et al.*, 2007).

Transgenic expression systems exhibit considerable variability in their patterns of expression among lines generated from the same construct. These variations are greatest from line to line, however, are also present among descendants of a single founder. Line-to-line variation can be accounted for by differences in chromosomal insertion sites and transgene copy number, as well as the influence of unlinked genes. Variation in transgene-directed expression – that is, within animals from a single founder – is poorly understood. It is postulated that combinatorial specificity, chromatin conformation, and position-effect variegation may contribute to this (Feng *et al.*, 2000). The high prevalence of variation in patterns of Thy-1-driven ChR2-YFP makes it essential to characterise the distribution of expression within individual lines.

Out of the primary Thy-1 founder lines generated, line 18, has been shown to exhibit high levels of ChR2-YFP in the cortex, including layer V pyramidal neurons (Arenkiel *et al.*, 2007; Wang *et al.*, 2007). To determine the precise profile of ChR2 expression in the somatosensory cortex of this animal model, whole-cell recordings were made from pyramidal neurons and inhibitory interneurons in layers II/III and V of primary somatosensory barrel cortex.

This chapter describes the characterisation of ChR2 expression in cortical neurons in the line 18 Thy-1-ChR2-YFP mouse. Analysis of the functional properties of this expression places constraints on the applicability of this model for investigating cortical circuitry.

3.2 Methods

3.2.1 Neuron Classification

Brain tissue slices from ChR2-YFP mice were sectioned in either coronal or sagittal planes – as described in Methods section 2.2. Primary somatosensory cortex (S1) was identified from brain atlas coordinates and appearance of anatomical markers present at given tissue-section depths (Franklin and Paxinos, 2008). Neurons were selected based on the laminar location of their somata and, where possible, were selected uniformly within cortical layers. Where comparisons between ChR2-YFP and wild-type mice were performed, wild-type littermates from the same line were used.

Whole-cell patch-clamp recordings were made from the somata of putative pyramidal neurons and interneurons in layers II/III and V of the somatosensory cortex. Intracellular solution containing biocytin was used to allow for morphological reconstruction of recorded cells – as described in Methods section 2.5. In current-clamp a series of current steps of 400 ms duration with amplitudes increasing from -200 pA to 400 pA in 50 pA increments were applied. Input resistance was calculated from the linear fit to V/I curves generated from voltage responses to hyperpolarising current steps. Single action potential (AP) properties were measured for the first AP occurring 10 ms after current pulse onset for the first current step exceeding rheobase (Figure 3.1). AP threshold was defined as the membrane potential (V_m) at which dV_m/dt first exceeded 50 V/s. AP height was defined as the amplitude from AP threshold to AP peak. AP half-width was measured as the AP width at the

Figure 3.1: Active electrophysiological parameters measured from supra-threshold responses

Description of the different active electrical properties measured during action potentials: action potential (AP) threshold, height, half-width, and after-hyperpolarisation (AHP) amplitude.

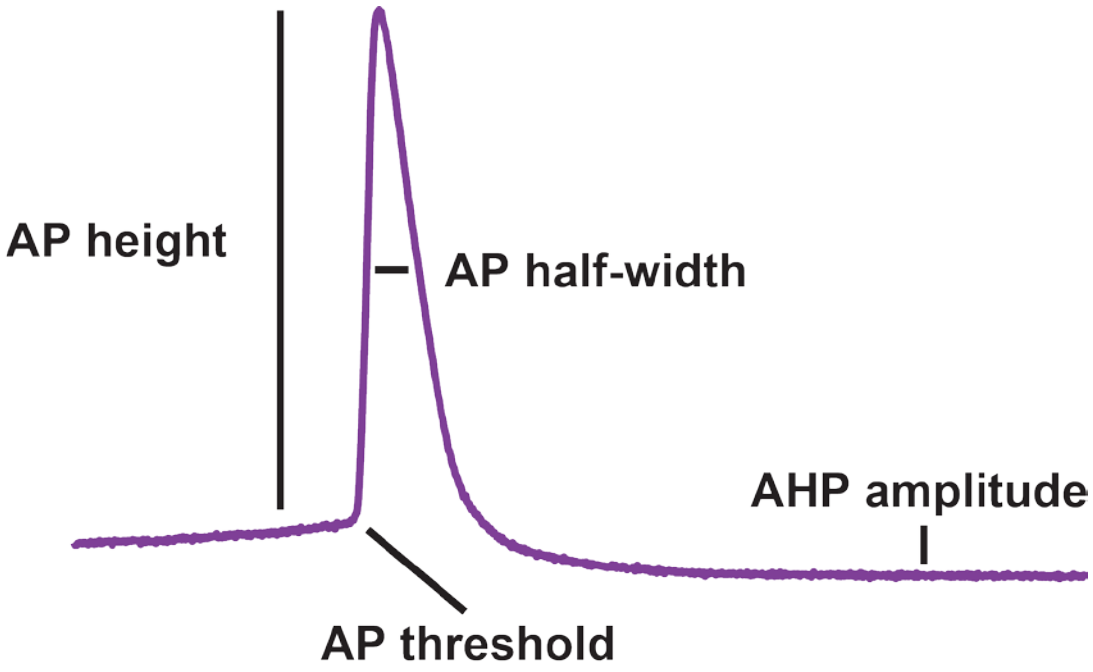
AP height
AP half-width
AHP amplitude
AP threshold

halfway point between AP threshold and AP peak. After-hyperpolarisation (AHP) amplitude was measured as the peak of the AHP relative to the AP threshold. For recordings in voltage-clamp, neurons were held close to the resting potential (V_{rest}) of putatively identified pyramidal cells (-64 mV) and interneurons (-70 mV).

3.2.2 Photo-stimulation

For photo-stimulation of ChR2-expressing cells wide-field illumination was used as described in Methods section 2.4 to generate 470 nm light with a total light power of 6.5 mW. Light was delivered to the tissue through the microscope objective yielding a circular light field. The diameter of the illumination area was manually adjusted using the epifluorescent field diaphragm of the microscope. This enabled circular illumination with diameters ranging from 20 µm to 365 µm (full-field with 60x objective). The size of the area illuminated was measured using a micro-ruler at the tissue surface. Light intensity was measured as total light power and reported as light power density, calculated by dividing the total emitted light power by the area of the illuminated field. Full-field illumination through a 60x objective yielded a maximum light power density of 5.7 mW/mm^2. Light emission by the illumination unit and controller used in these experiments (as described in Methods section 2.4) occurred with a notable delay after triggering via the acquisition software. This delay was measured to be 7.9 ± 0.8 ms (n = 10). All figures have been corrected for this delay to represent the onset and offset of photo-stimulation rather than when the light source was triggered.

To investigate the effective light intensity at different tissue depths light transmission measurements were performed using tissue slices with a range of thicknesses between 200 µm and 1000 µm, sectioned at 200 µm increments as described in Methods section 2.2. As per the recording setup, individual tissue slices were transferred to the recording chamber and positioned under the microscope. The microscope objective was then advanced to a depth at which the tissue surface was in focus and 470 nm light was delivered to the tissue. The photo-detector of a power meter (ThorLabs; PM100A, USA) was positioned directly under the recording chamber and total light power recorded, reflecting transmission through the tissue slice. This was then repeated after removal of the tissue. Five trials for each slice thickness were performed and a transmission fraction was calculated as the power with tissue present divided by the power with no tissue present. Total transmitted light power was determined to be reduced by less than 10% at a typical somatic intracellular recording depth of 20 µm (Figure 3.2).

3.2.3 Synaptic Connectivity

Synaptic transmission was assessed using extracellular electrical stimulation to generate excitatory postsynaptic potentials (EPSPs) in post-synaptic cells. A bipolar stimulus isolator was used to deliver 100 µs duration constant current pulses of variable amplitude to an extracellular stimulation pipette as described in Methods section 2.3. Glutamate receptor antagonists DNQX and AP5, as well as the $GABA_A$ receptor antagonist gabazine, were used to block synaptic transmission. Synaptic antagonists were delivered in ACSF via gravity drip-feed at a flow rate of 2 ml/minute. For investigating synaptic photo-responses,

Figure 3.2: Transmission of blue (470 nm) light through mouse cortical tissue

Measured total transmission fraction of 470 nm light through cortical tissue as a function of tissue thickness (n = 5). Data fitted with an exponential function.

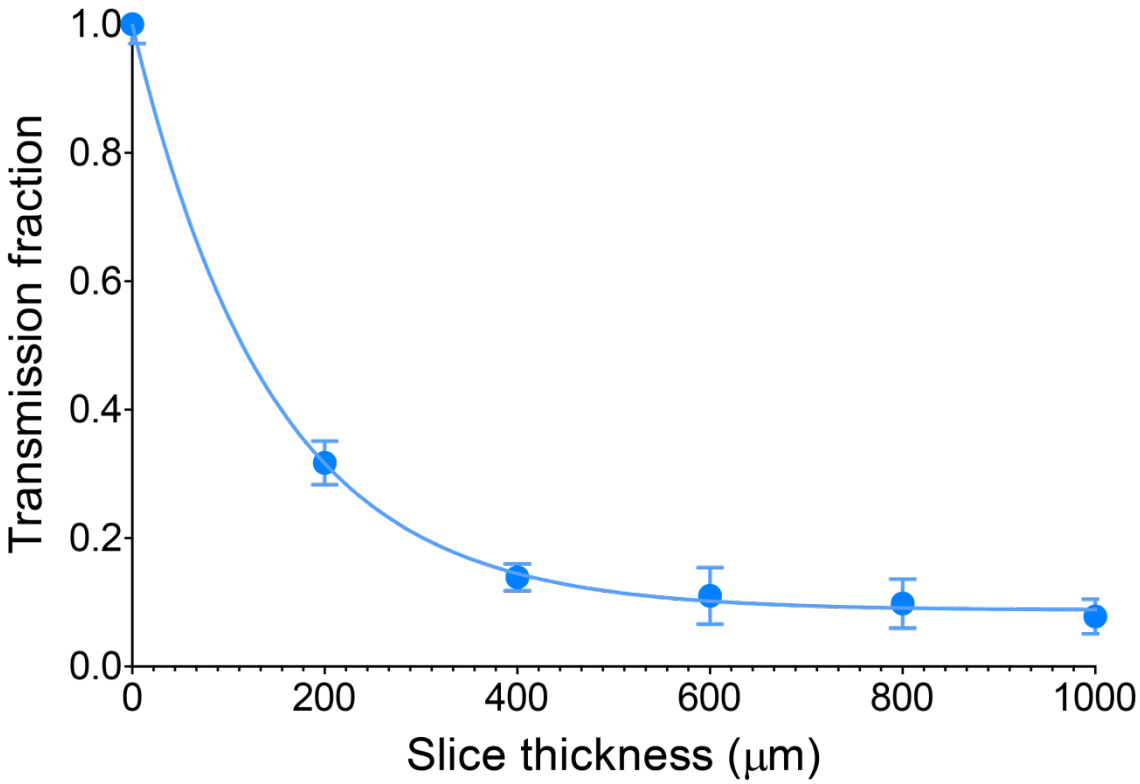
Transmission fraction
1.0
0.8
0.6
0.4
0.2
0.0
0
200
400
600
800
1000
Slice thickness (μm)

sequences of alternating electrical stimulation and full-field light pulses were delivered during the application and subsequent wash-out of synaptic blockers.

3.3 Results

3.3.1 Neuronal expression of ChR2-YFP in somatosensory cortex

To determine the functional expression of ChR2 in primary somatosensory cortex, whole-cell patch-clamp recordings were made from the somata of visualised neurons in layers II/III and V. Neurons were classified and identified based on the laminar location of their somata, their cellular morphology, and their intrinsic electrical properties.

Neurons were first classified by the layer in which their somata resided. This was determined based on the relative distance from the pia. To reveal the cellular morphology of neurons, cells were filled with biocytin and their dendritic tree was reconstructed using neuron tracing software (MBF Bioscience; Neurolucida, USA). Pyramidal neurons were characterised by their eponymous pyramidal-shaped soma and their distinct apical and basal dendritic structures (Figure 3.3A,B). Pyramidal cells in both layers II/III (n = 5) and V (n = 8) display a prominent apical dendrite emanating from the apex of the soma and extending radially towards the pia. In layer V neurons, this apical dendrite was considerably longer than that seen in layer II/III neurons, boasting fewer oblique apical dendrites and terminating in an apical tuft. Additionally, the basal dendrites of layer II/III pyramidal neurons were considerably more expansive and diffuse than that seen in layer V cells (Spruston, 2008).

Neighbouring interneurons in these cortical layers were strikingly different in morphology. Interneurons in both layer II/III (n = 5) and V (n = 6) lacked distinct

Figure 3.3: Morphological reconstructions of different neuron classes in somatosensory cortex

Top: Tracings illustrating the typical cellular morphology of a layer V (**A**; blue) and layer II/III (**B**; green) pyramidal neuron and interneurons in layer V (**C**; red) and layer II/III (**D**; orange). Bottom: Example whole-cell current-clamp recordings from layer V (blue) and layer II/III (green) pyramidal neurons, and layer V (red) and layer II/III (orange) interneurons.

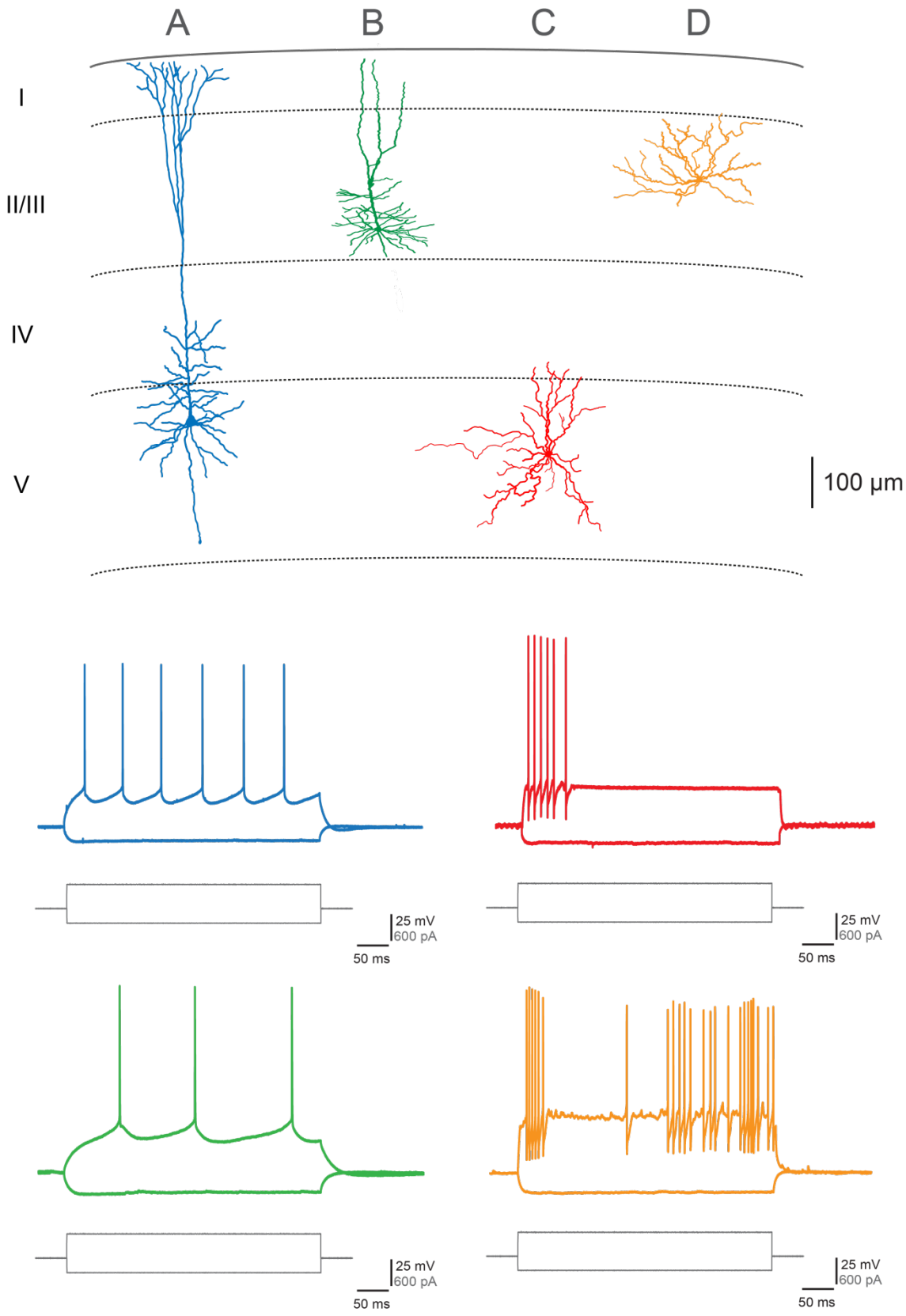
A
B
C
D
I
II/III
IV
V
100 µm
25 mV
600 pA
50 ms
25 mV
600 pA
50 ms
25 mV
600 pA
50 ms
25 mV
600 pA
50 ms

apical and basal dendritic domains, and possessed considerably more complex and ramifying dendrites (Figure 3.3C,D). Dendritic morphology also varied considerably between interneurons, consistent with the diversity of interneuron classes in different cortical layers (Markram *et al.*, 2004; DeFelipe *et al.*, 2013).

The intrinsic electrical properties of neurons were determined from voltage responses to somatic current injection (see Methods section 3.2.1). Example supra-threshold traces are shown in Figure 3.3 (bottom) and electrical properties are listed in Table 3.1. The most evident electrophysiological distinction between pyramidal cells and interneurons was in the shape of the AP waveform. The AP half-width was significantly smaller in layer V interneurons compared with pyramidal cells (Table 3.1; $P < 0.05$). Similarly, in layer II/III AP half-width was significantly less in interneurons compared to pyramidal cells (Table 3.1; $P < 0.05$). In addition to these differences in AP duration, a marked difference was seen in the amplitude of the AHP. AHPs were significantly larger in interneurons compared with pyramidal cells in both layer V (Table 3.1; $P < 0.05$) and layer II/III (Table 3.1; $P < 0.05$).

AP threshold was also significantly more hyperpolarised in interneurons compared to pyramidal neurons in layer V (Table 3.1; $P < 0.05$). In layer II/III this difference in AP threshold between interneurons and pyramidal cells was even more pronounced (Table 3.1; $P < 0.05$). AP height was also significantly higher in pyramidal neurons compared to interneurons in layer V (Table 3.1; $P < 0.05$) and in layer II/III (Table 3.1; $P < 0.05$).

Table 3.1: Electrical properties of different neuron classes in ChR2 mice

Resting membrane potential (RP), input resistance (R_{in}), action potential (AP) threshold, height, half-width, and after-hyperpolarisation (AHP) amplitude for layer II/III and V pyramidal neurons and interneurons. Interneurons within cortical layers show significant differences from pyramidal neurons in all parameters measured. This enabled broad differentiation of these cell types based on their electrophysiology. Values are mean ± SEM (n's in brackets, $p<0.05$).

Cell type	Pyramidal		Interneuron	
Cortical layer (n)	II/III (24)	V (24)	II/III (18)	V (21)
V_{rest} (mV)	-64 ± 0.4	-63 ± 0.4	-66.9 ± 0.5	-67.3 ± 0.4
R_{in} (MΩ)	142.9 ± 2.6	100.3 ± 1.5	94.9 ± 1.9	91.1 ± 2.7
AP threshold (mV)	-23.9 ± 0.6	-21.8 ± 0.7	-41.4 ± 1.1	-34.2 ± 1.3
AP height (mV)	95.7 ± 1.2	100.4 ± 0.8	69.8 ± 1.6	79.9 ± 2
AP half-width (ms)	0.77 ± 0.01	0.74 ± 0.01	0.42 ± 0.01	0.19 ± 0.01
AHP amplitude (mV)	12.3 ± 0.4	9.7 ± 0.3	19.1 ± 0.7	18.8 ± 0.6

Correlations between AP half-width and AHP amplitude demonstrated marked distinctions between pyramidal cells and interneurons. This was evident as clear clustering of pyramidal and interneuron populations in scatter plots of these parameters (Figure 3.4A). The exceptionally brief AP half-widths seen in layer V interneurons distinguished this population from interneurons in layer II/III. Similarly, scatter plots of AP height and AP threshold demonstrated clustering of pyramidal and interneurons populations (Figure 3.4A). These data revealed an apparent linear relationship between AP peak amplitude and AP threshold.

Interneurons in layer V were also found to have significantly more hyperpolarised resting membrane potentials (V_{rest}) than layer V pyramidal neurons (Table 3.1; $P < 0.05$). Likewise, in layer II/III interneurons demonstrated significantly more hyperpolarised V_{rest} than pyramidal cells (Table 3.1; $P < 0.05$). Input resistance was also significantly higher in pyramidal neurons compared to neighbouring interneurons in both layer 2/3 and layer V (Figure 3.4C-F and Table 3.1; $P < 0.05$).

To determine whether the introduction of ChR2 influenced the intrinsic functional properties of neurons whole-cell patch-clamp recordings were made from pyramidal neurons and interneurons in layers II/III and V of wild-type (WT) mice. In Thy-1-ChR2-YFP mice voltage responses were evaluated in response to photo-stimulation to verify ChR2 expression (See section 3.3.2 – below). Electrical properties of neurons were determined from voltage responses to somatic current injection in the absence of photo-stimulation. Comparing pyramidal neurons in ChR2 and WT mice revealed no significant difference in

Figure 3.4: Electrophysiological classification of cortical neuron types

A: Scatter plot of AP half-width against AHP amplitude for layer II/III and layer V pyramidal neurons and interneurons illustrating clear clustering between these different cell types. **B**: Scatter plot of AP threshold against AP height for layer II/III and layer V pyramidal neurons and interneurons. **C** and **D**: Example whole-cell current-clamp recordings from a layer V pyramidal neuron (blue) and interneuron (red). **E**: Voltage/current plot from the cells in **C** and **D**. **F**: Average input resistance of layer V pyramidal neurons (n = 24) and interneurons (n = 21). Data show mean ± SEM.

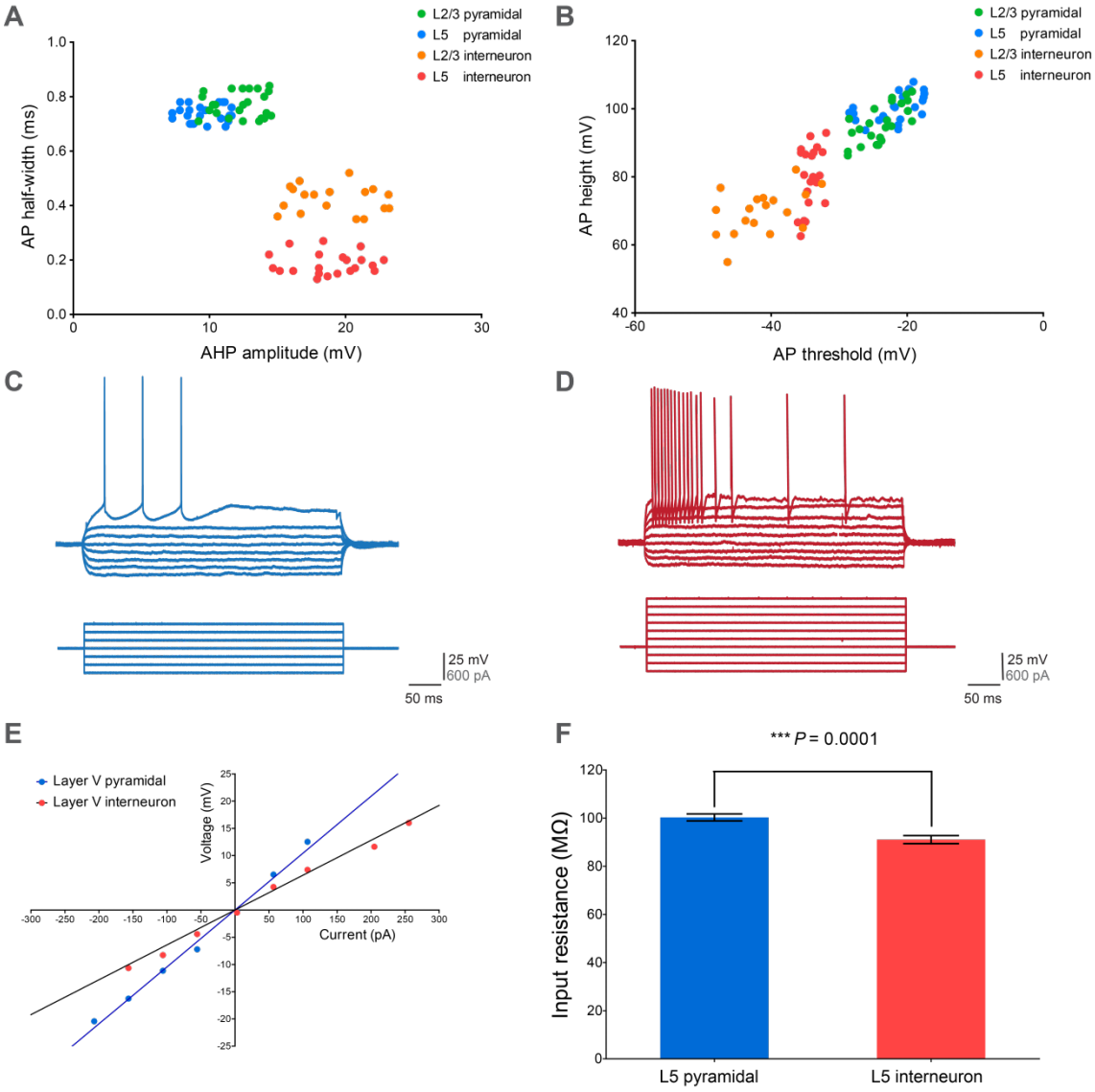
A
L2/3 pyramidal
L5 pyramidal
L2/3 interneuron
L5 interneuron
AP half-width (ms)
AHP amplitude (mV)
B
AP height (mV)
AP threshold (mV)
C
25 mV
600 pA
50 ms
D
E
Layer V pyramidal
Layer V interneuron
Voltage (mV)
Current (pA)
F
*** P = 0.0001
Input resistance (MΩ)
L5 pyramidal
L5 interneuron

resting membrane potential in either layer II/III or layer V (Table 3.2; $P \geq 0.05$). Similarly, input resistance was not significantly different in layer II/III pyramidal neurons in ChR2 mice compared with WT mice (Table 3.2; $P \geq 0.05$). Action potential threshold, height, half-width, and after-hyperpolarisation amplitude in both layers II/III and V also did not show any significant differences between ChR2 mice and WT mice (Table 3.2; $P \geq 0.05$).

To further investigate the potential impact of ChR2 expression on the functional properties of neurons in Thy-1-ChR2-YFP mice, recordings were made from ChR2-positive and ChR2-negative pyramidal neurons and interneurons in the same tissue slices. Based on the high level of ChR2 expression in layer V cells, this comparison was only possible in layer II/III (See section 3.3.2 – below). Voltage responses were recorded in response to photo-stimulation to distinguish ChR2-positive from ChR2-negative cells.

Consistent with the findings comparing ChR2 mice with WT mice, no significant differences in resting membrane potential were observed between ChR2-positive and ChR2-negative pyramidal cells or interneurons in layer II/III (Table 3.3; $P \geq 0.05$). Input resistance was also not statistically different between cells expressing ChR2 and non-expressing cells. Interestingly, while AP threshold demonstrated no significant difference between ChR2-positive and ChR2-negative pyramidal neurons, interneurons expressing ChR2 revealed a significantly more hyperpolarised AP threshold compared to ChR2-negative interneurons (Table 3.3; $P < 0.05$). AP height demonstrated no disparity between ChR2-positive and ChR2-negative pyramidal cells or interneurons. AP duration was unaffected by ChR2 expression in pyramidal neurons, however,

Table 3.2: Comparison of the electrical properties of different neuron classes in ChR2 and wild type mice

Resting membrane potential (RP), input resistance (R_{in}),action potential (AP) threshold, height, half-width, and after-hyperpolarisation (AHP) amplitude for layer II/III and V pyramidal cells and interneurons in ChR2 and wild type mice. All parameters measured between ChR2 and wild type mice were not statistically significant. Values are mean ± SEM (p<0.05).

Cell type	Pyramidal				Interneuron			
Cortical layer	II/III		V		II/III		V	
Model (n)	ChR2 (24)	WT (9)	ChR2 (24)	WT (10)	ChR2 (18)	WT (6)	ChR2 (21)	WT (6)
V_{rest} (mV)	-64.1 ± 0.4	-64.5 ± 0.6	-63 ± 0.4	-62.2 ± 0.8	-66.9 ± 0.5	-66 ± 0.8	-67.3 ± 0.4	-68.1 ± 0.8
R_{in} (MΩ)	142.9 ± 2.6	137.4 ± 3.8	100.3 ± 1.5	103.6 ± 2.4	94.8 ± 1.9	94.8 ± 3.9	91.1 ± 2.7	100.5 ± 3.3
AP threshold (mV)	-23.9 ± 0.6	-24.3 ± 1	-21.8 ± 0.7	-25.6 ± 1.2	-41.4 ± 1.1	-39.8 ± 2.3	-34.2 ± 1.3	-31.3 ± 0.7
AP height (mV)	95.7 ± 1.2	93.6 ± 1.3	100.4 ± 0.8	96.1 ± 1.7	69.8 ± 1.6	74.1 ± 2.1	79.9 ± 2	83.1 ± 3.6
AP half-width (ms)	0.77 ± 0.01	0.74 ± 0.01	0.74 ± 0.01	0.8 ± 0.02	0.42 ± 0.01	0.44 ± 0.02	0.19 ± 0.01	0.2 ± 0.02
AHP amplitude (mV)	12.3 ± 0.4	12 ± 0.6	9.7 ± 0.3	9.3 ± 0.5	19.1 ± 0.7	19 ± 1.2	18.8 ± 0.6	18.7 ± 0.8

Table 3.3: Comparison of the electrical properties of different neuronal classes in ChR2-positive and ChR2-negative layer II/III neurons

Resting membrane potential (RP), input resistance (R_{in}), action potential (AP) threshold, height, half-width, and after-hyperpolarisation (AHP) amplitude for ChR2-positive (ChR2+) and ChR2-negative (ChR2-) layer II/III pyramidal cells and interneurons. AP threshold and half-width for layer II/III interneurons (in bold) show significant differences between ChR2+ and ChR2- cells in the same slice. All other parameters between ChR2+ and ChR2- cells were not statistically significant. Values are mean ± SEM (p<0.05).

Cell type	Pyramidal		Interneuron	
Model (n)	ChR2+ (12)	ChR2- (12)	ChR2+ (8)	ChR2- (9)
V_{rest} (mV)	-64.1 ± 0.6	-63.4 ± 0.3	-67.3 ± 0.6	-66.6 ± 0.8
R_{in} (MΩ)	142.7 ± 3.6	133.7 ± 3	95.8 ± 2.9	96 ± 2.6
AP threshold (mV)	-24.3 ± 1	-22.6 ± 0.8	**-40.8 ± 2**	**-35.6 ± 0.3**
AP height (mV)	95.6 ± 1.8	94.4 ± 1.4	72.5 ± 2.3	73 ± 2.3
AP half-width (ms)	0.77 ± 0.02	0.81 ± 0.01	**0.37 ± 0.02**	**0.3 ± 0.02**
AHP amplitude (mV)	12.1 ± 0.5	12.8 ± 0.4	20.8 ± 0.9	21 ± 1.1

ChR2-positive interneurons had significantly broader Aps compared to ChR2-negative interneurons (Table 3.3; $P < 0.05$). The AP after-hyperpolarisation was not altered by ChR2 expression in either pyramidal cells or interneurons.

To assess the ability of ChR2 activation to elicit action potentials, voltage responses to photo-stimulation were recorded in current-clamp in layer V pyramidal cells. Brief light pulses generated sub-threshold depolarisations with amplitudes dependent on light intensity, with higher intensities producing short-latency action potentials (Figure 3.5A). These membrane potential depolarisations were precisely timed and were comparable to membrane depolarisations generated by somatic current injection (Figure 3.5B). Action potentials generated by brief light pulses showed remarkable temporal precision and were reliably reproduced over multiple trials (Figure 3.5C).

Prolonged photo-stimulation evoked trains of action potentials mimicking firing patterns seen during somatic current injection (Figure 3.5D, E), and lower light intensities revealed accommodation in firing (Figure 3.5F). Action potential firing was proportional to illumination intensity and could be fitted with a sigmoidal relationship saturating at high light intensities (Figure 3.6A, B). Maximum AP frequencies during sustained photo-stimulation exceeded 60 Hz saturating at high light intensities (Figure 3.6B). To investigate the efficiency of AP firing during trains of brief photo-stimulation, trains of 10 ms light pulses were delivered at increasing frequencies from 10 to 80 Hz in increments of 10 Hz. Photo-stimulation reliably evoked APs with high fidelity for frequencies up to approximately 30 Hz, at which point AP probability decreased dramatically (Figure 3.6C, D).

Figure 3.5: ChR2 activation generates sub-threshold depolarisations and evokes action potentials in layer V pyramidal neurons

Voltage traces in response to photo-stimulation of a layer V pyramidal cell. **A**: Voltage responses to photo-stimulation at different light intensities (light grey: 0.5 mW/mm^2; medium grey: 1 mW/mm^2; dark grey: 2 mW/mm^2; black: 3 mW/mm^2; truncated spike: 4 mW/mm^2). **B**: Voltage responses to somatic current injection (200-600 pA in 100 pA increments; 20 ms) in the same cell as in **A**. **C**: Overlay of action potentials generated by five 10 ms photo-stimulations at the highest light intensity. **D**: Voltage response to somatic current injection (600 pA; 400 ms). **E**: Voltage response to sustained photo-stimulation (4 mW/mm^2) in the same cell as **D**. **F**: Voltage response to photo-stimulation at lower intensity (2 mW/mm^2) shows spike accommodation.

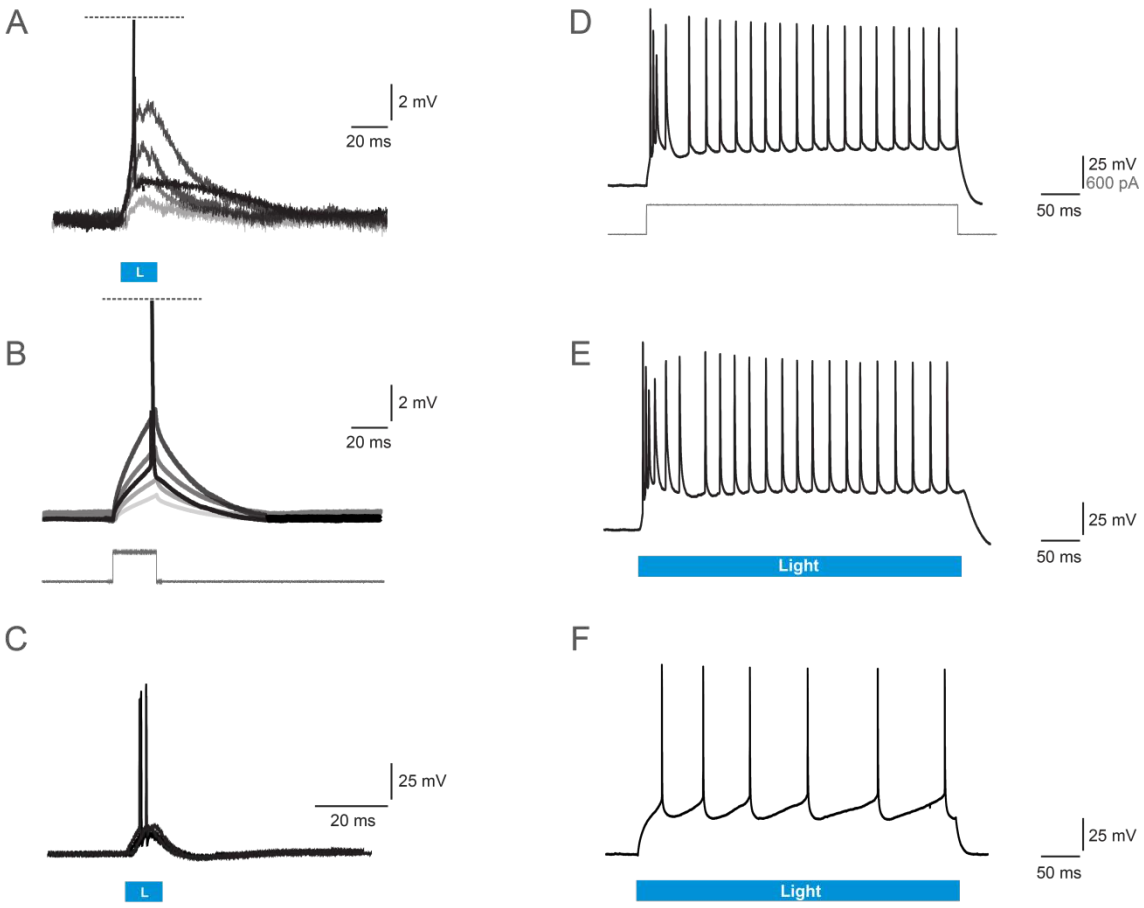
A
2 mV
20 ms
L
B
2 mV
20 ms
C
25 mV
20 ms
L
D
25 mV
600 pA
50 ms
E
25 mV
50 ms
Light
F
25 mV
50 ms
Light

Figure 3.6: Action potential number and frequency are dependent on photo-stimulation intensity

Voltage traces in response to photo-stimulation in a layer V pyramidal cell. **A**: Increasing light intensity generates higher numbers of action potentials. **B**: Relationship between action potential number and light intensity (1 s duration; n = 5; data are mean ± SEM). Data fitted with a sigmoid. **C**: Increasing frequency of brief (10 ms; 5 mW/mm^2) light pulses leads to AP failure at higher frequencies. **D**: Average action potential probability during photo-stimulation at increasing light pulse frequencies.

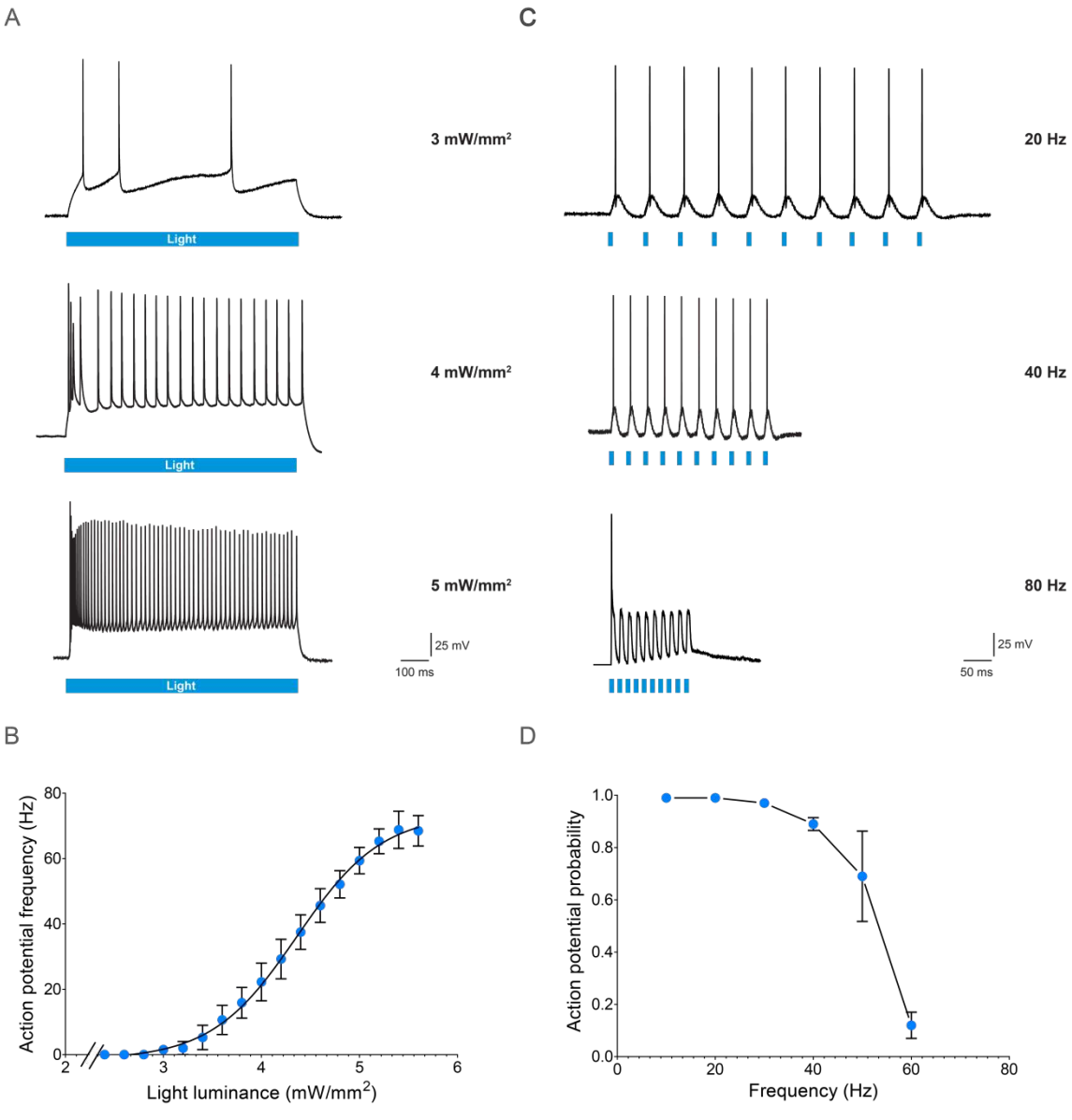
A
3 mW/mm²
Light
4 mW/mm²
Light
5 mW/mm²
Light
25 mV
100 ms
C
20 Hz
40 Hz
80 Hz
25 mV
50 ms
B
Action potential frequency (Hz)
Light luminance (mW/mm²)
D
Action potential probability
Frequency (Hz)

To determine the impact of photo-stimulation duration on action potential probability, trains of light pulses of 2.5 to 20 ms duration were delivered at 15 Hz. AP probability was proportional to light pulse duration, with 2.5 ms illumination only generating sub-threshold events at maximum light intensity (~6 mW/mm^2), while bursts of several spikes were observed during 20 ms duration light pulses (Figure 3.7A-E). It must be noted that individual cells varied significantly in the minimum duration at which action potentials were able to be elicited (data not shown).

To investigate the properties of photo-currents triggered by ChR2 activation, whole-cell voltage-clamp recordings were made from layer V pyramidal neurons. Synaptic transmission was blocked using glutamate receptor antagonists DNQX and AP5 as well as $GABA_A$ receptor antagonist gabazine (10µM DNQX; 50µ AP5; 10µM gabazine). Isolated photo-currents were recorded in voltage clamp in response to full-field illumination with 470 nm light. Photo-stimulation reliably evoked rapid and reproducible inward currents. These photo-currents exhibited an initial transient component which decayed to steady-state (Figure 3.8A, B). Photo-current amplitudes were graded with illumination intensity with increasing light luminance producing increased photo-current amplitude. The relationship between light intensity and peak photo-current amplitude could be fitted with a sigmoid, whereas the relationship between current integral (charge) and light intensity was approximately linear (Figure 3.8C, D).

Figure 3.7: Effect of illumination pulse duration on light-evoked depolarisations in layer V pyramidal cells

A-**D**: Voltage responses to trains of brief light pulses in a layer V pyramidal cell (From top: 2.5, 5, 10, and 20 ms duration; 15 Hz; ~6 mW/mm^2). Light pulse duration indicated by blue bars. **E**: Average number of action potentials generated at different photo-stimulation durations (n = 25; data are mean ± SEM; *p<0.05).

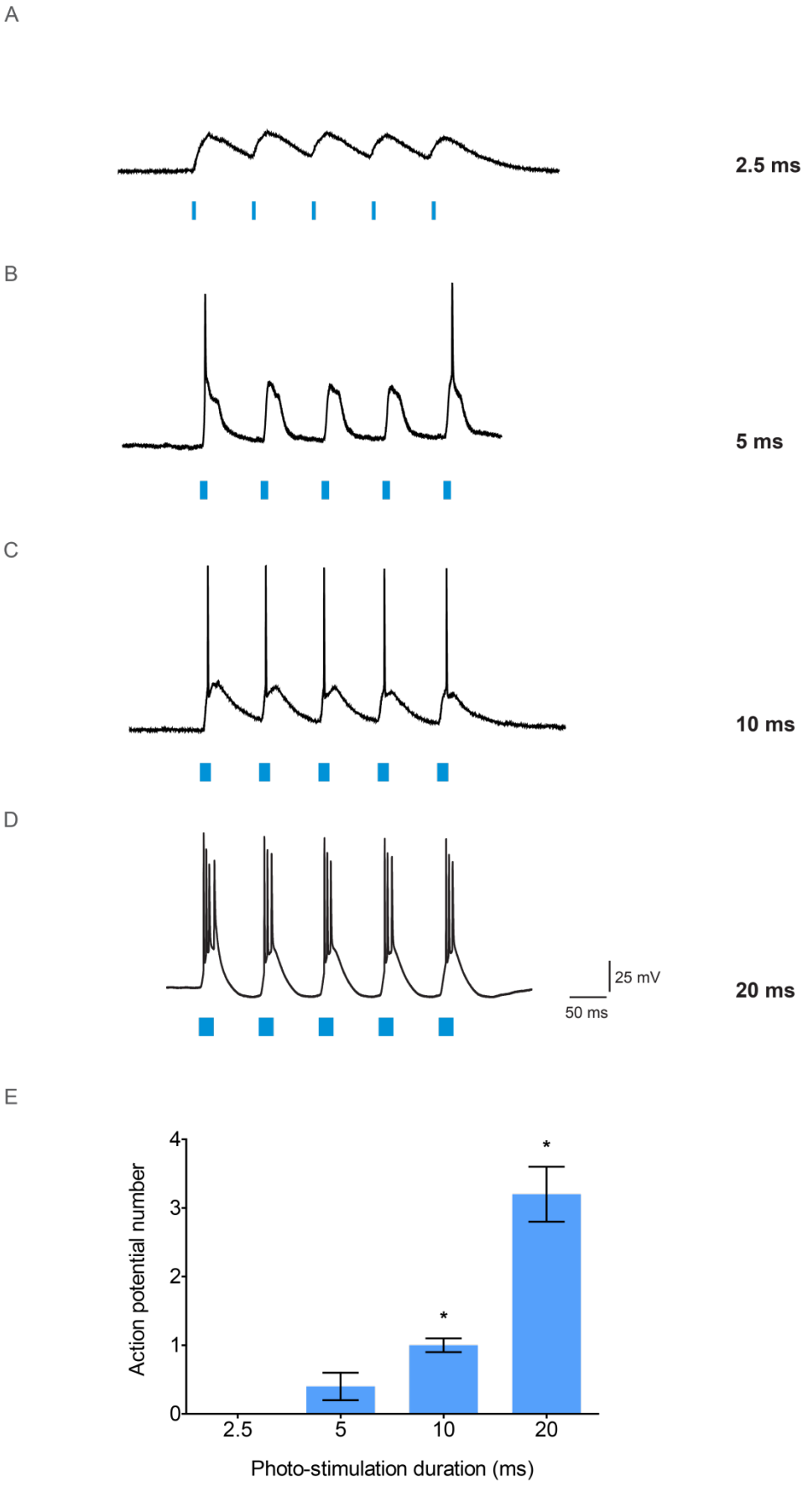
A
2.5 ms
B
5 ms
C
10 ms
D
25 mV
50 ms
20 ms
E
Action potential number
0
1
2
3
4
*
*
2.5
5
10
20
Photo-stimulation duration (ms)

Figure 3.8: Activation of ChR2 produces rapid light-evoked photo-currents in layer V pyramidal neurons

Photo-stimulation generates rapid photocurrents with transient and sustained components in a voltage-clamped layer V pyramidal cell. **A**: Photo-currents produced in response to increasing illumination intensities (light: 0.6 mW/mm^2; light grey: 1.2 mW/mm^2; medium grey: 2 mW/mm^2; dark grey: 3 mW/mm^2; black: ~6 mW/mm^2). **B**: Brief 20ms illumination produces rapid, reproducible photo-currents. **C**: Relationship between photo-current peak amplitude and light intensity. Data fitted with a sigmoid **D**: Relationship between total charge (integral over time) and light intensity (400 ms duration; n = 5; data are mean ± SEM). Data fitted with a linear regression.

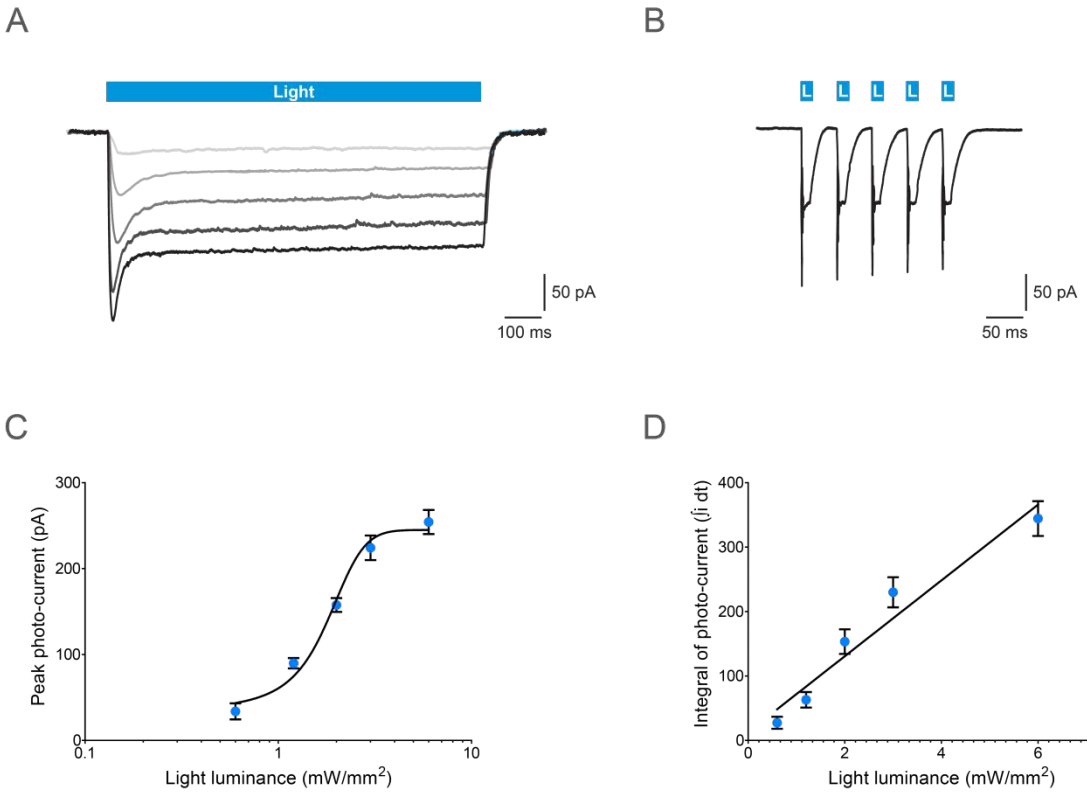
A
Light
50 pA
100 ms
B
L L L L L
50 pA
50 ms
C
Peak photo-current (pA)
300
200
100
0
0.1
1
10
Light luminance (mW/mm2)
D
Integral of photo-current (∫i dt)
400
300
200
100
0
0
2
4
6
8
Light luminance (mW/mm2)

3.3.2 Photo-stimulation of ChR2-expressing neurons

To determine the effect of photo-stimulation in different cell types, pyramidal neurons and interneurons in both layer II/III and V were assessed in response to photo-stimulation. Photo-stimulation could evoke trains of action potentials in all cell types mimicking firing patterns seen during current injection (Figure 3.9A-D; compare with Figure 3.3).

Under control conditions (in the absence of blockers of synaptic transmission) responses to photo-stimulation are likely to contain a presynaptic component arising from connections with neighbouring ChR2 expressing neurons. To identify the contribution of this presynaptic component to light-evoked responses, and to delineate this from direct ChR2 activation, the glutamate receptor antagonists DNQX and AP5, as well as the $GABA_A$ receptor antagonist gabazine, were used to block synaptic transmission (see methods section 3.2.3). Voltage responses were recorded from pyramidal cells and interneurons in layer II/III and V in response to extracellular electrical stimulation and photo-stimulation. Full-field photo-stimulation (365 µm diameter) with 470nm light was presented using 20 ms duration pulses. Sequences of successively alternating extracellular stimulation (100 µs; variable amplitude) and photo-stimulation (3 mW/mm^2) were delivered at 10 second intervals over a 15-to-20 minute period. Excitatory postsynaptic potentials (EPSPs) and light-evoked EPSP-like events were measured before, during, and after the application of synaptic blockers (10 µM DNQX; 50 µM AP-5; 10 µM gabazine).

Figure 3.9: Photo-stimulation in layer II/III and V pyramidal cells and interneurons expressing ChR2

(**A**-**D**) Voltage traces in response to photo-stimulation (4 mW/mm^2) of a layer V pyramidal neuron (**A**; blue), and interneuron (**B**; red), and a layer II/III pyramidal neurons (**C**; green), and interneuron (**D**; orange). Responses demonstrate similar spiking characteristics to that seen with current injection.

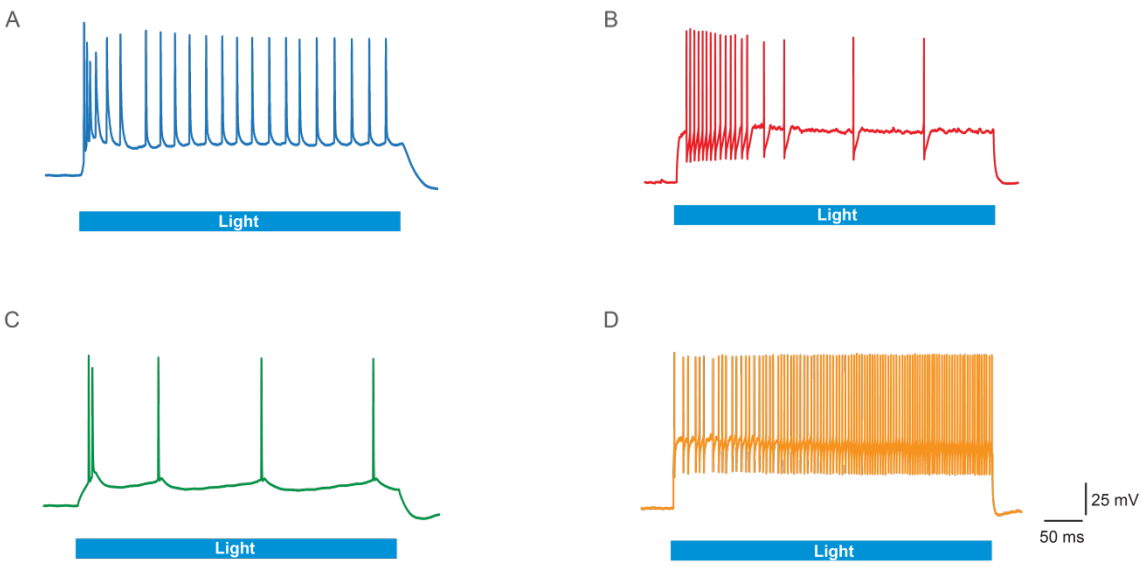
A
Light
B
Light
C
Light
D
Light
25 mV
50 ms

Light-evoked responses in layer V pyramidal cells demonstrated no significant attenuation following the application of synaptic antagonists (Figure 3.10A, C; $P \geq 0.05$). In contrast, EPSPs generated by extracellular stimulation were readily abolished by synaptic blockers in these cells and returned following wash-out (Figure 3.10B,C). Based on the absence of an impact of synaptic blockers, we conclude these cells were directly activated by ChR2. Functional ChR2 expression was found to be present in essentially all (23 out of 24) layer V pyramidal cells (Figure 3.10G). In contrast, synaptic blockers abolished light-evoked responses in 7 out of 25 layer II/III pyramidal neurons (28%; Figure 3.10D,E,G; $P < 0.05$), with light-evoked responses in the majority of layer II/III pyramidal cells (72%) unaffected by synaptic blockers indicating direct activation and therefore functional expression of ChR2 (Figure 3.10G). In cells where light-evoked responses were blocked, these responses returned following wash-out of synaptic blockers (see Figure 3.10D,E). Moreover, direct and indirect (presynaptic) light-evoked responses could be distinguished from one another based on the shape of sub-threshold depolarisation waveforms, with direct responses having a smooth rising and falling phase, whereas indirect responses had inflections similar to synaptic potentials (Figure 3.10F).

Light-evoked responses in layer V interneurons varied in response to application of synaptic blockers. In 18 out of 21 interneurons (86%) light-evoked responses were unaffected by synaptic blockers, while light-evoked responses were abolished by synaptic blockers in 3 out of 21 (14%) of layer V interneurons (Figure 3.10G). Similarly, light-evoked responses were unaffected by synaptic blockers in the majority of interneurons in layer II/III (14 out of 18; 78%) whereas light-evoked responses in the remaining 4 out of 18 cells (22%) were

Figure 3.10: Pre and post-synaptic components to light evoked responses

A: Sub-threshold response in a layer V neuron generated via ChR2 activation (3 mW/mm^2) without (left) and with (right) synaptic transmission blocked by bath application of glutamatergic antagonists DNQX and AP5, and the $GABA_A$ receptor antagonist gabazine (yellow bar). **B**: Sub-threshold response in a layer V neuron generated via extracellular stimulation without (left) and with (right) synaptic blockers (yellow bars). **C**: Amplitude of sub-threshold responses in a layer V pyramidal neuron evoked by extracellular stimulation (black) and photo-stimulation (blue) during perfusion with glutamatergic antagonists DNQX and AP5, and the $GABA_A$ receptor antagonist gabazine (yellow bar). **D**: Same as in **C** in a layer II/III pyramidal neuron. **E**: Pooled data for layer II/III pyramidal cells (n = 25). Upper panel shows cells where light-evoked responses were unaffected by synaptic antagonists (8 cells). Lower panel shows cells where light-evoked responses were blocked (17 cells). **F**: Examples of sub-threshold responses generated via direct ChR2 activation (left) or via indirect (pre-synaptic) activation (right) during photo-stimulation in a layer II/III pyramidal neurons. **G**: Pooled data for ChR2 expression in different cell types. Blue: number of cells directly activated by photo-stimulation. Red: number of cells indirectly activated by photo-stimulation.

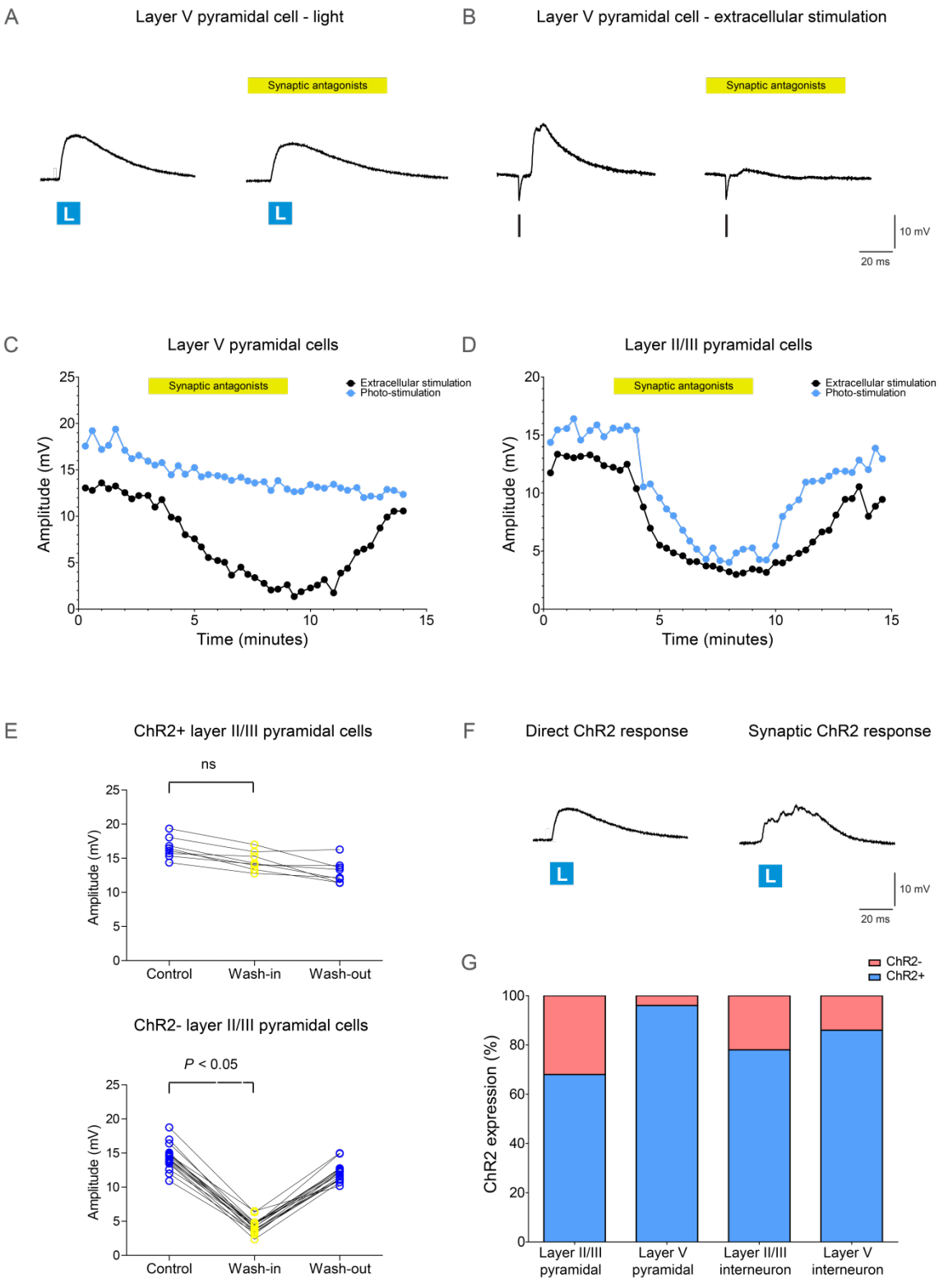
A
Layer V pyramidal cell - light
Synaptic antagonists
L
L
B
Layer V pyramidal cell - extracellular stimulation
Synaptic antagonists
10 mV
20 ms
C
Layer V pyramidal cells
Synaptic antagonists
Extracellular stimulation
Photo-stimulation
Amplitude (mV)
Time (minutes)
D
Layer II/III pyramidal cells
Synaptic antagonists
Extracellular stimulation
Photo-stimulation
Amplitude (mV)
Time (minutes)
E
ChR2+ layer II/III pyramidal cells
ns
Amplitude (mV)
Control
Wash-in
Wash-out
ChR2- layer II/III pyramidal cells
P < 0.05
Amplitude (mV)
Control
Wash-in
Wash-out
F
Direct ChR2 response
Synaptic ChR2 response
L
L
10 mV
20 ms
G
ChR2-
ChR2+
ChR2 expression (%)
Layer II/III pyramidal
Layer V pyramidal
Layer II/III interneuron
Layer V interneuron

blocked by synaptic antagonists (Figure 3.10G). All interneurons expressing ChR2 generated action potentials when stimulated with higher light intensities (6 mW/mm2), like those used in the experiments described in Chapter Four and Five of this thesis. These data show that ChR2 expression is not restricted to layer V pyramidal cells, and is present in the majority of layer II/III pyramidal cells as well as interneurons in layer II/III and V in this mouse model.

3.4 Discussion

The advent of optogenetic methods has resulted in the development of multiple transgenic mouse lines expressing light activated channels such as channelrhodopsin-2 (ChR2). Previous studies have demonstrated ChR2 expression in layer V cortical pyramidal neurons in founder line 18 Thy-1-ChR2-YFP mice. The present study was undertaken to determine the distribution of ChR2 expression in different cells types the somatosensory cortex in this model, and to analyse the functional properties of ChR2 activation in the context of the use of this model for investigating cortical circuitry.

The principle findings of this study are two-fold. Firstly, we show that Thy-1 driven ChR2 expression is markedly heterogeneous in different cortical neurons of the mouse somatosensory cortex, with non-uniform expression throughout all cortical layers. Secondly, investigation of the functional properties of ChR2 activation demonstrates the capacity to precisely control action potential generation in individual neurons and thereby manipulate excitatory and inhibitory synaptic transmission in cortical circuits.

To accurately characterise ChR2 expression patterns identification and classification of neuron classes is required. Pyramidal neurons and interneurons throughout the somatosensory cortex have been well described, both in terms of their morphology and electrophysiology (Connors and Gutnick, 1990; Spruston, 2008). While diversity is found within these populations, they can be defined and distinguished from one another based on a number of distinct electrical properties and cellular architectures. Detailed identification of cortical

neurons enabled evaluation of the extent of ChR2 expression in different neuron populations in the Thy-1-ChR2-YFP model. Despite the relatively widespread use of this model, little information exists regarding the expression patterns in different cortical neurons. ChR2 was found to be abundantly expressed in layer V pyramidal neurons, with expression found in 96% of cells, with robust action potentials evoked even with low illumination intensities. These results are consistent with previous findings in layer V pyramidal cells in this model (Arenkiel *et al.*, 2007; Wang *et al.*, 2007). Surprisingly, ChR2 expression was also observed in 72% of layer II/III pyramidal neurons (Figure 3.10). Furthermore, ChR2 expression was found in the majority of fast-spiking interneurons in both layer II/III and V (78% and 86% respectively), suggesting Thy-1 transgene expression is not restricted to layer V cells. Together these data highlight the heterogeneous distribution of ChR2 expression in this Thy-1 driven ChR2 model. These observations have implications for the use of this animal model in investigating cortical circuitry. Whether non-expressing pyramidal cells in layer II/III represent different sub-type populations remains unclear. Likewise, the presence of non-expressing interneurons in both layers II/III and V may signify that Thy-1-driven ChR2 is targeted to certain interneuron populations but not others. The implications of these findings are further discussed in Chapter Six.

Importantly, the introduction of ChR2 into cortical neurons appears not to alter their intrinsic properties. Comparing ChR2 expressing cells with non-expressing cells in the same slice or in wild-type littermates revealed negligible differences in their electrical properties. ChR2-positive interneurons in layer II/III, however, did show differences in action potential threshold and half-width from ChR2-

negative interneurons in the same cortical layer (Table 3.3), characteristics which were found to differ considerably within cortical interneuron populations. This observation may indicate some differential expression of ChR2 in different interneurons cell types, although the number of ChR2 negative cells was small. Additionally, no signs of cellular degeneration or altered morphology were observed in ChR2-positive cells compared with neighbouring ChR2-negative cells in the same slice (data not shown). These findings substantiate previous evidence that ChR2 expressing cells demonstrate morphological and electrophysiological properties indistinguishable from their wild-type counterparts (Arenkiel *et al.*, 2007).

Recruitment of ChR2 has been demonstrated to be directly proportional to the intensity of photo-stimulation, enabling responses to be titrated by adjusting illumination intensity (Boyden *et al.*, 2005). In addition to defining the light intensity requirements for desired photo-currents and associated membrane depolarisations, it was important to determine the dependence of photo-stimulation on cell depth. Experiments demonstrated an exponential decay in total transmitted light power as a function of tissue depth (Figure 3.2). These estimates correspond well with existing evidence concerning the propagation of 470 nm light in rodent cortical tissue (Aravanis *et al.*, 2007) and indicate that photo-evoked responses are likely to vary with the depth of recorded neurons.

Photo-currents mediated by ChR2 activation exhibited an initial transient component decaying rapidly to a steady-state current, suggesting an inactivation phase. Interestingly, while this steady-state current was maintained during prolonged photo-stimulation, subsequent light pulses elicit reduced peak

transient currents (Figure 3.8). Similar observations have been made by others (Boyden *et al.*, 2005; Nagel *et al.*, 2005; Zhang *et al.*, 2006). The rapid onset kinetics of ChR2 activation enabled precise temporal control of action potentials. Additionally, photo-current amplitude was directly proportional to illumination intensity enabling light-evoked responses to be titrated in a controlled manner (Figure 3.8).

Light-evoked membrane depolarisations have been shown to exhibit an exponential relationship with light dose (light power x duration) indicating a temporal component to the ChR2-conductance (Zhang and Oertner, 2007). Indeed, both ChR2-evoked sub-threshold depolarisations and action potentials were dependent on photo-stimulation duration (Figure 3.5). This was particularly evident at very short durations where the reliability of action potential generation fell dramatically with light pulses below 5 ms duration, even at maximum light intensity (Figure 3.6).

Consistent with previous findings, ChR2 activation was capable of generating action potential trains with frequencies similar to that achieved with direct current injection (Wang *et al.*, 2007). In layer V pyramidal cells action potential firing saturated at frequencies around 70 Hz (Figure 3.6) suggesting supra-threshold responses are limited by the intrinsic properties of the neuron and not the properties of ChR2 activation.

In conclusion, this study has demonstrated that the Thy-1 driven ChR2 mouse exhibits a varying distribution of ChR2 expression in different neurons of somatosensory barrel cortex. These observations are likely to result from a

position effect variegation arising from transgene regulation by the Thy-1 promoter (Feng *et al.*, 2000). While variability in expression patterns in the mouse model limit the ability to achieve selective responses in defined cell types, quantification of expression patterns (as performed in this study), together with the fast kinetics and spatiotemporal control afforded by ChR2, indicate the Thy-1-ChR2 mouse model is a valuable model for investigating cortical circuitry.

CHAPTER FOUR

AN OPTOGENETIC OPTICAL INTERFACE FOR CIRCUIT MAPPING

4.1 Introduction

This chapter describes the design and application of an optical interface capable of spatiotemporally precise photo-stimulation for optogenetics. Optogenetic methods have become instrumental in neuroscience research. The widespread application of optogenetic technologies has led to an evolving toolbox of photo-sensitive compounds (Zhang *et al.*, 2011; Asrican *et al.*, 2013). While these developments enable photo-sensitive proteins to be targeted to specific neuronal subpopulations, optical techniques available to activate these proteins remain relatively limited. Typically, excitation of light-sensitive optogenetic proteins is achieved by fluorescent lamps or light-emitting diodes (LEDs; often coupled with fibre optics), or using scanning lasers coupled to confocal or two-photon microscopes (Aravanis *et al.*, 2007; Wang *et al.*, 2007). These techniques rely on either wide-field or targeted illumination with little flexibility in dynamically probing multiple regions simultaneously.

To exploit the full potential of optogenetics an optical tool with high spatiotemporal and chromatic precision as well as the ability to simultaneously stimulate multiple areas in real-time is required. To produce a photo-stimulation system possessing these capabilities a novel* projector-based illumination system was developed. This illumination system was applied to a series of

experiments designed to assess the capabilities of this system for photo-stimulation of ChR2.

Three proof-of-principle studies were conducted to assess the application of this method. Firstly, sub-cellular dendritic photo-stimulation was used to investigate the somatic impact of distal dendritic inputs in cortical pyramidal neurons. Secondly, projected light patterns were used to activate different cortical layers in an effort to map synaptic connectivity in the mouse somatosensory barrel cortex. Finally, the projector-based illumination system was used to activate long-range thalamocortical projections to pyramidal neurons in somatosensory barrel cortex.

* Following this research other research groups (Stirman *et al.*, 2011; Sakai *et al.*, 2013) developed similar illumination technologies to the one outlined in this thesis.

4.2 Methods

4.2.1 Tissue slice preparation and neuron identification

Brain tissue slices from ChR2-YFP mice were sectioned in the coronal plane as described in the General Methods (section 2.2). Primary somatosensory cortex and the laminar distribution of cells were identified as described previously (section 3.2.1). For analysis of long-range connectivity, a well-established somatosensory thalamocortical brain slice preparation was employed (Agmon and Connors, 1991). Briefly, tissue slices were sectioned at 55º off-sagittal and 10º off-coronal with thicknesses of 400 µm. Sectioning procedures were otherwise identical to those described previously in the General Methods (section 2.2). This slice preparation preserves anatomical and functional connectivity between the ventrobasal thalamus and somatosensory barrel cortex. Primary somatosensory (S1) barrel cortex was identified based on the appearance of barrels visible under bright-field illumination and positioning relative to rostrocaudal location using a brain atlas (Franklin and Paxinos, 2008). Thalamic structures were identified according to anatomical markers described for the thalamocortical slice preparation (Agmon and Connors, 1991).

Neurons were identified as described previously (section 3.2.1). Pyramidal neurons were distinguished from spiny stellate neurons in layer IV by the presence of extended apical dendrites. Whole-cell somatic patch-clamp recordings were made from visualised pyramidal neurons and interneurons in layers II/III, IV, and V and electrophysiological properties determined from voltage responses to current injection. Intracellular solution containing biocytin

was used to permit morphological reconstructions of recorded cells (as described in the General Methods section 2.5).

4.2.2 Photo-stimulation

To produce a dynamic photo-stimulation system capable of precise spatial, temporal, and chromatic control, an innovative projector-based illumination system was developed. This photo-stimulation system employed the use of a widely available commercial video projector (Epson; EB-1770W, Japan). This system utilises a metal halide mercury lamp which emits light through a liquid crystal spatial light modulator. The individual pixel elements of this liquid crystal display (LCD) create an image composed of pixels defined by a computer video output. In a standard LCD projector this projected image is typically transmitted through a zoom lens and a diverging projection lens. Removal of this lens permits a primary image plane with a short (5-10 cm) focal length. The addition of an in-line tube lens centred along the optical axis of the epifluorescence port of the microscope (Zeiss; Axioskop, Germany) enabled this primary image plane to be relayed through the microscope objective where the magnification (or demagnification in this case) is determined by the ratio of the focal lengths of the two lenses (the native zoom lens and the additional microscope tube lens). The resultant de-magnified image was then projected onto the tissue slice (Figure 4.1).

Image processing and illumination output was controlled by a programming-based computing environment software (MathWorks; MATLAB, USA) on a computer (Dell Inc.; OptiPlex 990, USA). Custom software was written in

Figure 4.1: Projector-based photo-stimulation system

Schematic of the illumination system. A liquid crystal display (LCD) projector is integrated with a standard epifluorescent microscope enabling projection of de-magnified images directly onto the tissue slice (Image produced by Vince Daria).

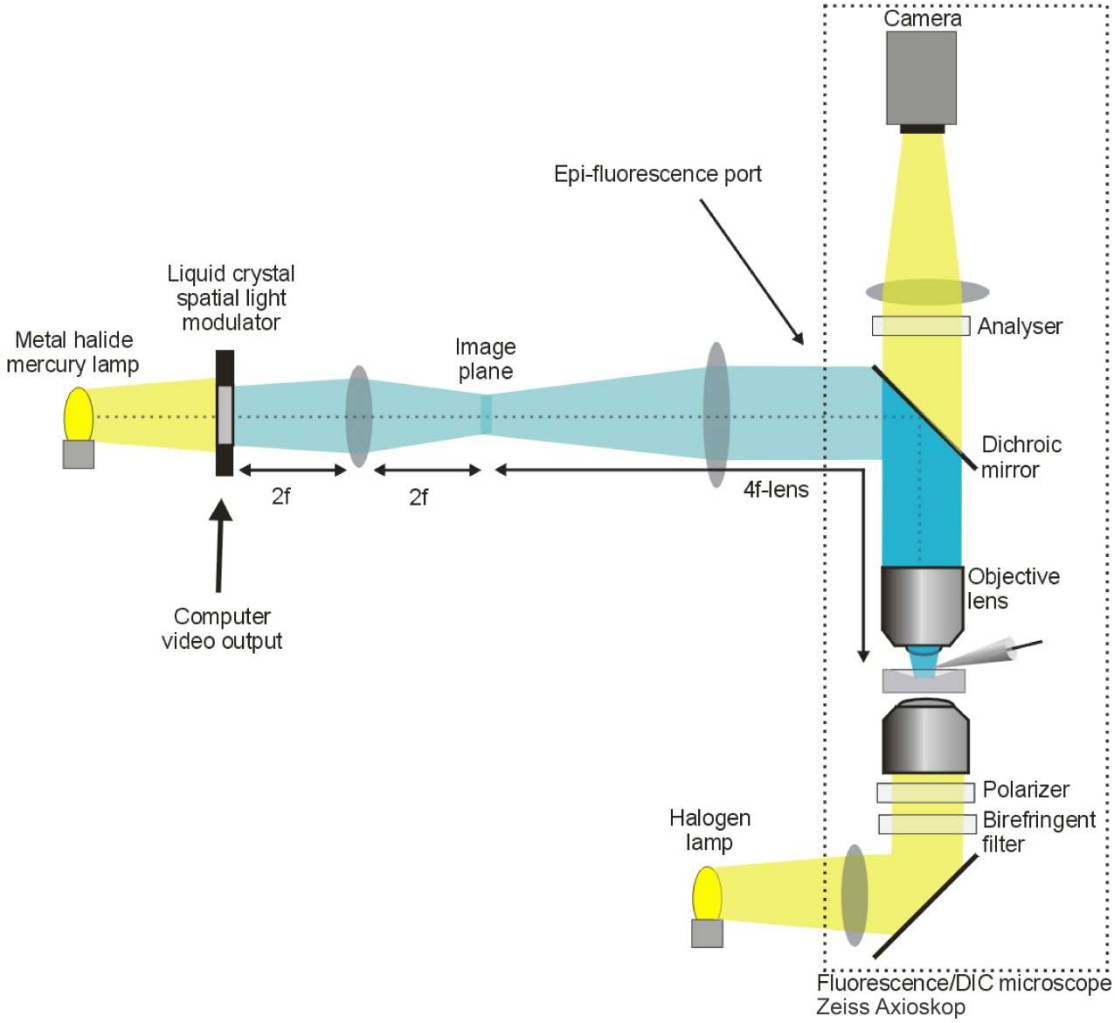
Camera
Epi-fluorescence port
Liquid crystal
spatial light
modulator
Metal halide
mercury lamp
Image
plane
Analyser
Dichroic
mirror
2f
2f
4f-lens
Objective
lens
Computer
video output
Polarizer
Halogen
lamp
Birefringent
filter
Fluorescence/DIC microscope
Zeiss Axioskop

MATLAB® and comprised execution scripts of input functions to control the spatial and temporal resolution, and chromatic composition of video output patterns. Synchronisation with a primary computer (Apple Macintosh; Power Mac G4, USA) running acquisition software (Axon Instruments; Axograph, USA) was achieved via a computer interface (Instrutech Corporation; ITC-16, USA) linked to the secondary computer parallel port and controlled with parallel port access software (Parport 2000, USA). Both the wavelength (colour) and intensity of the LCD red-green-blue (RGB) channels were controlled by 8-bit integers in MATLAB®. Light power was measured for linear software-controlled output using a power meter (Thorlabs; PM100A, USA). Actual light power output was not linearly related to software-controlled output voltage (Figure 4.2A,B). As a result in experiments where the relative light intensity was of importance, the non-linear relationship between light power output and software-controlled output voltage was determined and used to scale the software-controlled output voltage to achieve a linear relationship (Figure 4.2C). The maximum light power density produced through a 60x objective was 8.8 mW/mm^2. For experiments utilising lower magnifications, light power densities were measured accordingly.

To avoid inaccuracies in spatial spread of illumination patterns due to lens contrast transfer functions, illumination resolutions that were software defined in terms of pixel value were measured and corrected for at the tissue slice plane using micro-ruler measures at the focal plane. Temporal resolution was limited by the frequency of the LCD projector – in this case 60 Hz. The theoretical limit of 16.67 ms imposed by the refresh rate of the projector dictated the minimum duration of light exposures in these experiments using this system (~20 ms).

Figure 4.2: Relationship of software-controlled output and projector output power

Measured output power at 470 nm (% of maximum) as a function of software-controlled output for the full projector output range (**A**), and the experimental range of intensities used for ChR2 photo-stimulation (**B**). The black line in (**A**) represents a linear fit, whereas the red curve in (**B**) represents the fit using a quadratic (equation indicated). **C**: Corrected output generated by adjusting software-controlled output according to the equation in (**B**).

A

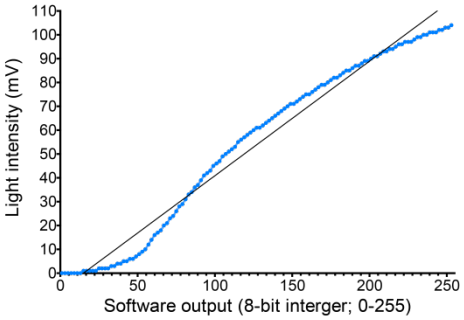
Light intensity (mV)
110
100
90
80
70
60
50
40
30
20
10
0
0
50
100
150
200
250
Software output (8-bit interger; 0-255)

B

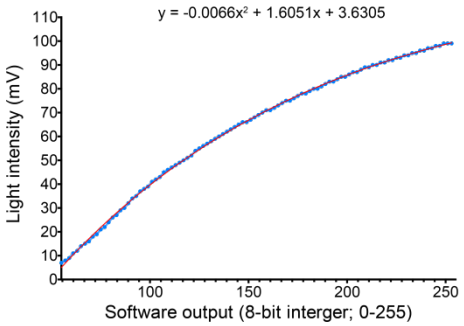
y = -0.0066x² + 1.6051x + 3.6305
Light intensity (mV)
110
100
90
80
70
60
50
40
30
20
10
0
100
150
200
250
Software output (8-bit interger; 0-255)

C

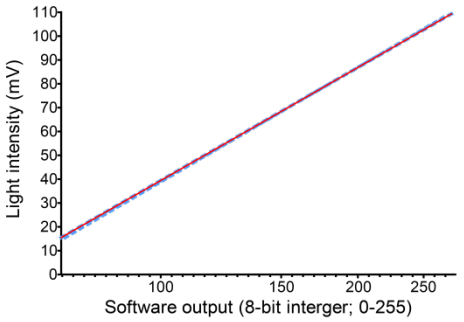
Light intensity (mV)
110
100
90
80
70
60
50
40
30
20
10
0
100
150
200
250
Software output (8-bit interger; 0-255)

Illumination output by the projector-based illumination system occurred with a delay following triggering by the acquisition software, resulting from both software (MATLAB® execution scripts) and hardware (LCD activation). This delay was measured as 12.4 ± 2.2 ms (n = 10). All figures were corrected for this delay to represent the onset and offset of photo-stimulation rather than when the light source was triggered.

4.2.3 Pharmacology

In some experiments synaptic transmission was blocked using glutamate receptor antagonists DNQX (10 µM) and AP5 (50 µM) as well as the $GABA_A$ receptor antagonist gabazine (10 µM). Synaptic antagonists were delivered in ACSF via a gravity drip-feed at a flow rate of 2 ml/minute.

4.3 Results

4.3.1 Photo-stimulation of subcellular domains

To determine the efficiency of the projector-based photo-stimulation system in investigating sub-cellular information processing, somatic recordings were made from layer V pyramidal neurons while photo-stimulating specific dendritic sites either in isolation or simultaneously. Using a functional illumination field spanning the entire structure of an individual cell enabled rapid, precisely controlled generation of light-evoked inputs across the cell.

To determine the somatic impact of light-evoked inputs generated at predetermined dendritic locations, whole-cell somatic patch-clamp recordings were made from layer V pyramidal neurons. Somatic depolarisations were then recorded in response to successively distal photo-stimulation sites (Figure 4.3A). Photo-stimulation was delivered in circular light beams 50 µm in diameter targeted from 250 µm to 750 µm distal from the soma towards the pia in 250 µm intervals. Light pulses were presented in series of 5 pulses of 20 ms duration at 15 Hz with a power density of 8.8 mW/mm^2 (Figure 4.3B). Experiments were performed in the presence of synaptic blockers (10 µM DNQX; 50 µM AP5; 10 µM gabazine) to isolate light-evoked responses due to direct activation of ChR2 in the recorded neuron.

Direct photo-stimulation of the soma evoked robust bursts of actions potentials with multiple spikes generated in response to all light pulses in the train (Figure 4.3B). Action potentials were also reliably produced during optical activation at

Figure 4.3: Somatic depolarisations in response to distal dendritic photo-stimulation in layer V pyramidal neurons

A: Reconstructed layer V pyramidal neuron illustrating photo-stimulation sites at the soma and at distances of 250 µm, 500 µm, and 750 µm distal to the soma. **B**: Somatic depolarisations in response to successively distal photo-stimulation (8.8 mW/mm^2) sites as indicated in (**A**). **C**: Relationship between amplitude of somatic light-evoked depolarisations (at 50 % maximum light intensity; 4.4 mW/mm^2) and the distance of the light illumination site from the soma (data are mean ± SEM; data fit with an exponential; n = 5). **D**: Example somatic voltage trace in response to simultaneous photo-stimulation of dendritic sites at 500 µm and 750 µm distal to the soma (black trace) and the linear sum of responses at each of these sites alone (blue trace).

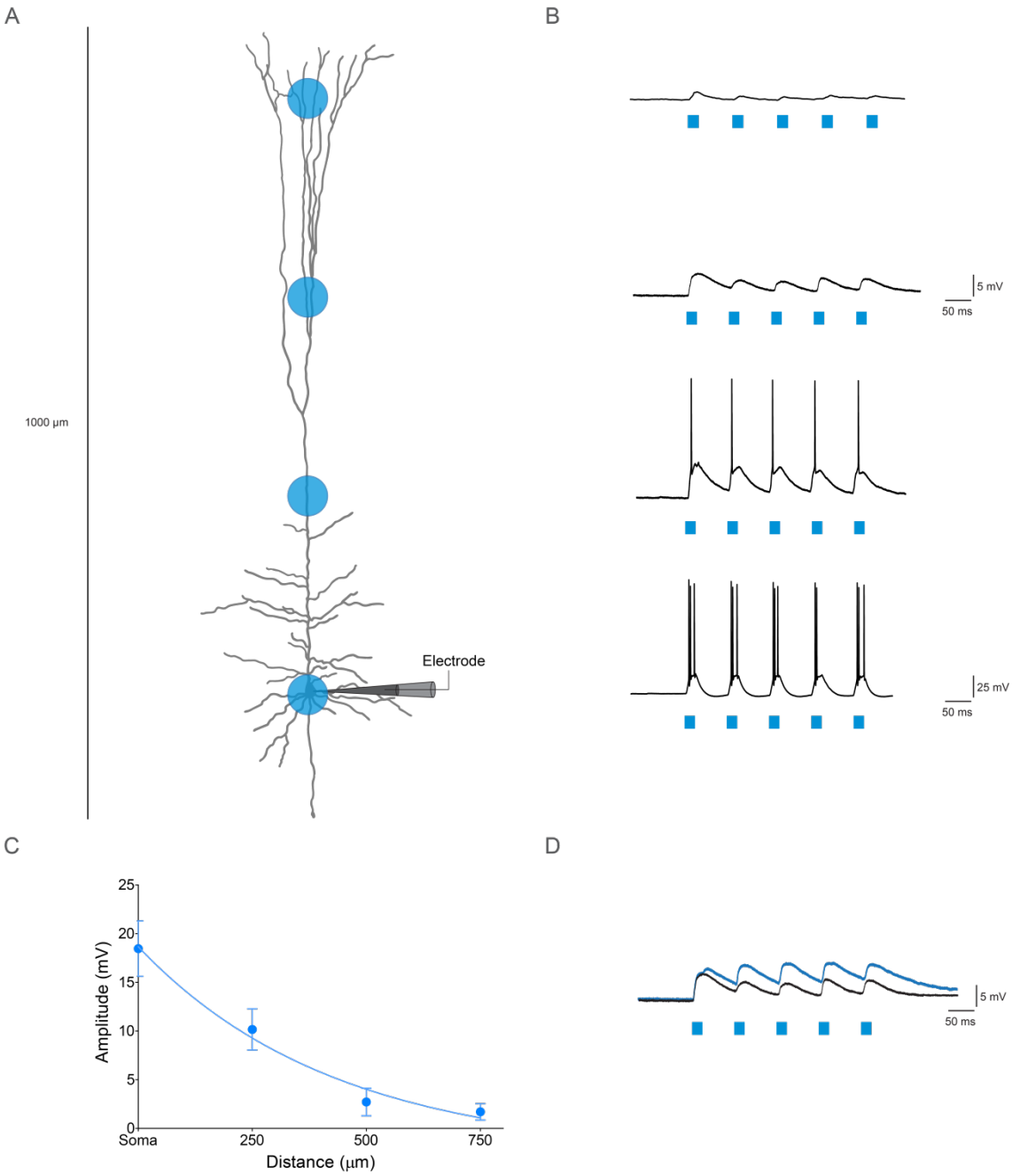
A
1000 µm
Electrode
B
5 mV
50 ms
25 mV
50 ms
C
Amplitude (mV)
25
20
15
10
5
0
Soma
250
500
750
Distance (µm)
D
5 mV
50 ms

distances 250 µm distal to the soma, while activation of more distal sites only produced sub-threshold depolarisations (Figure 4.3B). The somatic amplitude of light-evoked depolarisations decreased exponentially with increasingly distance of activation sites from the soma (Figure 4.3C). Simultaneous photo-stimulation of dendritic sites at 500 µm and 750 µm distal to the soma showed sub-linear spatial summation (Figure 4.3D).

4.3.2 Mapping functional connectivity in layer II/III and IV somatosensory cortex

To assess the capabilities of the projector-based photo-stimulation system for circuit mapping a series of experiments were designed to map synaptic network connectivity in the mouse somatosensory cortex. These experiments utilised the heterogeneous Thy-1-driven expression of ChR2 found in layer II/III and IV somatosensory cortex (see Chapter Three) to isolate non-ChR2 expressing cells in these layers. This enabled the recording of presynaptic light-evoked responses arising from synaptic connections from ChR2-expressing neurons in the absence of direct photo-stimulation.

To investigate synaptic connectivity in layer II/III of somatosensory barrel cortex, whole-cell patch-clamp recordings were made from the somata of ChR2-negative pyramidal neurons and interneurons within barrel columns. Recorded neurons were identified based on the laminar location of their somata, their cellular architecture, and their intrinsic electrical properties (described in Chapter Three). Targeted photo-stimulation was used to stimulate neighbouring presynaptic neurons at predetermine locations.

Photo-stimulation was delivered in 50 µm square fields presented pseudo-randomly across a grid spanning 600 µm x 400 µm through cortical layers I to V and across at least two adjacent barrel columns (Figure 4.4). Each field received light pulses of 20 ms duration at a power density of 2.9 mW/mm^2. Light-evoked synaptic responses were recorded as somatic membrane depolarisations and averaged across five trials for each photo-stimulation field.

Depolarisation amplitudes were correlated with the illumination region and used to construct 'heat' maps representing the strength of synaptic input to each recorded neuron during activation of that illumination region. All experiments were performed in the presence of the $GABA_A$ receptor antagonist gabazine (10 µM) to isolate excitatory synaptic responses. To confirm that responses were due to activation of presynaptic inputs, rather than via direct activation of ChR2 in the recorded neuron, the glutamate receptor antagonists DNQX (10 µM) and AP5 (50 µM) were applied to block excitatory synaptic transmission.

Initially, illumination was targeted to ChR2-expressing layer II/III pyramidal cells in the presence of synaptic antagonists to determine the somatic impact of light-evoked inputs generated by direct ChR2 activation. At an illumination intensity of 2.9 mW/mm^2 action potentials were generated only in response photo-stimulation of the soma or illumination fields within 100 µm of the soma (Figure 4.5). Action potential probability (percentage of cells where APs were evoked) fell to 0 at distances 150 µm distal to the soma (n = 8). These data suggest that action potentials are primarily evoked by light activation of the soma at this photo-stimulation intensity, creating a proxy for somatic location during circuit mapping.

Figure 4.4: Projector-based photo-stimulation in somatosensory barrel cortex

A: Schematic of the experimental arrangement. The photo-stimulation illumination grid (grey squares) is shown overlaid onto a barrel column (rounded rectangles in layer IV). Also indicated is the position of the recorded cell (red) and illumination locations (numbered blue squares with circles around them). **B**: Light-evoked postsynaptic responses recorded from cell in (**A**) during illumination (2.9 mW/mm^2) at locations 1 to 3 indicated in (**A**).

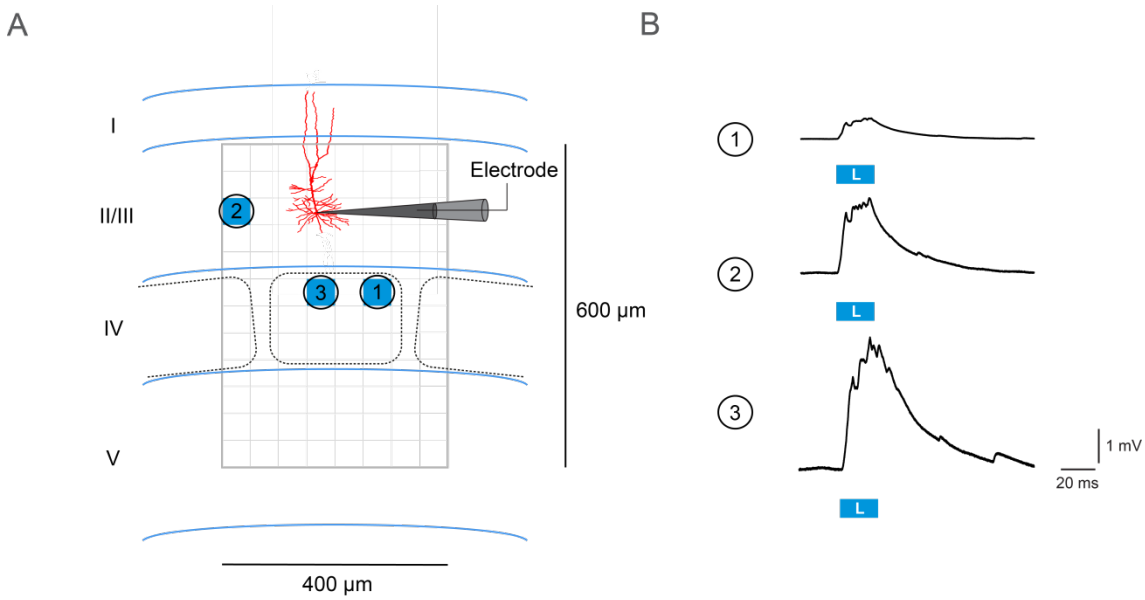
A
B
I
II/III
IV
V
Electrode
2
3
1
600 µm
400 µm
1
2
3
L
L
L
1 mV
20 ms

Figure 4.5: Somatic response to direct ChR2 photo-stimulation of a layer II/III pyramidal neuron at different locations

Reconstructed layer II/III pyramidal neuron showing photo-stimulation illumination grid (grey squares). Colour-coded fields indicating the strength of somatic depolarisation (scale: bottom, right) for fields (squares) where photo-stimulation (2.9 mW/mm^2) generated a response in the recorded cell. Experiments performed with synaptic blockers (10 µM DNQX; 50 µM AP5; 10 µM gabazine). Blank fields did not evoke detectable somatic depolarisation. Inset (right, top): Action potential probability for illumination of somatic and proximal dendritic fields (n = 8).

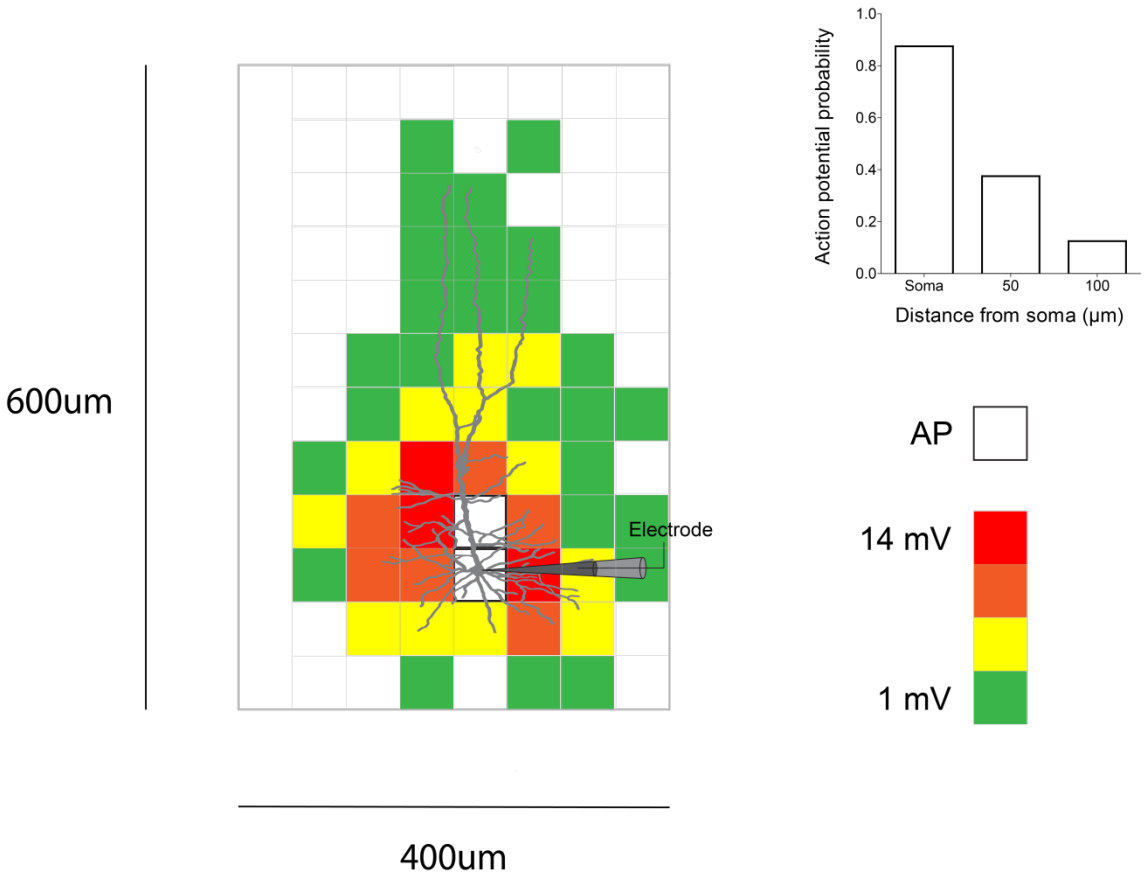
600um
Electrode
400um
Action potential probability
1.0
0.8
0.6
0.4
0.2
0.0
Soma
50
100
Distance from soma (µm)
AP
14 mV
1 mV

Layer II/III pyramidal cells were found to receive most of their excitatory synaptic input from fields in layer IV and II/III (Figure 4.6A). Approximately 51% of tested photo-stimulated fields in layer IV elicited excitatory responses in layer II/III pyramidal neurons, with responses evoked from 38% of fields in layer II/III and 15% of fields in layer V (Figure 4.6E; n = 9). To determine the average strength of excitatory inputs originating in different layers, mean response amplitude was calculated across light-illumination grid rows for all detectable light-evoked responses (excluding blank fields). The mean strength of excitatory inputs arising from both layer IV and II/III was significantly stronger than that in layer V (Figure 4.6F; n = 9), revealing a profile of input relative to the soma which was consistent among layer II/III pyramidal cells recorded within the same slice and across different slices (Figure 4.6C).

The synaptic distribution patterns in layer IV neurons revealed that most of their excitatory synaptic input arises from neighbouring cells within layer IV and layer V, with approximately 43% of photo-stimulated fields in layer IV generating excitatory responses in contrast to 37% in layer V and 15% in layer II/III (Figure 4.6E; n = 7). On average, the amplitude of inputs arising from layer IV was also significantly stronger than that in layer II/III (Figure 4.6C,F; n = 7)

To investigate the spatial distribution of synaptic inputs onto interneurons in somatosensory barrel cortex, whole-cell recordings were made from layer II/III and IV interneurons. Layer II/III interneurons received the majority of their excitatory synaptic inputs from both layer II/III and IV (Figure 4.7A). Photo-stimulation in layer IV generated responses in approximately 71% of fields

Figure 4.6: Functional connectivity of layer II/III and IV neurons

Typical "heat" maps of the strength of excitatory synaptic inputs to layer II/III pyramidal cells (**A**) and IV (**B**) neurons (recorded in the presence of gabazine). Black triangle indicates somatic location of recorded cell. Colour-coded fields indicate input strength for fields where photo-stimulation (2.9 mW/mm^2) generated responses in the recorded cell. Blank fields did not evoke a synaptic response. Dotted rounded rectangles indicate approximate location of barrels. Insets show heat maps after addition of DNQX and AP5. **C** and **D**: Vertical profiles of the distribution of synaptic input relative to the somata of recorded cells in **A** and **B** obtained by averaging responses across rows (n = 9 and 7 respectively; data are mean ± SEM). **E**: Per cent of total photo-stimulated fields in each cortical layer eliciting excitatory synaptic responses in layer II/III and IV neurons. **F**: Mean strength of excitatory synaptic inputs to layer II/III and IV neurons arising from each cortical layer (data are mean ± SEM; $*p<0.05$).

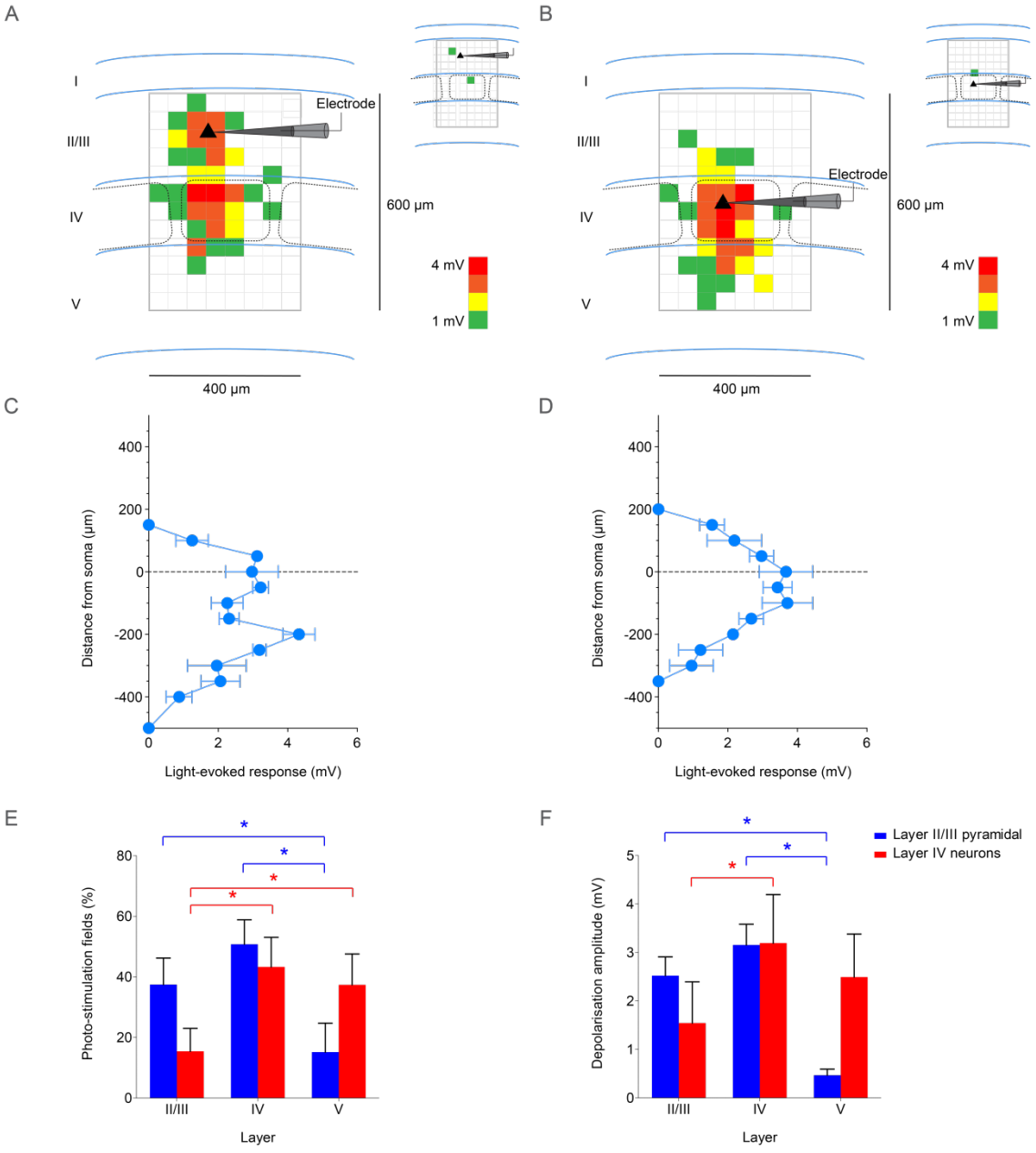
A
I
II/III
IV
V
Electrode
600 µm
4 mV
1 mV
400 µm
B
I
II/III
IV
V
Electrode
600 µm
4 mV
1 mV
400 µm
C
Distance from soma (µm)
400
200
0
-200
-400
0
2
4
6
Light-evoked response (mV)
D
Distance from soma (µm)
400
200
0
-200
-400
0
2
4
6
Light-evoked response (mV)
E
Photo-stimulation fields (%)
80
60
40
20
0
II/III
IV
V
Layer
F
Depolarisation amplitude (mV)
5
4
3
2
1
0
II/III
IV
V
Layer
Layer II/III pyramidal
Layer IV neurons

Figure 4.7: Functional connectivity of layer II/III and IV interneurons

Typical “heat” maps of the strength of synaptic inputs to layer II/III (**A**) and IV (**B**) interneurons (recorded in the presence of gabazine). Magenta ellipse indicates somatic location of recorded cell. Colour-coded fields indicate input strength for fields where photo-stimulation (2.9 mW/mm^2) generated responses in the recorded cell. Blank fields did not evoke a synaptic response. Dotted rounded rectangles indicate approximate location of barrels. Insets show heat maps after addition of DNQX and AP5. **C** and **D**: Vertical profiles of the distribution of synaptic input relative to the somata of recorded cells in **A** and **B** obtained by averaging responses across rows (n = 7 and 6 respectively; data are mean ± SEM). **E**: Per cent of total photo-stimulated fields in each cortical layer eliciting excitatory synaptic responses in layer II/III and IV interneurons. **F**: Mean strength of excitatory synaptic inputs to layer II/III and IV interneurons arising from each cortical layer (data are mean ± SEM; *p<0.05).

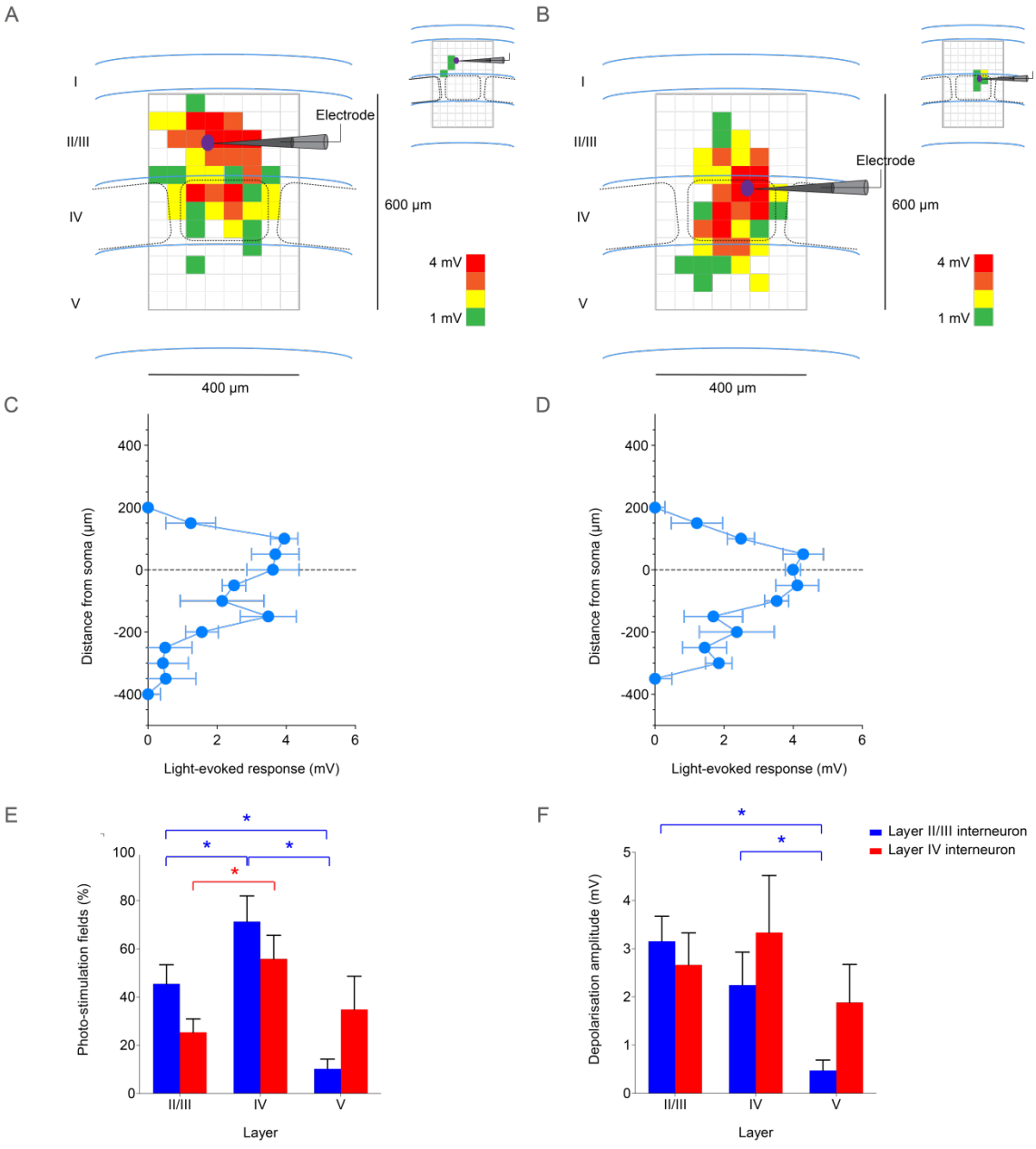
A
I
II/III
IV
V
Electrode
600 µm
4 mV
1 mV
400 µm
B
I
II/III
IV
V
Electrode
600 µm
4 mV
1 mV
400 µm
C
Distance from soma (µm)
400
200
0
-200
-400
0
2
4
6
Light-evoked response (mV)
D
Distance from soma (µm)
400
200
0
-200
-400
0
2
4
6
Light-evoked response (mV)
E
Photo-stimulation fields (%)
100
80
60
40
20
0
II/III
IV
V
Layer
F
Depolarisation amplitude (mV)
5
4
3
2
1
0
II/III
IV
V
Layer
Layer II/III interneuron
Layer IV interneuron

compared with 46% in layer II/III and only 10% in layer V (Figure 4.7E; n = 7). On average, the strength of synaptic inputs was significantly stronger for inputs arising from layer II/III and IV than inputs from layer V (Figure 4.7C,F; n = 7). Recordings from layer IV interneurons revealed the majority of excitatory inputs were received from neighbouring layer IV cells with significantly fewer fields in layer II/III generating responses (Figure 4.7B). Over 55% of photo-stimulation fields in layer IV demonstrated connectivity while only 25% and 35% generated responses in layers II/III and V respectively (Figure 4.7E; n = 6). Input strength was highest, but not statistically significant, for fields in layer IV and II/III, while inputs from layer V were typically weaker (Figure 4.7D,F). Application of glutamate receptor antagonists DNQX and AP5 abolished all light-evoked responses showing that they were presynaptic.

4.3.3 Photo-stimulation of long range projections

To assess the application of our projector-based photo-stimulation system for activation of long-range projections, thalamocortical tissue slices were prepared as described in the Methods (section 4.2.1). Recordings were made from pyramidal neurons in somatosensory cortex while targeting photo-stimulation to sites within the thalamic nuclei as well as somatosensory cortex (Figure 4.8A-C). Delivering photo-stimulation through a low magnification (5x) microscope objective permitted an illumination field spanning from the pia of the somatosensory cortex to the ventrobasal thalamic nuclei. Photo-stimulation was presented in a 500 µm diameter circular beam targeted over the upper region of the ventrobasal (VB) thalamic nuclei or the somatosensory barrel cortex. Illumination was presented in trains comprising 5 pulses with ~20 ms duration at

Figure 4.8: Photo-stimulation of ascending thalamocortical afferents

(**A**) Schematic of the thalamocortical slice preparation and photo-stimulation sites. (**B**) Reconstruction of a layer V pyramidal neuron showing location within somatosensory cortex. The blue spot indicates the photo-stimulation region. (**C**) Voltage response from cell in (**B**) in response to photo-stimulation (1.8 mW/mm^2) of the somatosensory cortex (upper traces) or ventrobasal thalamic nuclei (lower traces). Grey lines in lower traces indicate responses following application of synaptic blockers DNQX, AP5, and gabazine). **D**-**I**: Same as in (**A**-**C**) for layer II/III pyramidal (**D**-**F**) and IV neurons (**G**-**I**). **J**: Connection probability of thalamocortical input to neurons in layers V, II/III, and IV (% of total recorded cells demonstrating detectable thalamocortical light-evoked responses). **K**: Average amplitude of somatic depolarisations in neurons in layers V, II/III, and IV of the somatosensory cortex in response to thalamic photo-stimulation (data are mean ± SEM; n = 12, 8, and 9 for layer V, II/III, and IV respectively; $*p<0.05$).

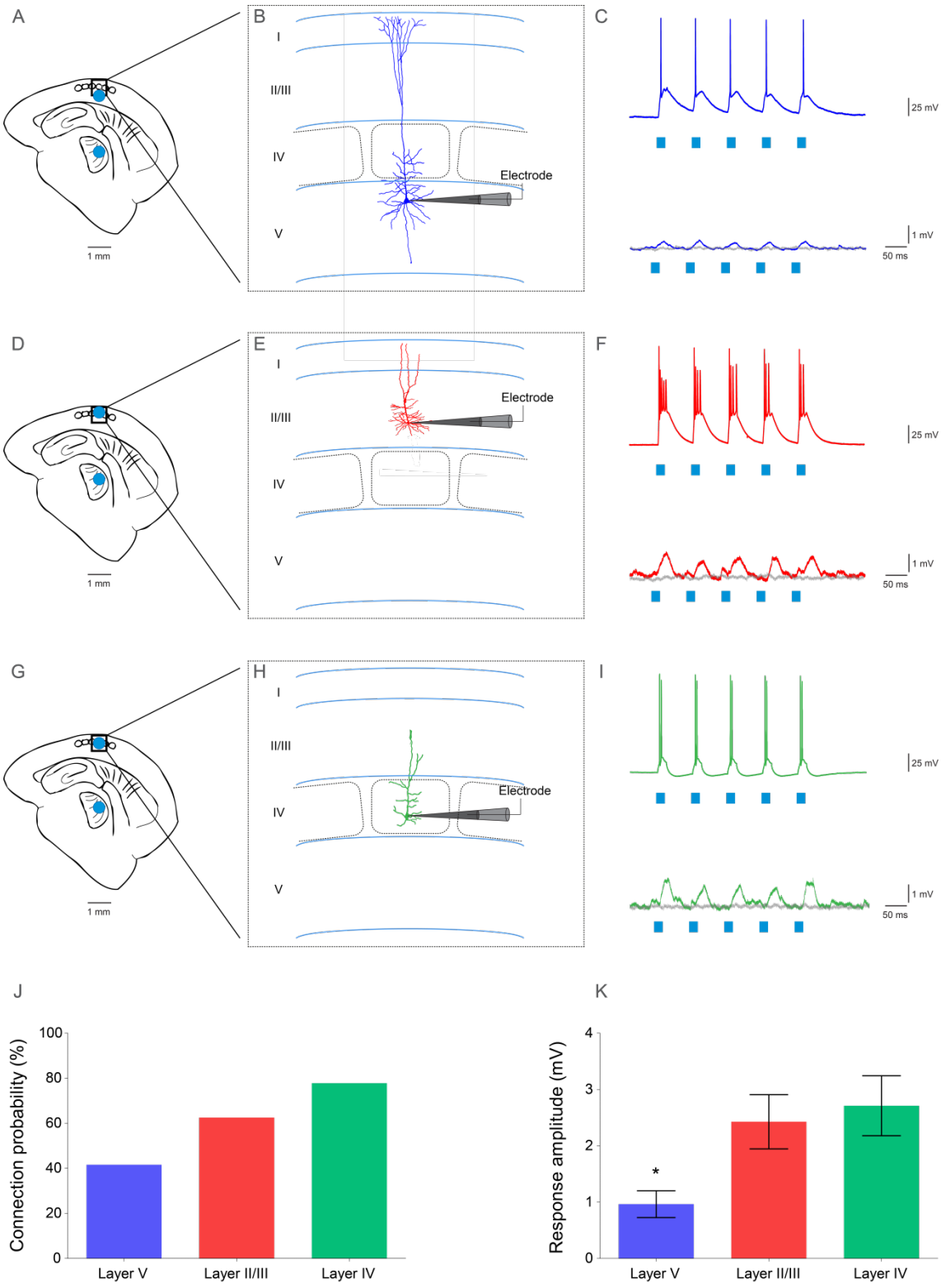
A
B
C
I
II/III
IV
V
Electrode
1 mm
25 mV
1 mV
50 ms
D
E
F
G
H
I
J
Connection probability (%)
100
80
60
40
20
0
Layer V
Layer II/III
Layer IV
K
Response amplitude (mV)
4
3
2
1
0
*

1.8 mW/mm^2. Whole-cell recordings were made from pyramidal neurons in layers II/III, IV, and V and somatic depolarisations measured in response to photo-stimulation. Direct photo-stimulation of the somatosensory cortex reliably elicited action potentials in all layer V pyramidal cells (n = 12; Figure 4.8A-C). Subsequent photo-stimulation to the VB thalamic nuclei evoked sub-threshold somatic depolarisations in 5 out of 12 layer V pyramidal neurons (Figure 4.8A-C and Figure 4.8J). In neurons demonstrating thalamocortical connectivity, somatic membrane depolarisation amplitudes were on average 0.96 ± 0.2 mV (Figure 4.8K; n = 5). Thalamocortical light-evoked responses were abolished following the application of synaptic blockers (10 µM DNQX; 50 µM AP-5; 10 µM gabazine) indicating they were synaptic.

Similar to that seen in layer V cells, layer II/III pyramidal cells demonstrated robust action potential firing in response to direct somatosensory photo-stimulation (results from cells determined to be ChR2-negative by application of synaptic blockers were discarded). Targeting photo-stimulation to the VB nuclei revealed thalamocortical inputs in 5 out of 8 cells, with an average somatic membrane depolarisation of 2.4 ±0.5 mV (Figure 4.8D-F,J,K). Somatic recordings from layer IV cells demonstrated thalamocortical connections in 7 out of 9 cells, with an average somatic amplitude of 2.7 ± 0.5 mV, demonstrating higher connectivity and input strength than seen in layer II/III and V neurons (Figure 4.8G-K).

4.4 Discussion

Innovations in genetic techniques (Asrican *et al.*, 2013), molecular engineering (Zhang *et al.*, 2011) and opsin targeting (Zhang *et al.*, 2009) have significantly expanded the capabilities of optogenetic methods. However, to appreciate the full potential of optogenetic manipulation, optical techniques need to allow for flexible and arbitrary generation of illumination patterns with high spatial, temporal, and ideally chromatic precision. The purpose of the research described in this chapter was to design a dynamic optical interface system capable of spatiotemporally precise optogenetic photo-stimulation. The central component of this illumination system is a modified LCD projector enabling projection of computer video output onto brain slice preparations. This method enables high spatial flexibility with illumination patterns that can be customized to meet the requirements of different experimental designs.

Three proof-of-principle studies were conducted to assess the application of this method. The first set of experiments was designed to assess the ability of projector-based illumination in investigating sub-cellular information processing in cortical pyramidal neurons. Rapid, precisely controlled photo-stimulation was targeted to progressively distal dendritic locations in layer V pyramidal neurons. The somatic amplitude of light-evoked depolarisations attenuated exponentially with increasingly distal input sites. Depolarisations generated from sites approximately 500 µm distal to the soma decreased by almost 6-fold (Figure 4.3). These data are consistent with other findings on the site-dependence of dendritic inputs on somatic EPSP amplitude (Williams and Stuart, 2003). Attenuation of pharmacologically isolated spontaneous EPSPs (Williams and

Stuart, 2003), however, is much greater than the attenuation of ChR2-generated events observed here. This likely reflects the different time course of these depolarisations with ChR2-generated conductance changes considerably slower than EPSPs. Simultaneously photo-stimulating multiple dendritic sites at different distances distal to the soma generated sub-linear spatial summation (Figure 4.3D). These results demonstrated the capacity of using controlled patterned photo-stimulation to examine dendritic signalling *in vitro*.

The second study comprised a series of experiments to map the spatial distribution of synaptic inputs onto cortical pyramidal neurons and interneurons in the mouse somatosensory barrel cortex. Synaptic connections between excitatory and inhibitory neurons within cortical circuits play a fundamental role in processing sensory information. The ability to quantitatively map this synaptic connectivity provides a means to understanding the organising principles governing neocortical circuits. Using a combination of whole-cell recordings from ChR2-negative neurons and projector-based photo-stimulation patterns, topographic 'heat' maps were constructed representing the spatial distribution of excitatory synaptic inputs onto pyramidal neurons and interneurons in layer II/III and IV of primary somatosensory barrel cortex. The photo-stimulation intensities used generated ChR2-evoked action potentials only during peri-somatic illumination (Figure 4.5), indicating that illumination fields represent the somatic location of presynaptic cells.

The findings from this aspect of the study indicate that layer II/III pyramidal cells receive the majority of their excitatory synaptic input from layer IV and II/III, with fewer inputs arising from layer V within the barrel column (Figure 4.6).

Excitatory inputs arising from layer IV and II/III were also significantly stronger than those in layer V. Interneurons in layer II/III also received extensive excitatory synaptic input from layer IV in addition to surrounding layer II/III cells (Figure 4.7). These data are consistent with the characteristic patterns of inputs and outputs in cortical columns of the barrel cortex where afferent signals arising from thalamic nuclei project primarily to cortical layer IV neurons, which in turn relay this input to the supra-granular layers II and III and subsequently to infra-granular layers V and VI. (Armstrong-James *et al.*, 1992; Petersen and Sakmann, 2001).

The vertical profile of excitatory synaptic input onto layer IV neurons revealed a relatively even distribution with strong inputs from within layer IV and layer V (Figure 4.6). Similar intra-columnar input profiles were also seen in interneurons residing in layer IV, where inputs were more numerous and stronger from local layer IV cells than inputs arising from layer V or layer II/III (Figure 4.7). An important consideration in these experiments is the complement of neuron subtypes in layer IV barrel cortex. Previous work (Staiger *et al.*, 2004) has characterised three subpopulations of excitatory cells in layer IV rat somatosensory barrel cortex, comprising spiny stellate cells (58%), star pyramidal cells (25%), and pyramidal cells (17%). The electrical properties of layer IV neurons in our study were consistent across cells (data not shown) prohibiting the capacity to distinguish between spiny stellate, star pyramidal and pyramidal cells based on their electrical properties alone. Morphological reconstructions were limited in these experiments and could not be used to identify cell types. Additionally, it is important to identify the nature of the postsynaptic potentials generated in these experiments. While our experiments

did not distinguish between mono-synaptic and poly-synaptic inputs as neurons in slices usually have a relatively negative membrane potential (see Table 3.1) we think it likely most of the inputs are mono-synaptic.

In conclusion, the study shows the capacity of our projector-based system to stimulate multiple fields providing an efficient method to map intra-cortical afferents in somatosensory cortex. Previous work using ChR2 photo-stimulation for circuit mapping (Wang *et al.*, 2007) has demonstrated the advantages this technique has over methods such as glutamate uncaging, where large direct responses can obscure local inputs (Wang *et al.*, 2007). Importantly, our method of photo-stimulation allows for simultaneous stimulation of different areas rather than relying on sequential scanning methods.

The final series of experiments utilised a thalamocortical slice preparation whereby projector-generated photo-stimulation patterns could be targeted to thalamic nuclei and somatosensory barrel cortex in the same experiment. These data revealed functional connectivity between the ventrobasal thalamus and somatosensory barrel cortex in all cortical layers (Figure 4.8). The significantly increased connection probability and input strength observed in layer IV pyramidal cells compared with inputs to layer II/III and V is consistent with the dense innervation of thalamocortical neurons in layer IV of barrel cortex (Bureau *et al.*, 2006; Aronoff *et al.*, 2010).

Together, these data provide proof-of-principle of the application of our projector-based photo-stimulation system for optogenetic studies. One clear advantage to this method is the ability to stimulate multiple regions in parallel

compared to traditional scanning techniques, which utilise serial photo-stimulation. The present chapter provides the first description of the application of this new system to study integration in single cells as well as circuit mapping both within the cortex and across brain regions.

CHAPTER FIVE

THE IMPACT OF DENDRITIC AND SOMATIC INHIBITION ON NEURONAL OUTPUT

5.1 Introduction

Neurons process information via the transformation of synaptic inputs into an output signal – the action potential. A wealth of theoretical and experimental studies has demonstrated that this process is governed by a multitude of non-linear mechanisms, greatly enhancing the computational power of single neurons (Blomfield, 1974; Silver, 2010). Pyramidal neurons in the cortex receive vast numbers of excitatory and inhibitory inputs. These inputs are not distributed uniformly across the dendritic tree but rather display distinctive organisation patterns. Excitatory inputs are concentrated on dendritic regions and are absent from the most proximal dendrites, soma, and axon initial segment – the peri-somatic region. In contrast, inhibitory inputs synapse throughout the dendritic tree and peri-somatic regions (Megias *et al.*, 2001; Spruston, 2008).

The ability to modulate action potential output in response to different complements of synaptic input is vitally important for information processing. This modulation of neuronal output is typically described in terms of gain control, where gain refers to the relationship between synaptic input and output firing rate. This enables a distinction between modulatory inputs which generate additive (or subtractive) changes in the input-output relationship, and those which produce multiplicative (or divisive) changes (Figure 5.1) (Silver, 2010). In

Figure 5.1: Neuronal input-output relationships in response to modulatory input

Schematic of the input-output relationship between the driving input and the output firing rate of a neuron. The black line represents a hypothetical plot of the firing rate of a neuron as a function of input intensity. Modulatory inputs can increase excitation by shifting the curve to the left (green), while purely subtractive inhibition shifts the curve to the right (red). Changes in gain are represented as a change in the slope of the curve (blue). An increase in rheobase (minimum input that generates an action potential) and reductions in slope indicates subtractive and divisive effects, respectively.

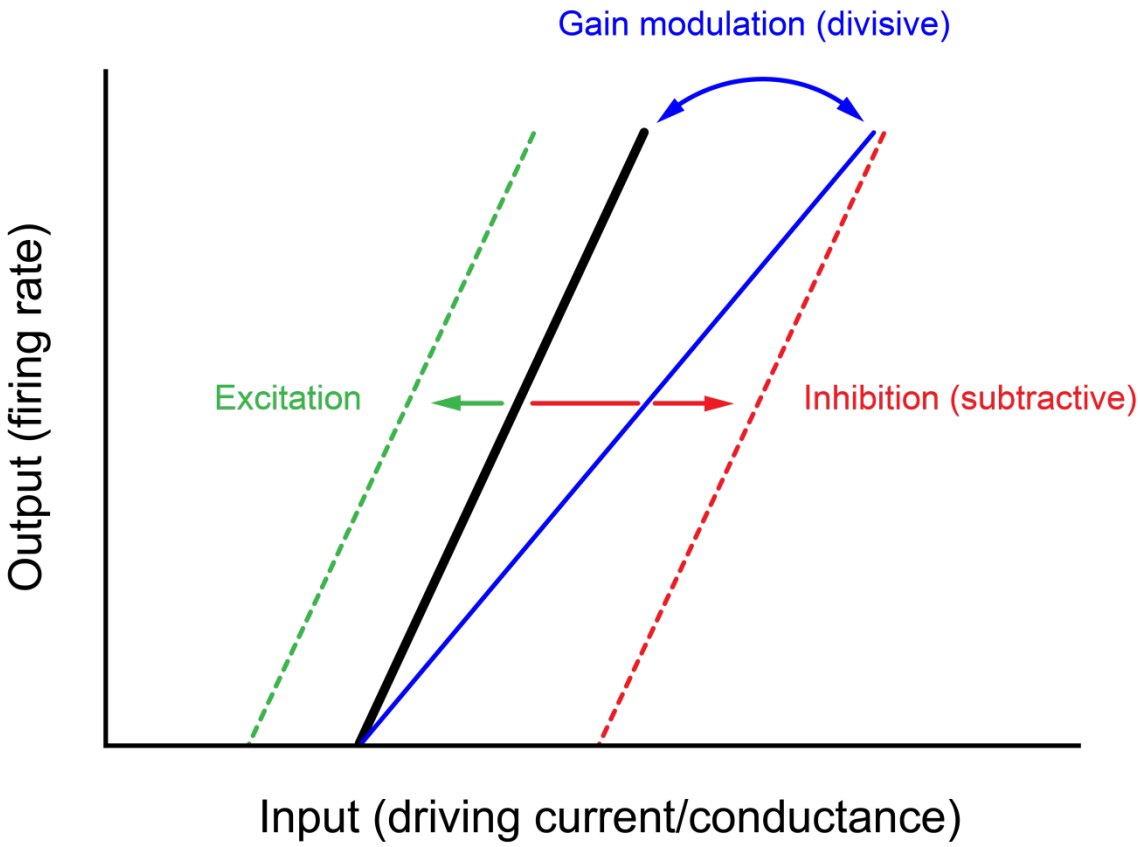
Gain modulation (divisive)
Excitation
Inhibition (subtractive)
Output (firing rate)
Input (driving current/conductance)

the case of inhibitory input, GABA-mediated inhibition acts by increasing membrane potential hyperpolarisation and/or increasing membrane conductance. Membrane hyperpolarisation produces a subtractive effect on excitatory input – observed as a uniform right-shift in the input-output relationship. This acts to sharpen neuronal responses by filtering inputs based on relative strength. In contrast, increased membrane conductance (shunting inhibition) creates a divisive effect – observed as a change in the slope of the input-output curve. This serves to scale excitatory synaptic inputs (Blomfield, 1974; Prescott and De Koninck, 2003; Ulrich, 2003; Silver, 2010). Although gain control through inhibition is a well-established feature of many neuronal circuits, the underlying mechanisms remain poorly understood.

Inhibitory interneurons in the neocortex exhibit extraordinary diversity in their morphology, electrophysiology, molecular composition, and connectivity patterns (Markram *et al.*, 2004; DeFelipe *et al.*, 2013). Despite this diversity, cortical interneurons can be broadly classified into three groups based on the molecular markers they express; namely, the calcium-binding protein parvalbumin, the neuropeptide somatostatin, and the ionotropic serotonin receptor 5HT3a (this group includes neurons expressing the neuropeptide VIP) (Rudy *et al.*, 2011). The two most abundant of these groups – the parvalbumin-expressing (PV) interneurons and somatostatin-expressing (SOM) interneurons – exhibit distinct synaptic connectivity patterns. PV interneurons characteristically target inhibition to the somatic region of pyramidal neurons, whereas SOM interneurons target inhibition to the dendrites of pyramidal cells (Markram *et al.*, 2004; Freund and Katona, 2007; Silberberg and Markram,

2007). These characteristic properties of PV and SOM interneurons suggest that they may perform distinct computational functions within cortical circuits.

Recent studies have begun to explore the impact of dendritic versus somatic inhibition on the output of cortical pyramidal neurons by studying the influence of PV and SOM interneuron-mediated inhibition in the mouse visual cortex *in vivo* (Atallah *et al.*, 2012; Lee *et al.*, 2012; Wilson *et al.*, 2012). These studies have used optogenetics to activate and inactivate PV and SOM cells. Interestingly, two of these studies reached opposing conclusions regarding the impact of PV and SOM interneuron-mediated inhibition on the input-output relationship in cortical pyramidal cells (Lee *et al.*, 2012; Wilson *et al.*, 2012). Subsequently, these findings were revisited (Lee *et al.*, 2014) suggesting that the different conclusions from these studies may be attributed to differences in the anaesthetics and optogenetic stimulation paradigms used. These results highlight the complexity of looking at this issue *in vivo* and reveal that further work is needed to fully understand the impact of somatic versus dendritic inhibition on neuronal output.

The present study was undertaken to investigate how inhibition targeted to somatic or dendritic regions of cortical layer V pyramidal neurons in mouse somatosensory cortex impacts on input-output relationships *in vitro*. Optogenetic stimulation and pharmacological inhibition are used to create somatic and dendritic excitatory and inhibitory input, allowing their impact on neuronal output to be investigated. In addition, we investigate how the location of excitatory input influences this process.

5.2 Methods

5.2.1 Tissue preparation and electrophysiology

Coronal brain tissue slices were prepared from ChR2-YFP mice as described in the General Methods (section 2.2). Primary somatosensory cortex was identified as described previously (section 3.2.1) and whole-cell patch-clamp recordings were made from the somata of visually identified pyramidal neurons in layer V. Electrophysiological properties were determined from voltage responses to somatic current injection and intracellular solution containing biocytin allowed for morphological identification of recorded neurons as described in the General Methods (section 2.5).

Input-output curves were generated by driving neurons with somatic depolarising current, or somatic or dendritic photo-stimulation of ChR2 (see section 5.2.2, below) and neuronal output (AP firing frequency) measured as a function of stimulus input. For somatic current injection this was defined by f-I curves (frequency of action potential output versus current (I) amplitude) and was achieved by injection of a series of 1-second-long depolarising current steps with amplitudes up to 1.2 nA increasing in 50 pA increments. Action potential output was averaged across 5 trials for each cell. Rheobase for input-output curves was defined as the lowest current amplitude or photo-stimulation intensity (see section 5.2.2 below) to elicit action potentials. Slope for input-output curves was calculated as *m* (where $m = \frac{y2 - y1}{x2 - x1}$) over a range of 5 points at 50% maximal response. The impact of somatic or dendritic inhibition on

input-output relationships was determined from the change in rheobase and slope of input-output functions.

5.2.2 Photo-stimulation

For photo-stimulation of ChR2-expressing cells, a projector-based illumination system was used to generate patterns of light with software controlled spatial and temporal characteristics as described in Chapter Four (section 4.2.2). Photo-stimulation patterns were constructed to deliver illumination to either the somatic or apical and basal dendritic region of target neurons (Figure 5.2).

To generate input-output curves, photo-stimulation was presented for 1 second with increasing intensity from 31.2 to 100% maximum light intensity (8.8 mW/mm^2) in 1.6% increments. Input-output functions were defined as f-L curves (frequency of action potential output versus light (L) intensity).

5.2.3 Pharmacology

To isolate direct ChR2 responses most experiments were performed in the presence of cadmium chloride ($CdCl_2$; 100 µM). To generate spatially restricted inhibition γ-aminobutyric acid (GABA; 100 µM) was locally applied via a patch pipette either to the somatic region (~30 µm from the soma) or to the main apical dendrites (~250 µm from the soma towards the pia) using pressure (10-20 PSI). In experiments where inhibitory synaptic transmission was blocked locally at the soma, gabazine (10 µM) was locally applied via a patch pipette to

Figure 5.2: Different methods used to stimulate layer V pyramidal cells

Schematic of the different stimulation and recording arrangements. Left: Stimulation and recording via the somatic current injection. Middle: and Right: Somatic recording during photo-stimulation restricted to somatic (middle) or dendritic regions using a light doughnut (right) used to excite the soma and proximal dendrites, respectively, of layer V pyramidal neurons.

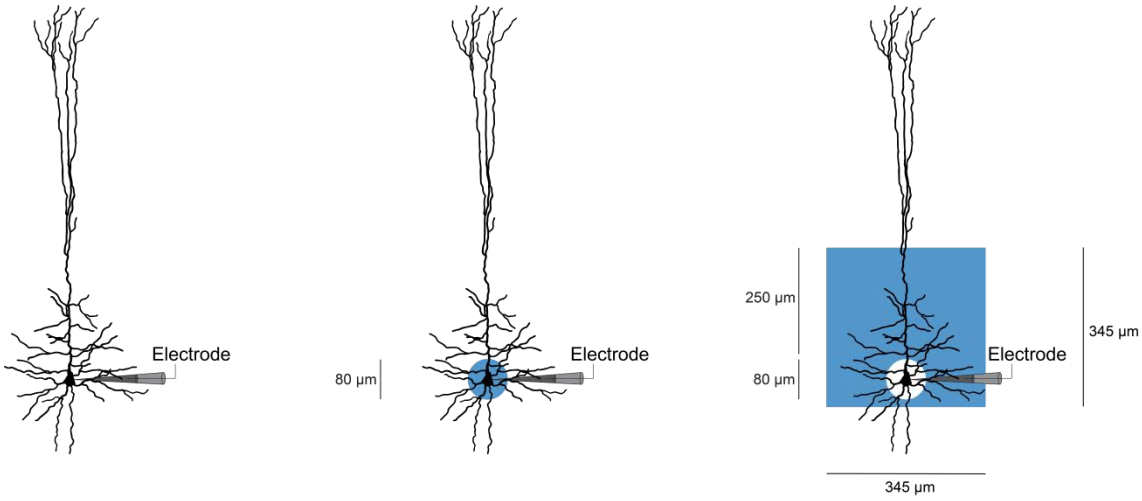
Electrode
80 µm
Electrode
250 µm
80 µm
345 µm
Electrode
345 µm

the somatic region (~ 30 µm from the soma). Excitatory synaptic transmission was blocked globally in these experiments using bath application of the glutamate receptor antagonists DNQX and AP5 (10 µM and 50 µM, respectively).

5.3 Results

5.3.1 Excitatory somatic and dendritic input-output relationships

To investigate the impact of inhibition on input-output relationships whole-cell patch-clamp recordings were made from layer V pyramidal neurons in mouse primary somatosensory cortex. Initially, somatic current injection was used to excite neurons using current steps of increasing amplitude (see methods section 5.2.1) and input-output relationships determined as frequency-current (f-I) functions. To determine whether photo-stimulation of ChR2 could be used to reliably generate similar input-output relationships, photo-stimulation was targeted to either the soma or apical dendritic regions (see Figure 5.3A) to evoke postsynaptic responses in layer V pyramidal cells. Frequency-light intensity (f-L) input-output functions were then generated by increasing the photo-stimulation intensity. These responses were due to direct ChR2 activation as synaptic transmission was blocked with glutamate receptor antagonists DNQX and AP5. $GABA_A$ receptors were also blocked in these experiments by bath application of the antagonist gabazine. To aid comparison of relative changes between somatic and dendritic photo-stimulation, f-L curves during somatic photo-stimulation were matched to those observed during somatic current injection (Figure 5.3B). This was achieved by aligning the rheobase and matching the maximum firing frequency during somatic photo-stimulation with that observed during somatic current injection. As a result the slope of the input-output relationship during somatic current injection was not significantly different from that during somatic ChR2 photo-stimulation (Figure 5.3B,C; n = 8; $P < 0.05$). The input-output slope was also not significantly different during somatic

Figure 5.3: Comparison of input-output functions during somatic current injection with somatic and dendritic ChR2 photo-stimulation

A: Schematic of the different recording and stimulation arrangements. **B**: Input-output functions for somatic current injection (red), somatic photo-stimulation (dark blue), and dendritic photo-stimulation (light blue). The light-intensity scale was adjusted to match rheobase and maximum firing frequency for somatic photo-stimulation and somatic current injection. **C**: The slope of input-output functions during somatic current injection (red) versus somatic light stimulation (dark blue; upper panel) and dendritic light stimulation (light blue; lower panel). Data are mean ± SEM; n = 8; *p<0.05.

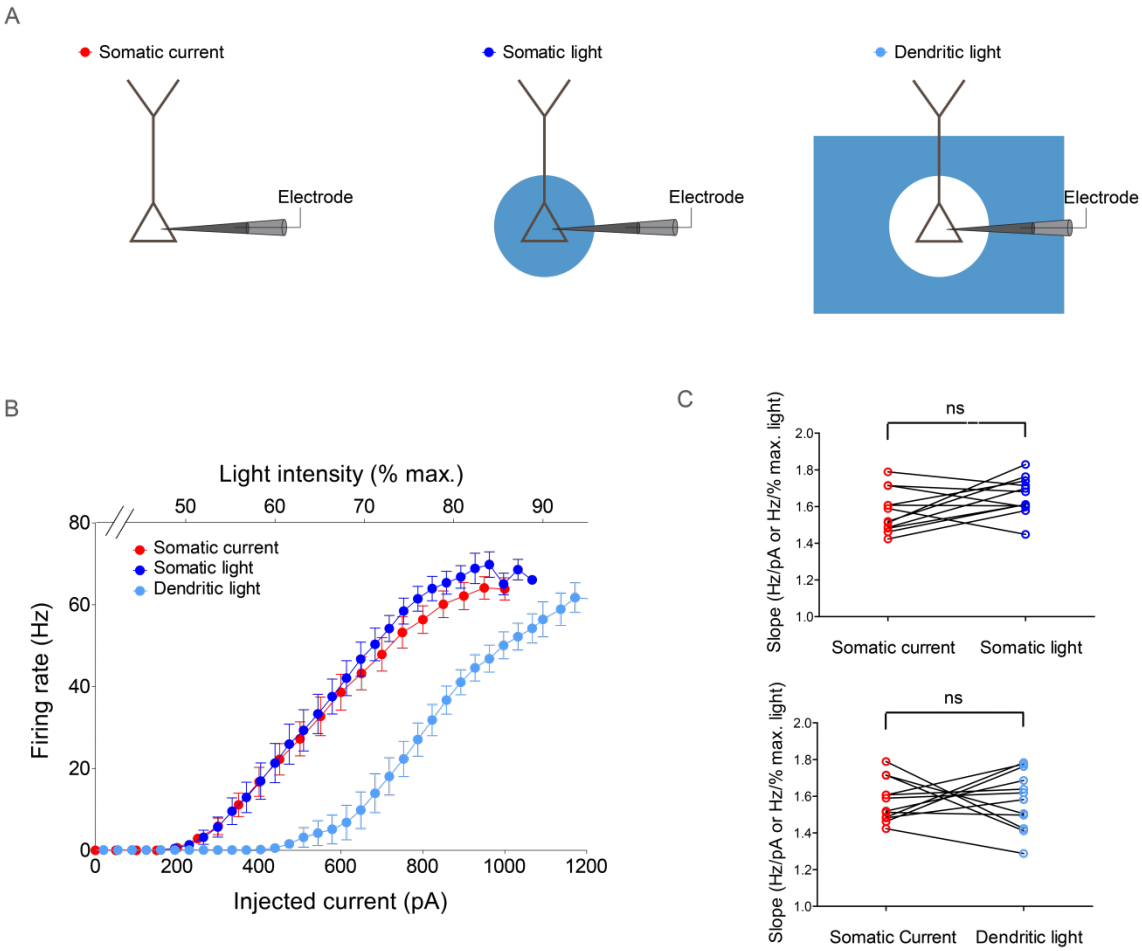
A
Somatic current
Somatic light
Dendritic light
Electrode
Electrode
Electrode
B
Light intensity (% max.)
50
60
70
80
90
Somatic current
Somatic light
Dendritic light
Firing rate (Hz)
0
20
40
60
80
0
200
400
600
800
1000
1200
Injected current (pA)
C
ns
Slope (Hz/pA or Hz/% max. light)
2.0
1.8
1.6
1.4
1.2
1.0
Somatic current
Somatic light
ns
Slope (Hz/pA or Hz/% max. light)
2.0
1.8
1.6
1.4
1.2
1.0
Somatic Current
Dendritic light

photo-stimulation compared to dendritic photo-stimulation (Figure 5.3B,C; n = 8; $P \geq 0.05$). Measurements of rheobase under these conditions show that dendritic photo-stimulation lead to a rightward shift in the f-L curve with firing frequency saturating at higher light intensities than observed during somatic photo-stimulation (Figure 5.3B).

These data show that photo-stimulation restricted to somatic or dendritic regions of ChR2-expressing layer V pyramidal neurons can be used to generate input-output relationships during somatic and dendritic excitation. Importantly, this method of generating excitation closely matches that which occurs during synaptic input in that it can be distributed over a large area of the dendritic tree and is generated by a conductance change. While dynamic clamp has been used to mimic dendritic synaptic input in previous studies (Williams, 2004; Pouille *et al.*, 2013), dynamic clamp only generates a conductance change at the site of the recording pipette, so is highly localised. Generating excitatory input with our projector-based system (see Methods section 5.2.2) also allows the capacity to simultaneously target multiple cellular regions.

5.3.2 Impact of somatic and dendritic inhibition on neuronal output

To investigate the impact of somatic versus dendritic inhibition on pyramidal cell output, GABA was locally applied to either the soma or the apical dendrites. Cadmium chloride (100 µM) was added to the bath to block presynaptic calcium channels, blocking transmitter release and thereby restricting the impact of GABA to the region of the postsynaptic cell close to the application site.

We first investigated the impact of somatic and dendritic GABA applications on action potential output in response to somatic photo-stimulation (Figure 5.4A-D). Photo-stimulation was achieved by targeting a projector-based illumination 'spot' to the soma of layer V pyramidal cells (see Figure 5.2). During somatic photo-stimulation, both somatic and dendritic GABA applications lead to a significant suppression of action potential firing compared to control (Figure 5.4E). Rheobase was significantly higher than controls (50.4 ± 1.48% max. light) during both somatic (Figure 5.4F, top left; 76.2 ± 1.61% max. light; n = 8; $P < 0.05$) and dendritic GABA application (Figure 5.4F, top right; 62.7 ± 0.92% max. light; n = 9; $P < 0.05$). The slope of the f-L relationship was not statistically different from control (1.46 ± 0.085) during either somatic (Figure 5.4F, bottom left; 1.37 ± 0.11; n = 8; $P > 0.05$) or dendritic GABA application (Figure 5.4F, bottom right; 1.43 ± 0.07; n = 9; $P < 0.05$).

.

To examine how somatic and dendritic inhibition shapes neuronal input-output relationships when neurons are driven by dendritic excitatory input, projector-based illumination patterns were targeted to the dendrites of layer V pyramidal cells (see Figure 5.2). A light 'doughnut' was used to evoke postsynaptic responses in the proximal dendrites of layer V pyramidal cells – avoiding the somata. Experiments were performed in the presence of cadmium chloride to block synaptic transmission, isolating direct responses due to activation of ChR2 in the postsynaptic cell. GABA was then puffed locally at either the soma or dendrites (see methods section 5.2) while measuring action potential output to dendritic photo-stimulation (Figure 5.5A-D).

Figure 5.4: Impact of somatic and dendritic inhibition on input-output functions during somatic ChR2 photo-stimulation

A and **B**: Schematic of recording and stimulation arrangement during somatic (left) and dendritic (right) inhibition. The blue circles indicate the area of photo-stimulation. **C** and **D**: Example responses illustrating suppression of action potential firing during somatic and dendritic GABA application for the photo-stimulation intensity indicated by the dashed line in **E**. **E**: F-L curves during somatic photo-stimulation in control (blue) and after GABA application to the soma (red) and dendrites (green). **F**: Rheobase (upper panel) and f-L slope (lower panel) in control (blue) and after somatic (red; left panels) or dendritic GABA application (green; right panels). Data are mean ± SEM; n = 8 (somatic GABA) and 9 (dendritic GABA); $*p<0.05$.

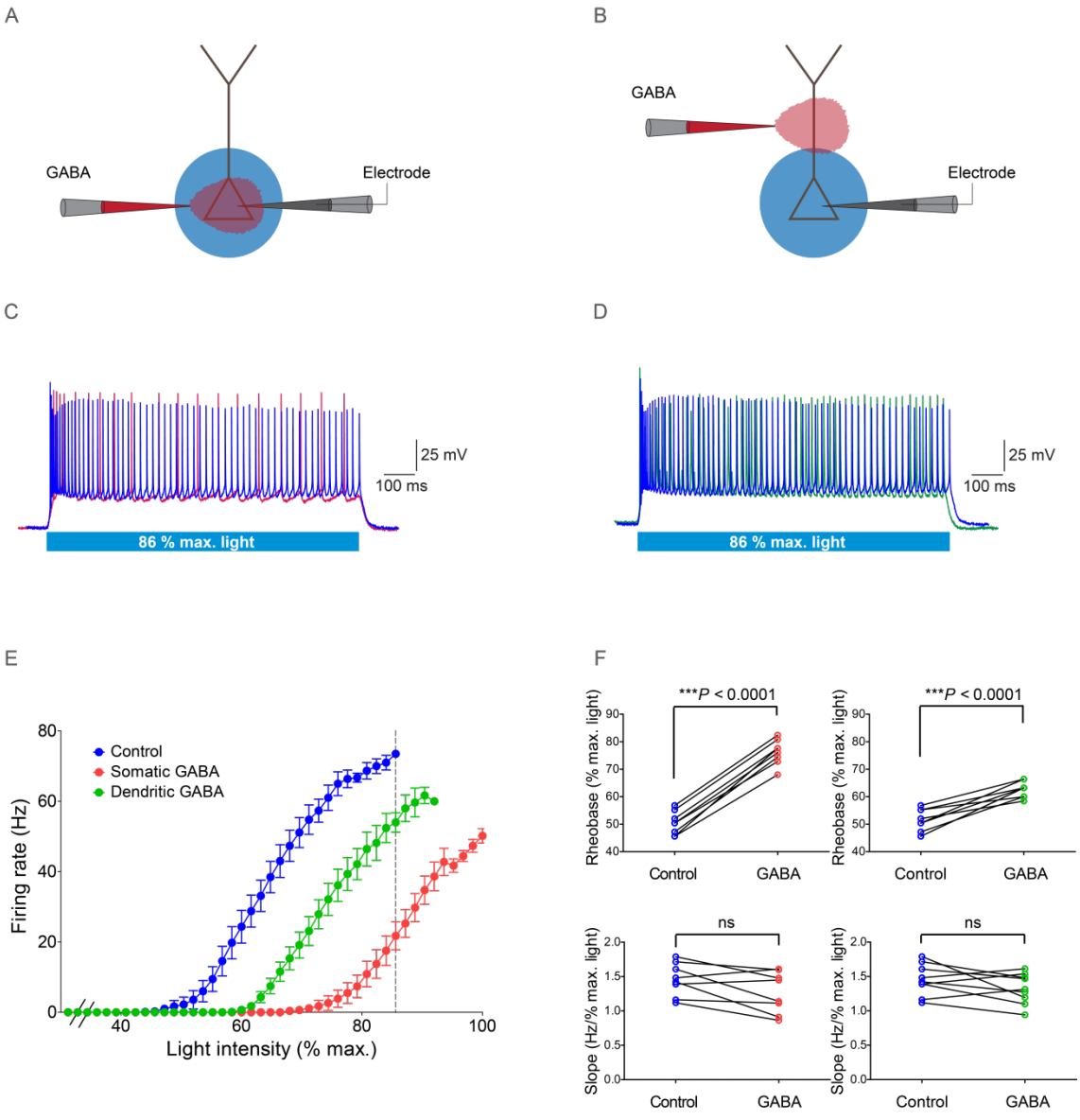
A
GABA
Electrode
B
GABA
Electrode
C
25 mV
100 ms
86 % max. light
D
25 mV
100 ms
86 % max. light
E
Control
Somatic GABA
Dendritic GABA
Firing rate (Hz)
Light intensity (% max.)
F
***P < 0.0001
Rheobase (% max. light)
Control
GABA
***P < 0.0001
Rheobase (% max. light)
Control
GABA
ns
Slope (Hz/% max. light)
Control
GABA
ns
Slope (Hz/% max. light)
Control
GABA

Figure 5.5: Impact of somatic and dendritic inhibition on input-output functions during dendritic ChR2 photo-stimulation

A and **B**: Schematic of recording and stimulation arrangement during somatic (left) and dendritic (right) inhibition. The blue rectangle with a hole at the soma represents the region of photo-stimulation. **C** and **D**: Example responses illustrating suppression of action potential firing during somatic and dendritic GABA application for the photo-stimulation intensity indicated by the dashed line in **E**. **E**: F-L curves during dendritic photo-stimulation in control (blue) and after GABA application to the soma (red) and dendrites (green). **F**: Rheobase (upper panels) and f-L slope (lower panels) in control (blue) and after somatic (red; left panels) or dendritic GABA application (green; right panels). Data are mean ± SEM; n = 8 (somatic GABA) and 9 (dendritic GABA); $*p<0.05$.

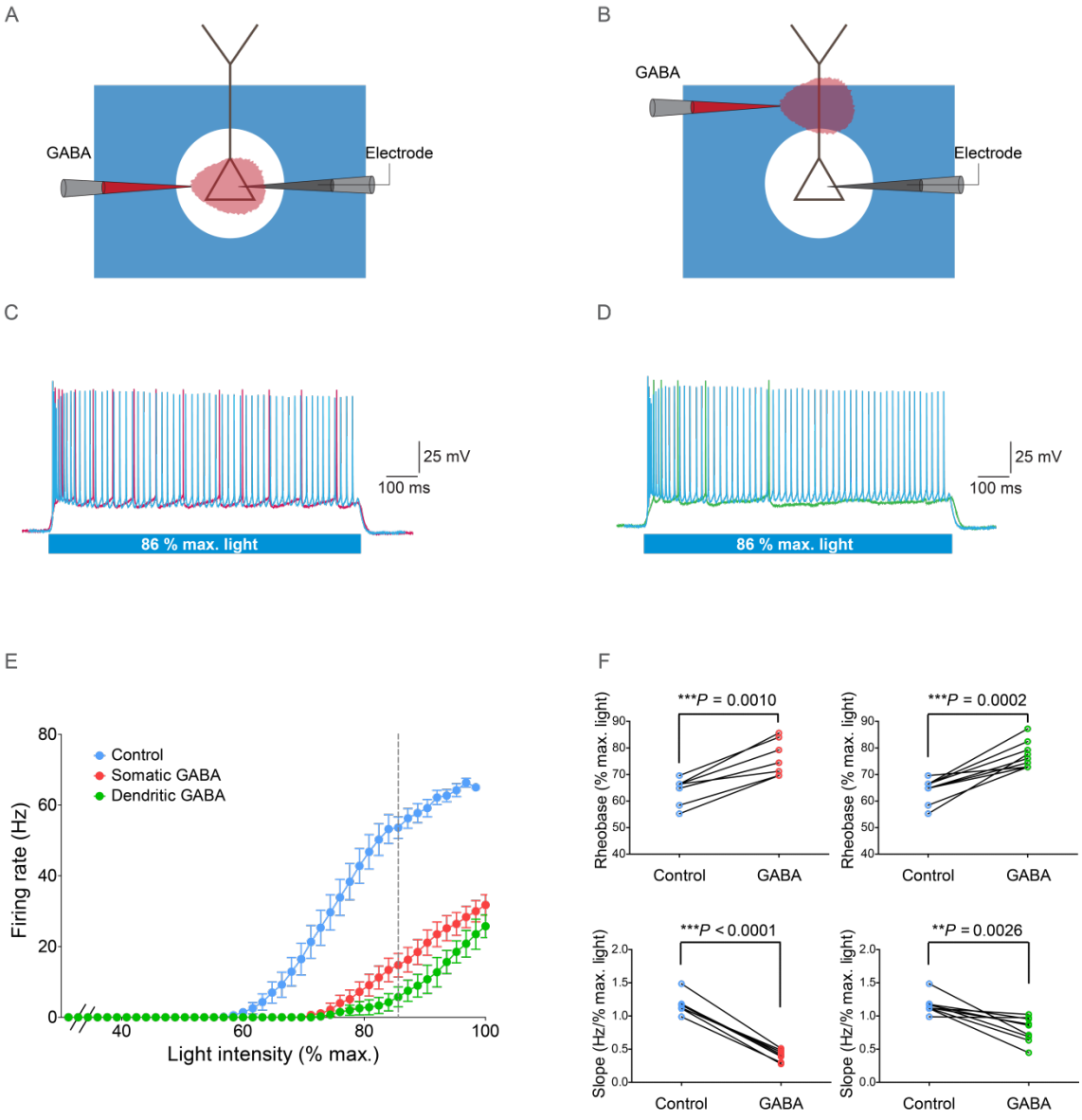
A
GABA
Electrode
B
GABA
Electrode
C
25 mV
100 ms
86 % max. light
D
25 mV
100 ms
86 % max. light
E
Control
Somatic GABA
Dendritic GABA
Firing rate (Hz)
Light intensity (% max.)
F
***P = 0.0010
Rheobase (% max. light)
Control
GABA
***P = 0.0002
Rheobase (% max. light)
Control
GABA
***P < 0.0001
Slope (Hz/% max. light)
Control
GABA
**P = 0.0026
Slope (Hz/% max. light)
Control
GABA

During dendritic photo-stimulation, both somatic and dendritic GABA application resulted in suppression of action potential firing relative to control (Figure 5.5E). Rheobase was significantly higher than control (64 ± 1.68% max. light) during somatic (Figure 5.5, top left; 76 ± 1.33% max. light; n = 8; $P < 0.05$) and dendritic GABA application (Figure 5.5F, top right; 77.4 ± 1.88% max. light; n = 9; $P < 0.05$). Additionally, the slope of the f-L function was significantly reduced relative to control (1.17 ± 0.05) during both somatic (Figure 5.5F, lower left; 0.41 ± 0.03; n = 8; $P < 0.05$) and dendritic GABA application (Figure 5.5F, lower right; 0.8 ± 0.063; n = 9; $P < 0.05$).

5.3.3 Impact of network-driven dendritic inhibition on neuronal output

The final set of experiments in this series investigated how network-driven dendritic synaptic inhibition shapes input-output relationships (Figure 5.6). Projector-based photo-stimulation patterns were used to recruit ChR2-expressing inhibitory interneurons in layer V of somatosensory cortex (see Chapter three). Recordings were made in the absence of cadmium chloride but with excitatory synaptic transmission blocked using glutamate receptor antagonists DNQX and AP5. The $GABA_A$ receptor antagonist gabazine was then locally applied at the soma to block somatic inhibitory input, thereby restricting inhibition to dendritic regions of the target cell. Action potential output was recorded in response to dendritic photo-stimulation at different intensities during local somatic gabazine applications, with the control input-output relationships obtained following bath application of gabazine or cadmium chloride.

Figure 5.6: Impact of dendritic network inhibition on input-output functions during dendritic ChR2 photo-stimulation

A: Schematic of recording and stimulation arrangement during dendritic excitation and network inhibition. The blue rectangle with a hole at the soma represents the region of photo-stimulation. **B**: Example responses illustrating suppression of action potential firing during dendritic network inhibition for the photo-stimulation intensity indicated by the dashed line in **C**. **C**: F-L curves during dendritic photo-stimulation in control (blue) and after dendritic network inhibition (green). **D**: Rheobase (left panel) and f-L slope (right panel) in control (blue) and after dendritic network inhibition (green). Data are mean ± SEM; n = 7; *p<0.05.

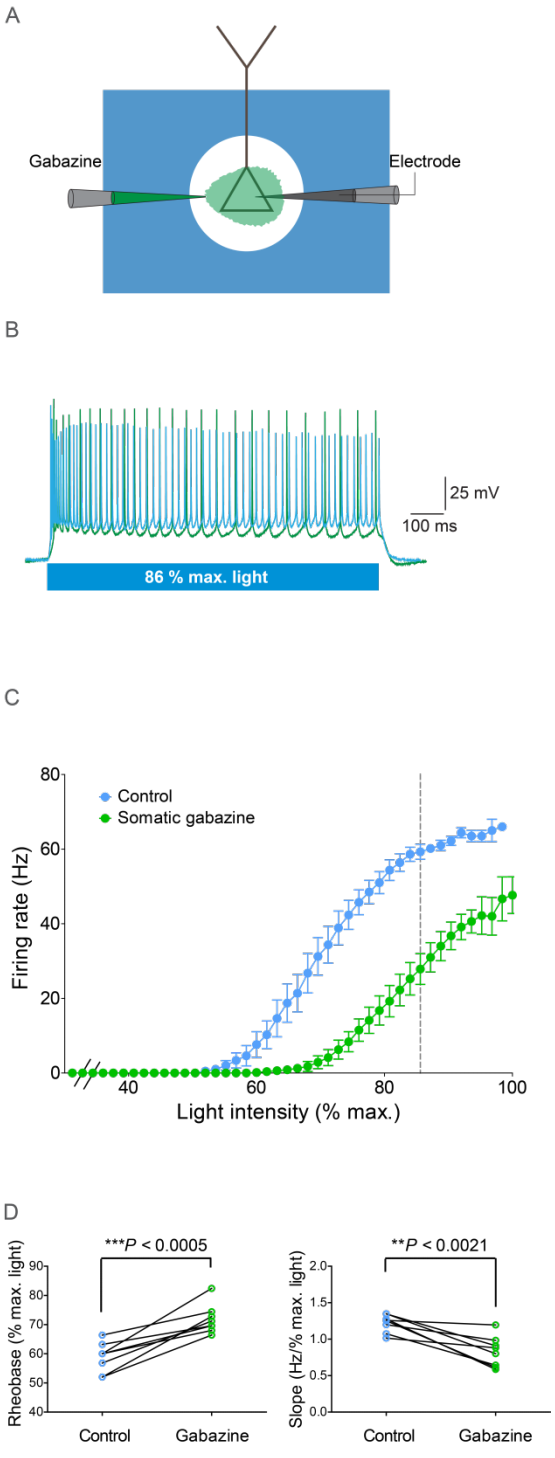
A
Gabazine
Electrode
B
25 mV
100 ms
86 % max. light
C
Control
Somatic gabazine
Firing rate (Hz)
Light intensity (% max.)
D
***P < 0.0005
Rheobase (% max. light)
Control
Gabazine
**P < 0.0021
Slope (Hz/% max. light)
Control
Gabazine

Recruitment of dendritic synaptic inhibition by photo-stimulation resulted in suppression of action potential firing relative to control (Figure 5.6A, B). Rheobase was significantly higher than control (45.4 ± 1.14% max. light) during network-driven dendritic inhibition (Figure 5.6D, left; 54.5 ± 1.71% max. light; n = 7; $P < 0.05$). Additionally, the slope of the f-L function was significantly reduced relative to control (1.52 ± 0.05) by network-driven dendritic inhibition (Figure 5.6D, right; 0.35 ± 0.03; n = 7; $P < 0.05$). While it was not possible to examine the impact of network-driven somatic inhibition in these experiments, these data demonstrate that dendritic inhibition driven by synaptic input influences input-output relationships in a similar manner to that seen during local activation of dendritic GABA receptors (see Figure 5.5).

During somatic photo-stimulation, suppression of action potential firing was significantly greater during somatic GABA compared to dendritic GABA applications. Rheobase was increased more by somatic compared to dendritic GABA applications (Figure 5.7B; n = 9; $P < 0.05$), but neither had a significant impact on the slope of f-L curves (Figure 5.7C, right; n = 9; $P \geq 0.05$). These data show that when pyramidal neurons are driven by somatic excitation somatic inhibition leads to a greater shift of the f-L function to the right than dendritic inhibition, due to a greater impact on rheobase.

During dendritic photo-stimulation, suppression of action potential firing was also greater during somatic compared to dendritic GABA applications. While the impact of somatic compared to dendritic GABA applications on rheobase was not statistically different (Figure 5.7B, right; n = 9; $P = 0.6375$), the slope of the f-L function was reduced significantly more during somatic GABA applications

Figure 5.7: Comparison of somatic and dendritic inhibition on input-output functions during either somatic or dendritic ChR2 photo-stimulation

A: Schematic of recording and stimulation arrangement. The blue circle (left) and rectangle with hole at the soma (right) indicate the area of photo-stimulation. **B:** Percentage change in rheobase after somatic (red) and dendritic GABA application (green) during somatic (left) and dendritic (right) photo-stimulation. **C:** F-L slope after somatic (red) and dendritic GABA application (green) during somatic (left) and dendritic (right) photo-stimulation. Circles represent individual data points, columns indicate mean ± SEM. **D:** Blue columns represent percentage change in rheobase during somatic and dendritic GABA applications. Red columns represent percentage change in f-L slope during somatic and dendritic GABA applications. Somatic and dendritic light denotes the site of ChR2 photo-stimulation. Data are mean ± SEM; n = 8 (somatic GABA) and 9 (dendritic GABA). Datasets were compared to 1 for statistical significance; *p<0.05.

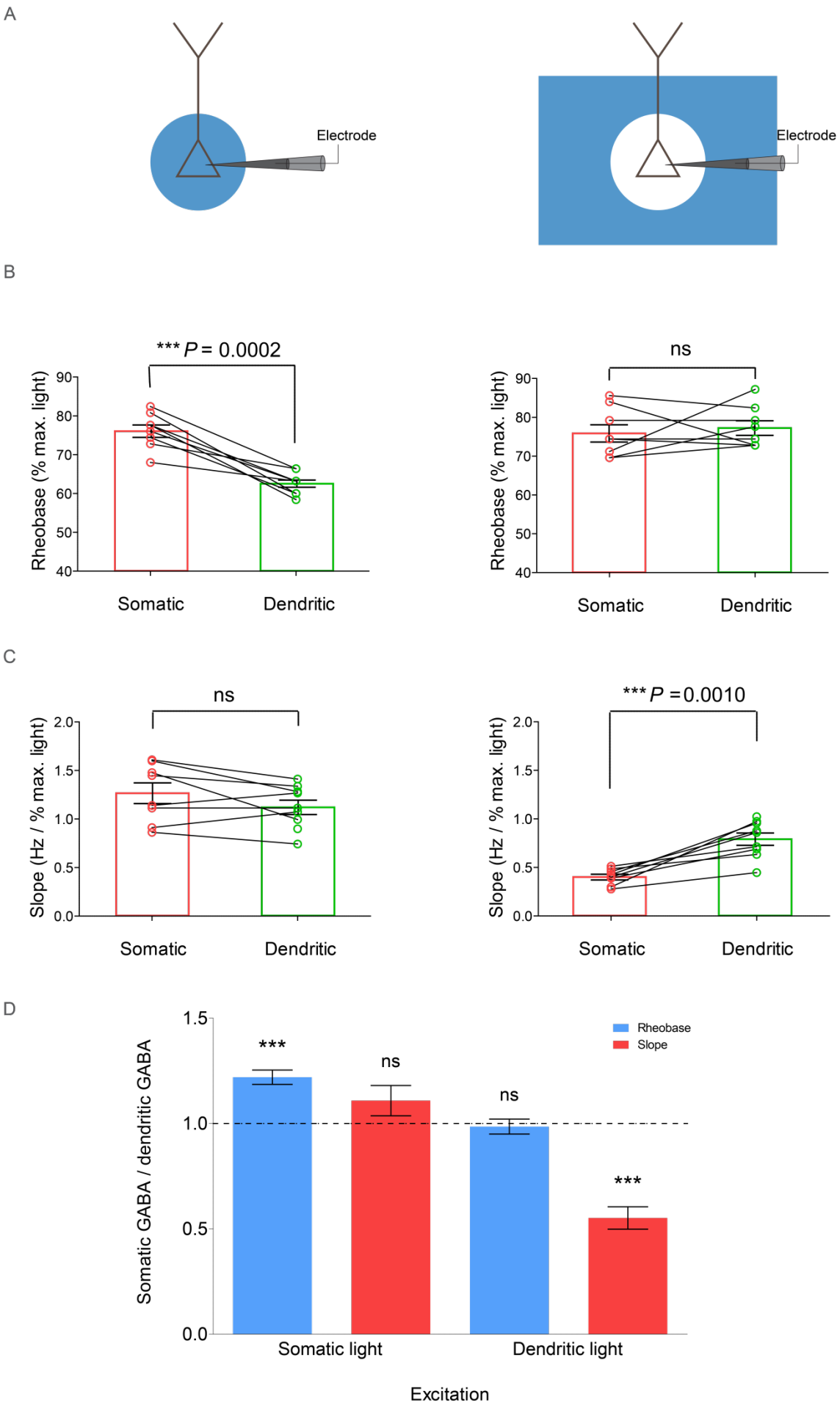
A
Electrode
Electrode
B
*** P = 0.0002
ns
Rheobase (% max. light)
90
80
70
60
50
40
Somatic
Dendritic
Rheobase (% max. light)
90
80
70
60
50
40
Somatic
Dendritic
C
ns
Slope (Hz / % max. light)
2.0
1.5
1.0
0.5
0.0
Somatic
Dendritic
*** P = 0.0010
Slope (Hz / % max. light)
2.0
1.5
1.0
0.5
0.0
Somatic
Dendritic
D
Rheobase
Slope
Somatic GABA / dendritic GABA
1.5
1.0
0.5
0.0
***
ns
ns
***
Somatic light
Dendritic light
Excitation

(Figure 5.7C, right; n = 9; $P < 0.05$). These data show that when pyramidal neurons are driven by dendritic excitatory input, activation of somatic inhibition causes a greater reduction in slope of the f-L curve than dendritic inhibition. Comparing the percentage change between somatic and dendritic inhibition under conditions of either somatic or dendritic excitatory input demonstrates that somatic inhibition produces significantly more subtractive effects when excitation is driven somatically, while generating more divisive effects during dendritic excitatory input (Figure 5.7D).

5.4 Discussion

Individual neurons employ a range of non-linear mechanisms in transforming synaptic input into firing output (Silver, 2010). By generating input-output relationships between the driving input and the output firing rate it is possible to investigate the impact of modulatory inhibitory input on neuronal gain control. Changes in the offset and slope of the input-output curve permit a distinction between modulatory inputs that generate additive (or subtractive) changes and those that produce multiplicative (or divisive) changes. During inhibition, subtractive effects lead to a right-shift in the input-output relationship, whereas divisive effects reduce the slope of the input-output relationship (Blomfield, 1974; Silver, 2010).

The thousands of excitatory and inhibitory synaptic inputs pyramidal neurons receive are not distributed evenly across the dendritic tree. Excitatory inputs synapse onto dendritic regions and are absent from the most proximal dendrites, soma, and axon initial segment, while inhibitory inputs synapse across the dendritic tree and peri-somatic regions (Megias *et al.*, 2001; Spruston, 2008). This provides an environment where in dendrites inhibitory inputs are interspersed with excitatory driving inputs, whereas the peri-somatic regions receive inhibition alone. These observations have been postulated to underpin different qualities of inhibition, with peri-somatic inhibitory inputs believed to provide gating inhibition and dendritic inputs generating gain control (Trevelyan and Watkinson, 2005). Indeed, this view is supported by observations that distinct populations of interneurons target somatic and dendritic regions (Markram *et al.*, 2004; Freund and Katona, 2007; Silberberg

and Markram, 2007). Recently, the contribution of synaptic location on gain control has been investigated during activation of different classes of interneurons *in vivo* drawing very different conclusions (Atallah *et al.*, 2012; Lee *et al.*, 2012; Wilson *et al.*, 2012). The present study was undertaken to address this issue *in vitro*, determining how inhibition targeting the somatic versus dendritic compartments shapes firing output of cortical pyramidal neurons, and how the location of excitatory input influences this process. The principle findings of this study demonstrate that the impact of inhibition on neuronal output is dependent on the location of both driving excitatory input and modulatory inhibitory input.

A major difficulty in studying the contribution of synaptic location to neuronal gain control is accurately defining and isolating both excitatory and inhibitory inputs (Pouille *et al.*, 2013). Moreover, techniques which permit accurate control of input location such as dynamic patch clamp (Chance *et al.*, 2002; Shu *et al.*, 2003; Ulrich, 2003; Williams, 2004; Rothman *et al.*, 2009) do not provide physiologically realistic inputs owing to highly localised conductance changes. Studies utilising indirect stimuli, such as visual stimulation for excitatory input and optogenetic stimulation of interneuron populations (Atallah *et al.*, 2012; Lee *et al.*, 2012; Wilson *et al.*, 2012) are also problematic as they rely on assumptions regarding the relative somato-dendritic projection patterns of driving excitatory input, arising from visual stimuli, and the populations of inhibitory interneurons stimulated, as well as complexities of interneuron-interneuron network effects (Pfeffer *et al.*, 2013). In our study photo-stimulation targeted to somatic or dendritic compartments of ChR2-expressing pyramidal neurons was utilised to generate input-output relationships for somatic or

dendritic excitation (Figure 5.3). This method of generating excitation distributes input over a large area of the dendritic tree via conductance changes generated by ChR2 activation. This has the advantage of more closely mimicking excitation during synaptic input than existing methods such as dynamic clamp (Williams, 2004), where the conductance change produced is highly localised at the site of the recording pipette. During the course of our study, another research group (Pouille *et al.*, 2013) used both dendritic dynamic clamp and optogenetic excitation to investigate the impact of somatic and dendritic inhibition on input-output relationships, finding considerable differences between conductance changes produced by dynamic clamp and ChR2 activation (discussed further in Chapter Six).

Input-output relationships generated via ChR2 photo-stimulation were similar to that seen with current injection (Figure 5.3). When photo-stimulation light intensity was scaled to match rheobase and maximum firing rate the input-output relationship generated by somatic current injection had a similar slope to that generated by somatic and dendritic photo-stimulation. The relative increase in rheobase observed during dendritic compared to somatic photo-stimulation in these experiments reflects the higher level of ChR2 activation required to evoke action potential firing during depolarisation of apical dendritic regions (see Figure 4.3B,C). Together, these data demonstrate the capacity to generate excitatory input that closely mimics dendritic synaptic input by distributing conductance changes across large areas of the dendritic tree via ChR2 activation.

Selectively activating GABA receptors on either somatic or dendritic regions while driving excitatory input optogenetically allowed investigation of the modulatory effects of somatic and dendritic inhibition. During somatic excitation somatic inhibition produced an increase in rheobase, observed as a right-shift in input-output curves, while the slope of the input-output curve remained unchanged (Figure 5.4). These data are consistent with findings from CA1 neurons *in vitro* (Pouille *et al.*, 2013) and during activation of soma-targeting PV interneurons in mouse visual cortex *in vivo* (Lee *et al.*, 2012). During dendritic excitation, somatic inhibition resulted in a right-shift in the input-output curve as well as a reduction in slope (Figure 5.5). These divisive effects are consistent with other findings *in vivo* during activation of soma-targeting PV interneurons in mouse visual cortex (Atallah *et al.*, 2012; Wilson *et al.*, 2012) and somatosensory cortex (Pouille *et al.*, 2013). The findings presented here illustrate that somatic $GABA_A$-mediated inhibition generated purely subtractive effects on input-output relationships when excitatory drive is somatic, while effects are both subtractive and divisive during dendritic excitatory input.

Dendritic inhibition generated by activation of dendritic GABA receptors also led to a right shift in the input-output curve when excitation was somatic without a change in slope (Figures 5.4). In contrast, during dendritic excitation dendritic inhibition led to a right-shift in rheobase and a reduction in slope of the input-output relationship (Figure 5.5), consistent with previous work in hippocampal CA1 pyramidal neurons (Lovett-Barron *et al.*, 2012) and other experimental studies (Vu and Krasne, 1992; Lee *et al.*, 2012). Furthermore, under conditions where dendritic inhibition was generated by synaptic input, via activation of ChR2-expressing interneurons, the impact of dendritic inhibition on input-output

functions was similar to that seen during local activation of dendritic GABA receptors (Figure 5.6). Dendritic synaptic inhibition in these experiments led to a significant right-shift in input-output curves, as well as a significant reduction in slope, consistent with SOM-mediated inhibition in mouse visual cortex (Lee *et al.*, 2012). These results indicate that, similar to somatic inhibition, dendritic $GABA_A$-mediated inhibition produces both subtractive and divisive effects when excitatory drive is dendritic while effects are largely subtractive during somatic excitatory input.

In these experiments, GABA-mediated inhibition acts by increasing membrane potential hyperpolarisation and/or increasing membrane conductance. Membrane hyperpolarisation produces a subtractive effect on excitatory input while increased membrane conductance, or shunting inhibition, creates a divisive effect (Blomfield, 1974; Prescott and De Koninck, 2003; Ulrich, 2003; Silver, 2010). The present study suggests that under conditions of tonic inhibition, both somatic and dendritic inhibition can generate divisive gain control provided excitatory drive is concentrated on dendritic compartments (Figure 5.5). This observation contradicts theoretical (Trevelyan and Watkinson, 2005) and experimental studies (Vu and Krasne, 1992; Lee *et al.*, 2012; Lovett-Barron *et al.*, 2012) showing that somatic inhibition is purely subtractive and dendritic inhibition is purely divisive. Conversely, other experimental studies have demonstrated opposing findings – suggesting that somatic inhibition is purely divisive, while dendritic inhibition is purely subtractive (Atallah *et al.*, 2012; Wilson *et al.*, 2012). One possible explanation for these conflicting findings may be the presence (or absence) of synaptic noise. Indeed the influence of background synaptic noise has been shown to be crucial for

shunting inhibition to produce divisive gain control (Chance *et al.*, 2002; Mitchell and Silver, 2003; Prescott and De Koninck, 2003; Shu *et al.*, 2003). It is also important to note that in the experiments performed here, excitation of ChR2 was largely restricted to apical dendritic regions. It is uncertain whether shifting excitatory input, and corresponding inhibitory input, to more distal regions of the dendritic tree may alter the complement of subtractive and divisive effects when excitation and inhibition are co-localised. Another consideration is the level of inhibition provided by GABA application. In these experiments the pressure and frequency of GABA puffs was constant. However, it is difficult to determine how localised the GABA application is in these experiments.

There are also a number of other potential mechanisms that may influence divisive inhibitory gain control. In cerebellar granular cells, when excitation is produced by synapses with short-term depression, the non-linearity introduced under these conditions transforms subtractive effects on input-output relationships into divisive gain changes (Rothman *et al.*, 2009). Furthermore, neuromodulation of after-hyperpolarisation amplitude may alter input-output relationships so as to produce divisive gain changes (Rothman *et al.*, 2009). Another important consideration in these experiments is the temporal properties of excitatory and inhibitory inputs. Fluctuations in somatic membrane potential may elicit action potentials despite a mean membrane potential below threshold, leading to a reduction in slope (Prescott and De Koninck, 2003; Pouille *et al.*, 2013). Indeed, fluctuating conductance changes arising from temporally discrete events have been shown to alter the slope and offset of input-output functions during inhibition (Mitchell and Silver, 2003; Shu *et al.*, 2003).

Finally, an important consideration in studies modulating inhibition by activation of different interneuron populations (Atallah *et al.*, 2012; Lee *et al.*, 2012; Lovett-Barron *et al.*, 2012; Wilson *et al.*, 2012) is the interaction of these interneuron classes with each other, which may have complex effects on pyramidal cell output (Cottam *et al.*, 2013). SOM interneurons are known to inhibit PV interneurons (Pfeffer *et al.*, 2013) and can supress their firing more than twice as effectively as pyramidal cell firing in mouse visual cortex *in vivo* (Cottam *et al.*, 2013). As a result optogenetic activation of SOM cells, which target inhibition to dendritic regions of pyramidal neurons, will result in suppression of somatic inhibition. These interactions among SOM and PV cells complicate *in vivo* studies (Atallah *et al.*, 2012; Lee *et al.*, 2012; Wilson *et al.*, 2012) as SOM cell output cannot be increased independently of suppressing PV cell output. The physiological implications of the findings in this chapter are further discussed in the context of other literature in Chapter Six.

CHAPTER SIX

GENERAL DISCUSSION

Optogenetics provides a powerful new tool for studying the way neurons integrate the inputs they receive, and how this shapes information processing in the brain. In this thesis we applied this new tool to investigate the mechanisms governing information processing in the somatosensory cortex of the mouse.

The first chapter of this study characterised the expression and activation of channelrhodopsin-2 (ChR2) in somatosensory barrel cortex of a widely used ChR2-Thy-1 transgenic mouse line. Within somatosensory barrel cortex ChR2 expression was found in 96% of layer V pyramidal neurons, consistent with previous findings in this model (Arenkiel *et al.*, 2007; Wang *et al.*, 2007). However, ChR2 expression was also found in 72% of layer II/III pyramidal neurons and in the majority of fast-spiking interneurons in both layer II/III and V – 78% and 86% respectively (Figure 3.10). These findings show that ChR2 expression is not limited to layer V pyramidal neurons in this mouse model as is commonly thought.

The second chapter of this study developed a spatiotemporally precise method for optogenetic stimulation based on a projector-based optical interface. As proof-of-principle, three studies were conducted to assess the application of this method. Firstly, subcellular dendritic photo-stimulation was used to investigate the somatic impact of distal dendritic inputs in cortical pyramidal neurons. Results from this study demonstrated the capacity to produce rapid, precisely

controlled conductance changes at distal dendritic locations. Results from these experiments show that somatic amplitude of light-evoked depolarisations attenuated exponentially with increasingly distal input sites. Depolarisations generated 500 µm distal to the soma decreased by almost 6-fold. Additionally, by simultaneously photo-stimulating multiple dendritic sites at different distances distal to the soma it was possible to generate sub-linear spatial summation (Figure 4.3).

Secondly, this method of photo-stimulation was applied to mapping the spatial distribution of synaptic inputs to neurons in layer II/III and IV within somatosensory barrel cortex. Using a combination of whole-cell recordings from ChR2-negative neurons, characterised in Chapter Three, and projector-based photo-stimulation patterns, topographic 'heat' maps were constructed representing the spatial distribution of excitatory synaptic inputs onto pyramidal cells and interneurons in layer II/III and IV of primary somatosensory barrel cortex. Findings from these experiments demonstrate that layer II/III pyramidal cells receive the majority of their excitatory synaptic input from layer IV and II/III, with fewer and weaker inputs arising from layer V within the same barrel (Figure 4.6). Interneurons in layer II/III also received extensive excitatory synaptic input from layer IV in addition to surrounding layer II/III cells. The vertical profile of excitatory input to layer IV neurons indicated stronger input from layer IV and layer V than from layer II/III within the same barrel. Similar intra-columnar input profiles were also seen in interneurons residing in layer IV, where inputs were more numerous and stronger from local layer IV cells than from layer II/III or layer V (Figure 4.7).

Thirdly, using a thalamocortical slice we show that thalamocortical inputs arising from the thalamus have significantly higher connection probability and input strength in layer IV compared layer II/III and V (Figure 4.8 and 4.9).

The final Chapter of this study used experimental approaches developed in Chapter Three and Four to investigate how inhibition targeting the somatic versus dendritic compartments shapes the firing output of layer V pyramidal neurons, and how the location of excitatory input influences this process. The findings presented illustrate that when excitatory drive is close to the soma both somatic and dendritic $GABA_A$-mediated inhibition has a purely subtractive effect on input-output relationships, whereas both a subtractive and divisive effect are observed during dendritic excitatory input (Figure 5.4-5.6). Somatic inhibition produces significantly more subtractive effects when excitation is driven somatically, while generating more divisive effects during dendritic excitatory input (Figure 5.7). Together these findings suggest that both somatic and dendritic inhibition can generate divisive gain control provided excitatory drive is concentrated in distal dendritic compartments.

One constraint to using this optogenetic model is the heterogeneous expression of ChR2 in different cortical neurons (Figure 3.10). While the relatively uniform electrophysiological properties of both pyramidal and interneurons groups investigated suggest homogeneous populations of these cell types (Table 3.1), it remains possible that ChR2 expression is selective for distinct pyramidal and interneuron subtypes in this model. This raises the question of whether this heterogeneity is due to differential expression in different sub-populations of neurons or represents random expression. Variations in ChR2 expression

patterns are found across different founder lines of Thy-1-ChR2 transgenic mice (Arenkiel *et al.*, 2007; Wang *et al.*, 2007), however, the factors influencing the patterns of these variations remain poorly understood. These variations are particularly relevant for experiments investigating circuit mapping.

In Chapter Four we use ChR2 photo-stimulation to map the spatial distribution of synaptic inputs to neurons in layer II/III and IV within somatosensory barrel cortex. This method of mapping was made possible by recording from ChR2-negative neurons in layer II/III and IV (Figure 4.6 and 4.7). However, the heterogeneous expression of ChR2 in neighbouring neurons, described in Chapter Three, necessitates the caveat that synaptic input may be driven by different sub-types of neurons. Although this issue remains unresolved, previous work using ChR2 photo-stimulation for circuit mapping (Wang *et al.*, 2007) together with the results shown here demonstrate the advantages this technique has over methods such as glutamate uncaging, where large direct responses obscure local inputs. One clear advantage to the projector-based method of photo-stimulation in our study is the ability to stimulate multiple regions in parallel compared to traditional scanning techniques, which utilise serial photo-stimulation (Wang *et al.*, 2007).

ChR2 activation exhibits rapid onset kinetics generating photo-currents that are directly proportional to illumination intensity (Figure 3.9). Additionally, results presented here show that action potential firing saturates at frequencies similar to that during somatic current injection suggests that supra-threshold responses are limited by the intrinsic properties of the neuron and not the properties of the

channel itself. These findings indicate that ChR2 activation represents an effective means to investigate sub-cellular information processing.

In Chapter Five we used sub-cellular photo-stimulation together with pharmacological inhibition to investigate how inhibition targeting the somatic versus dendritic compartments shapes firing output in layer V cortical pyramidal neurons, and how the location of excitatory input influences this process. This method of generating excitation distributes input over a large area of the dendritic tree via conductance changes generated by ChR2 activation. Notably, this has the advantage of more closely mimicking excitation during synaptic input than existing methods such as dynamic clamp (Williams, 2004), where the conductance change produced is highly localised at the site of the recording pipette. Interestingly, a recent study (Pouille *et al.*, 2013) used both dendritic dynamic clamp and optogenetic excitation to investigate the impact of somatic and dendritic inhibition on input-output relationships. Findings from this study revealed significant differences between conductance changes produced by dynamic clamp and ChR2 activation, indicating a larger shunting effect during optogenetic activation. These differences may explain some of the different findings between experiments using dynamic clamp (Chance *et al.*, 2002; Rothman *et al.*, 2009) and those using optogenetic activation, such as in the present study, or *in vivo* visual stimulation (Lee *et al.*, 2012; Wilson *et al.*, 2012).

In this study we also investigated dendritic inhibition generated by network-driven inhibitory synaptic input, via activation of neighbouring ChR2-expressing interneurons (Figure 5.6). As with the circuit mapping experiments discussed above, these experiments are dependent on the populations of interneurons

expressing ChR2 in this model. Findings from Chapter Three of this study indicate that interneurons expressing ChR2 reliably generate action potentials when stimulated with higher photo-stimulation intensities (6 mW/mm^2). Electrical properties of interneurons in this model suggest a relatively homogenous population of fast-spiking interneurons (Table 3.1). However, these experiments would benefit from cell-type specific expression of ChR2 in identified classes of inhibitory interneurons (see below).

Findings from mapping synaptic excitatory input in Chapter Four suggest that fast-spiking interneurons in both layer II/III and IV (presumably parvalbumin-expressing; PV cells) receive strong input from across multiple layers (Figure 4.7). The feed-forward and feed-back inhibition arising from networks formed by these different interneuron types plays an important role in influencing information processing in pyramidal neurons. It is well known that somatostatin-expressing (SOM) and parvalbumin-expressing (PV) interneurons target their inhibition preferentially to dendritic and peri-somatic compartments respectively (Markram *et al.*, 2004; Freund and Katona, 2007; Silberberg and Markram, 2007). However, much less is known about how the ratios of SOM and PV input change under conditions of feed-forward inhibition. Indeed findings from Chapter Four on the spatial distribution of synaptic inputs to interneurons in layer II/III and IV and the suggested feed-forward inhibition these networks give rise to is likely to influence the ratio of dendritic and peri-somatic inputs to pyramidal cells. SOM interneurons are known to supress PV interneuron firing with similar (Pfeffer *et al.*, 2013) or greater (Cottam *et al.*, 2013) impact than on pyramidal cell firing. These interactions among SOM and PV cells complicate *in*

vivo studies (Atallah *et al.*, 2012; Lee *et al.*, 2012; Wilson *et al.*, 2012) as SOM cell output cannot be increased independently of suppressing PV cell output.

Another important factor in investigating somatic and dendritic inhibitory effects on input-output relationships is the impact of synaptic noise. The influence of background synaptic noise has been shown to be crucial for shunting inhibition to produce divisive gain control (Chance *et al.*, 2002; Mitchell and Silver, 2003; Prescott and De Koninck, 2003; Shu *et al.*, 2003). In this study we analysed the impact of inhibition independent of synaptic noise, it is necessary therefore for future studies to investigate the impact of different levels of synaptic noise on the effects seen during somatic and dendritic inhibition.

Additionally, to further investigate the impact of somatic versus dendritic inhibition in shaping input-output relationships in this model, photo-stimulation (and $GABA_A$-mediated inhibition) could be targeted to more distal dendritic locations to determine how this influence firing output. It may also be important to investigate the impact of inhibition on sub-threshold events. Indeed, shunting inhibition has been demonstrated to act divisively on sub-threshold voltages but in a subtractive manner on supra-threshold firing rates (Ulrich, 2003; Silver, 2010). Finally, an important factor often overlooked in studies of neuronal gain control is the temporal properties of excitatory and inhibitory inputs. Fluctuating conductance changes arising from temporally discrete events have been shown to alter the slope and offset of input-output functions during inhibition (Mitchell and Silver, 2003; Shu *et al.*, 2003). Future studies would benefit from investigating the difference between tonic inhibitory conductance and transient or noisy synaptic conductance changes.

Recent developments in optogenetics have led to successful expression of ChR2 using bacterial artificial chromosomes (BACs) with cell-type specific promoters (Zhao *et al.*, 2011; Asrican *et al.*, 2013). While not without limitations, this method overcomes the constraints associated with random transgene insertion, generated by the Thy-1 promoter by reducing positional effect variegation as a result of the larger insert size of the transgene. Together with photo-stimulation systems such as the one described in this thesis, these approaches make it possible to dissect neural circuitry with much higher specificity. Additionally, the capacity to generate simultaneous multi-wavelength photo-stimulation with our illumination system combined with an evolving toolbox of photo-sensitive proteins (Zhang *et al.*, 2007; Zhao *et al.*, 2008; Zhang *et al.*, 2011; Asrican *et al.*, 2013) permits much more sophisticated means to investigate information processing in single neurons and cortical circuits.

BIBLIOGRAPHY

Agmon, A. and Connors, B.W. (1991) Thalamocortical responses of mouse somatosensory (barrel) cortex in vitro. *Neuroscience* **41**: 365-79

Akemann, W., Lundby, A., Mutoh, H. and Knopfel, T. (2009) Effect of voltage sensitive fluorescent proteins on neuronal excitability. *Biophys J* **96**: 3959-76

Aravanis, A.M., Wang, L.P., Zhang, F., Meltzer, L.A., Mogri, M.Z., Schneider, M.B. and Deisseroth, K. (2007) An optical neural interface: in vivo control of rodent motor cortex with integrated fiberoptic and optogenetic technology. *J Neural Eng* **4**: S143-56

Arenkiel, B.R., Peca, J., Davison, I.G., Feliciano, C., Deisseroth, K., Augustine, G.J., Ehlers, M.D. and Feng, G. (2007) In vivo light-induced activation of neural circuitry in transgenic mice expressing channelrhodopsin-2. *Neuron* **54**: 205-18

Armstrong-James, M., Fox, K. and Das-Gupta, A. (1992) Flow of excitation within rat barrel cortex on striking a single vibrissa. *J Neurophysiol* **68**: 1345-58

Aronoff, R., Matyas, F., Mateo, C., Ciron, C., Schneider, B. and Petersen, C.C. (2010) Long-range connectivity of mouse primary somatosensory barrel cortex. *Eur J Neurosci* **31**: 2221-33

Asrican, B., Augustine, G.J., Berglund, K., Chen, S., Chow, N., Deisseroth, K., Feng, G., Gloss, B., Hira, R., Hoffmann, C., Kasai, H., Katarya, M., Kim, J., Kudolo, J., Lee, L.M., Lo, S.Q., Mancuso, J., Matsuzaki, M., Nakajima, R., Qiu, L., Tan, G., Tang, Y., Ting, J.T., Tsuda, S., Wen, L., Zhang, X. and Zhao, S. (2013) Next-generation transgenic mice for optogenetic analysis of neural circuits. *Front Neural Circuits* **7**: 160

Atallah, B.V., Bruns, W., Carandini, M. and Scanziani, M. (2012) Parvalbumin-expressing interneurons linearly transform cortical responses to visual stimuli. *Neuron* **73**: 159-70

Avermann, M., Tomm, C., Mateo, C., Gerstner, W. and Petersen, C.C. (2012) Microcircuits of excitatory and inhibitory neurons in layer 2/3 of mouse barrel cortex. *J Neurophysiol* **107**: 3116-34

Blomfield, S. (1974) Arithmetical operations performed by nerve cells. *Brain Res* **69**: 115-24

Bock, O. (2013) Cajal, Golgi, Nansen, Schafer and the neuron doctrine. *Endeavour* **37**: 228-34

Boyden, E.S., Zhang, F., Bamberg, E., Nagel, G. and Deisseroth, K. (2005) Millisecond-timescale, genetically targeted optical control of neural activity. *Nat Neurosci* **8**: 1263-8

Branco, T. and Hausser, M. (2010) The single dendritic branch as a fundamental functional unit in the nervous system. *Curr Opin Neurobiol* **20**: 494-502

Brazier, M.A.B. (1988) A history of neurophysiology in the 19th century, xiv, 265 p. pp. Raven Press, New York.

Bureau, I., von Saint Paul, F. and Svoboda, K. (2006) Interdigitated paralemniscal and lemniscal pathways in the mouse barrel cortex. *PLoS Biol* **4**: e382

Chance, F.S., Abbott, L.F. and Reyes, A.D. (2002) Gain modulation from background synaptic input. *Neuron* **35**: 773-82

Chen, Q., Cichon, J., Wang, W., Qiu, L., Lee, S.J., Campbell, N.R., Destefino, N., Goard, M.J., Fu, Z., Yasuda, R., Looger, L.L., Arenkiel, B.R., Gan, W.B. and Feng, G. (2012) Imaging neural activity using Thy1-GCaMP transgenic mice. *Neuron* **76**: 297-308

Connors, B.W. and Gutnick, M.J. (1990) Intrinsic firing patterns of diverse neocortical neurons. *Trends Neurosci* **13**: 99-104

Cottam, J.C., Smith, S.L. and Hausser, M. (2013) Target-specific effects of somatostatin-expressing interneurons on neocortical visual processing. *J Neurosci* **33**: 19567-78

Davie, J.T., Kole, M.H., Letzkus, J.J., Rancz, E.A., Spruston, N., Stuart, G.J. and Hausser, M. (2006) Dendritic patch-clamp recording. *Nat Protoc* **1**: 1235-47

DeFelipe, J., Lopez-Cruz, P.L., Benavides-Piccione, R., Bielza, C., Larranaga, P., Anderson, S., Burkhalter, A., Cauli, B., Fairen, A., Feldmeyer, D., Fishell, G., Fitzpatrick, D., Freund, T.F., Gonzalez-Burgos, G., Hestrin, S., Hill, S., Hof, P.R., Huang, J., Jones, E.G., Kawaguchi, Y., Kisvarday, Z., Kubota, Y., Lewis, D.A., Marin, O., Markram, H., McBain, C.J., Meyer, H.S., Monyer, H., Nelson, S.B., Rockland, K., Rossier, J., Rubenstein, J.L., Rudy, B., Scanziani, M., Shepherd, G.M., Sherwood, C.C., Staiger, J.F., Tamas, G., Thomson, A., Wang, Y., Yuste, R. and Ascoli, G.A. (2013) New insights into the classification and nomenclature of cortical GABAergic interneurons. *Nat Rev Neurosci* **14**: 202-16

Douglas, R.J. and Martin, K.A. (2004) Neuronal circuits of the neocortex. *Annu Rev Neurosci* **27**: 419-51

Feng, G., Mellor, R.H., Bernstein, M., Keller-Peck, C., Nguyen, Q.T., Wallace, M., Nerbonne, J.M., Lichtman, J.W. and Sanes, J.R. (2000) Imaging neuronal subsets in transgenic mice expressing multiple spectral variants of GFP. *Neuron* **28**: 41-51

Franklin, K.B.J. and Paxinos, G. (2008) The mouse brain in stereotaxic coordinates. 3rd ed. 1 vols. Elsevier/Academic Press, Amsterdam ; Boston.

Freund, T.F. and Katona, I. (2007) Perisomatic inhibition. *Neuron* **56**: 33-42

Gilbert, C.D. and Wiesel, T.N. (1983) Clustered intrinsic connections in cat visual cortex. *J Neurosci* **3**: 1116-33

Gordon, J.W., Chesa, P.G., Nishimura, H., Rettig, W.J., Maccari, J.E., Endo, T., Seravalli, E., Seki, T. and Silver, J. (1987) Regulation of Thy-1 gene expression in transgenic mice. *Cell* **50**: 445-52

Grinvald, A. and Hildesheim, R. (2004) VSDI: a new era in functional imaging of cortical dynamics. *Nat Rev Neurosci* **5**: 874-85

Hamill, O.P., Marty, A., Neher, E., Sakmann, B. and Sigworth, F.J. (1981) Improved patch-clamp techniques for high-resolution current recording from cells and cell-free membrane patches. *Pflugers Arch* **391**: 85-100

Helmchen, F., Svoboda, K., Denk, W. and Tank, D.W. (1999) In vivo dendritic calcium dynamics in deep-layer cortical pyramidal neurons. *Nat Neurosci* **2**: 989-96

Holt, G.R. and Koch, C. (1997) Shunting inhibition does not have a divisive effect on firing rates. *Neural Comput* **9**: 1001-13

Ji, N., Shroff, H., Zhong, H. and Betzig, E. (2008) Advances in the speed and resolution of light microscopy. *Curr Opin Neurobiol* **18**: 605-16

Kogan, A., Ross, W.N., Zecevic, D. and Lasser-Ross, N. (1995) Optical recording from cerebellar Purkinje cells using intracellularly injected voltage-sensitive dyes. *Brain Res* **700**: 235-9

Larkum, M.E., Nevian, T., Sandler, M., Polsky, A. and Schiller, J. (2009) Synaptic integration in tuft dendrites of layer 5 pyramidal neurons: a new unifying principle. *Science* **325**: 756-60

Lasser-Ross, N., Miyakawa, H., Lev-Ram, V., Young, S.R. and Ross, W.N. (1991) High time resolution fluorescence imaging with a CCD camera. *J Neurosci Methods* **36**: 253-61

Lee, A.K., Manns, I.D., Sakmann, B. and Brecht, M. (2006) Whole-cell recordings in freely moving rats. *Neuron* **51**: 399-407

Lee, S.H., Kwan, A.C. and Dan, Y. (2014) Interneuron subtypes and orientation tuning. *Nature* **508**: E1-2

Lee, S.H., Kwan, A.C., Zhang, S., Phoumthipphavong, V., Flannery, J.G., Masmanidis, S.C., Taniguchi, H., Huang, Z.J., Zhang, F., Boyden, E.S., Deisseroth, K. and Dan, Y. (2012) Activation of specific interneurons

improves V1 feature selectivity and visual perception. *Nature* **488**: 379-83

Lefort, S., Tomm, C., Floyd Sarria, J.C. and Petersen, C.C. (2009) The excitatory neuronal network of the C2 barrel column in mouse primary somatosensory cortex. *Neuron* **61**: 301-16

Losonczy, A. and Magee, J.C. (2006) Integrative properties of radial oblique dendrites in hippocampal CA1 pyramidal neurons. *Neuron* **50**: 291-307

Lovett-Barron, M., Turi, G.F., Kaifosh, P., Lee, P.H., Bolze, F., Sun, X.H., Nicoud, J.F., Zemelman, B.V., Sternson, S.M. and Losonczy, A. (2012) Regulation of neuronal input transformations by tunable dendritic inhibition. *Nat Neurosci* **15**: 423-30, S1-3

Magee, J.C. (2000) Dendritic integration of excitatory synaptic input. *Nat Rev Neurosci* **1**: 181-90

Markram, H., Toledo-Rodriguez, M., Wang, Y., Gupta, A., Silberberg, G. and Wu, C. (2004) Interneurons of the neocortical inhibitory system. *Nat Rev Neurosci* **5**: 793-807

Matsuzaki, M., Honkura, N., Ellis-Davies, G.C. and Kasai, H. (2004) Structural basis of long-term potentiation in single dendritic spines. *Nature* **429**: 761-6

Megias, M., Emri, Z., Freund, T.F. and Gulyas, A.I. (2001) Total number and distribution of inhibitory and excitatory synapses on hippocampal CA1 pyramidal cells. *Neuroscience* **102**: 527-40

Mitchell, S.J. and Silver, R.A. (2003) Shunting inhibition modulates neuronal gain during synaptic excitation. *Neuron* **38**: 433-45

Mountcastle, V.B. (1997) The columnar organization of the neocortex. *Brain* **120 (Pt 4)**: 701-22

Murayama, M., Perez-Garci, E., Nevian, T., Bock, T., Senn, W. and Larkum, M.E. (2009) Dendritic encoding of sensory stimuli controlled by deep cortical interneurons. *Nature* **457**: 1137-41

Nagel, G., Szellas, T., Huhn, W., Kateriya, S., Adeishvili, N., Berthold, P., Ollig, D., Hegemann, P. and Bamberg, E. (2003) Channelrhodopsin-2, a directly light-gated cation-selective membrane channel. *Proc Natl Acad Sci U S A* **100**: 13940-5

Nagel, G., Szellas, T., Kateriya, S., Adeishvili, N., Hegemann, P. and Bamberg, E. (2005) Channelrhodopsins: directly light-gated cation channels. *Biochem Soc Trans* **33**: 863-6

Palmer, L.M. and Stuart, G.J. (2009) Membrane potential changes in dendritic spines during action potentials and synaptic input. *J Neurosci* **29**: 6897-903

Panzeri, S., Petroni, F., Petersen, R.S. and Diamond, M.E. (2003) Decoding neuronal population activity in rat somatosensory cortex: role of columnar organization. *Cereb Cortex* **13**: 45-52

Petersen, C.C. and Sakmann, B. (2001) Functionally independent columns of rat somatosensory barrel cortex revealed with voltage-sensitive dye imaging. *J Neurosci* **21**: 8435-46

Pfeffer, C.K., Xue, M., He, M., Huang, Z.J. and Scanziani, M. (2013) Inhibition of inhibition in visual cortex: the logic of connections between molecularly distinct interneurons. *Nat Neurosci* **16**: 1068-76

Pouille, F., Watkinson, O., Scanziani, M. and Trevelyan, A.J. (2013) The contribution of synaptic location to inhibitory gain control in pyramidal cells. *Physiol Rep* **1**: e00067

Prescott, S.A. and De Koninck, Y. (2003) Gain control of firing rate by shunting inhibition: roles of synaptic noise and dendritic saturation. *Proc Natl Acad Sci U S A* **100**: 2076-81

Ross, W.N. and Werman, R. (1987) Mapping calcium transients in the dendrites of Purkinje cells from the guinea-pig cerebellum in vitro. *J Physiol* **389**: 319-36

Rothman, J.S., Cathala, L., Steuber, V. and Silver, R.A. (2009) Synaptic depression enables neuronal gain control. *Nature* **457**: 1015-8

Rothman, S.M. and Olney, J.W. (1986) Glutamate and the pathophysiology of hypoxic--ischemic brain damage. *Ann Neurol* **19**: 105-11

Rudy, B., Fishell, G., Lee, S. and Hjerling-Leffler, J. (2011) Three groups of interneurons account for nearly 100% of neocortical GABAergic neurons. *Dev Neurobiol* **71**: 45-61

Sakai, S., Ueno, K., Ishizuka, T. and Yawo, H. (2013) Parallel and patterned optogenetic manipulation of neurons in the brain slice using a DMD-based projector. *Neurosci Res* **75**: 59-64

Shepherd, G.M., Pologruto, T.A. and Svoboda, K. (2003) Circuit analysis of experience-dependent plasticity in the developing rat barrel cortex. *Neuron* **38**: 277-89

Shu, Y., Hasenstaub, A., Badoual, M., Bal, T. and McCormick, D.A. (2003) Barrages of synaptic activity control the gain and sensitivity of cortical neurons. *J Neurosci* **23**: 10388-401

Silberberg, G. and Markram, H. (2007) Disynaptic inhibition between neocortical pyramidal cells mediated by Martinotti cells. *Neuron* **53**: 735-46

Silver, R.A. (2010) Neuronal arithmetic. *Nat Rev Neurosci* **11**: 474-89

Spruston, N. (2008) Pyramidal neurons: dendritic structure and synaptic integration. *Nat Rev Neurosci* **9**: 206-21

Staiger, J.F., Flagmeyer, I., Schubert, D., Zilles, K., Kotter, R. and Luhmann, H.J. (2004) Functional diversity of layer IV spiny neurons in rat somatosensory cortex: quantitative morphology of electrophysiologically characterized and biocytin labeled cells. *Cereb Cortex* **14**: 690-701

Stirman, J.N., Crane, M.M., Husson, S.J., Wabnig, S., Schultheis, C., Gottschalk, A. and Lu, H. (2011) Real-time multimodal optical control of neurons and muscles in freely behaving Caenorhabditis elegans. *Nat Methods* **8**: 153-8

Stuart, G.J. and Sakmann, B. (1994) Active propagation of somatic action potentials into neocortical pyramidal cell dendrites. *Nature* **367**: 69-72

Trevelyan, A.J. and Watkinson, O. (2005) Does inhibition balance excitation in neocortex? *Prog Biophys Mol Biol* **87**: 109-43

Ulrich, D. (2003) Differential arithmetic of shunting inhibition for voltage and spike rate in neocortical pyramidal cells. *Eur J Neurosci* **18**: 2159-65

Vidal, M., Morris, R., Grosveld, F. and Spanopoulou, E. (1990) Tissue-specific control elements of the Thy-1 gene. *EMBO J* **9**: 833-40

Vu, E.T. and Krasne, F.B. (1992) Evidence for a computational distinction between proximal and distal neuronal inhibition. *Science* **255**: 1710-2

Wallace, D.J., Meyer zum Alten Borgloh, S., Astori, S., Yang, Y., Bausen, M., Kugler, S., Palmer, A.E., Tsien, R.Y., Sprengel, R., Kerr, J.N., Denk, W. and Hasan, M.T. (2008) Single-spike detection in vitro and in vivo with a genetic Ca2+ sensor. *Nat Methods* **5**: 797-804

Wang, H., Peca, J., Matsuzaki, M., Matsuzaki, K., Noguchi, J., Qiu, L., Wang, D., Zhang, F., Boyden, E., Deisseroth, K., Kasai, H., Hall, W.C., Feng, G. and Augustine, G.J. (2007) High-speed mapping of synaptic connectivity using photostimulation in Channelrhodopsin-2 transgenic mice. *Proceedings of the National Academy of Sciences of the United States of America* **104**: 8143-8

Williams, S.R. (2004) Spatial compartmentalization and functional impact of conductance in pyramidal neurons. *Nat Neurosci* **7**: 961-7

Williams, S.R. and Stuart, G.J. (2003) Role of dendritic synapse location in the control of action potential output. *Trends Neurosci* **26**: 147-54

Wilson, N.R., Runyan, C.A., Wang, F.L. and Sur, M. (2012) Division and subtraction by distinct cortical inhibitory networks in vivo. *Nature* **488**: 343-8

Yuste, R. and Tank, D.W. (1996) Dendritic integration in mammalian neurons, a century after Cajal. *Neuron* **16**: 701-16

Zhang, F., Vierock, J., Yizhar, O., Fenno, L.E., Tsunoda, S., Kianianmomeni, A., Prigge, M., Berndt, A., Cushman, J., Polle, J., Magnuson, J., Hegemann, P. and Deisseroth, K. (2011) The microbial opsin family of optogenetic tools. *Cell* **147**: 1446-57

Zhang, F., Wang, L.P., Boyden, E.S. and Deisseroth, K. (2006) Channelrhodopsin-2 and optical control of excitable cells. *Nat Methods* **3**: 785-92

Zhang, F., Wang, L.P., Brauner, M., Liewald, J.F., Kay, K., Watzke, N., Wood, P.G., Bamberg, E., Nagel, G., Gottschalk, A. and Deisseroth, K. (2007) Multimodal fast optical interrogation of neural circuitry. *Nature* **446**: 633-9

Zhang, J., Laiwalla, F., Kim, J.A., Urabe, H., Van Wagenen, R., Song, Y.K., Connors, B.W., Zhang, F., Deisseroth, K. and Nurmikko, A.V. (2009) Integrated device for optical stimulation and spatiotemporal electrical recording of neural activity in light-sensitized brain tissue. *J Neural Eng* **6**: 055007

Zhang, Y.P. and Oertner, T.G. (2007) Optical induction of synaptic plasticity using a light-sensitive channel. *Nat Methods* **4**: 139-41

Zhao, S., Cunha, C., Zhang, F., Liu, Q., Gloss, B., Deisseroth, K., Augustine, G.J. and Feng, G. (2008) Improved expression of halorhodopsin for light-induced silencing of neuronal activity. *Brain Cell Biol* **36**: 141-54

Zhao, S., Ting, J.T., Atallah, H.E., Qiu, L., Tan, J., Gloss, B., Augustine, G.J., Deisseroth, K., Luo, M., Graybiel, A.M. and Feng, G. (2011) Cell type-specific channelrhodopsin-2 transgenic mice for optogenetic dissection of neural circuitry function. *Nat Methods* **8**: 745-52